Mixing of salinity by ship traffic in canals

Noor ten Harmsen
van der Beek

TU Delft

Deltares

Mixing of salinity by ship traffic in canals

by

Noor ten Harmsen van der Beek

In partial fulfilment of the requirements for the degree of

Master of Science
in Hydraulic Engineering
at the Delft University of Technology,

to be defended publicly on Thursday April 22, 2021 at 13:30 AM.

Thesis committee:	Dr. ir. R.J. Labeur,	TU Delft
	Prof. dr. ir. J.D. Pietrzak,	TU Delft
	Ir. O.M. Weiler,	Deltares
	Ir. A.C. Bijlsma,	Deltares
	Ir. A.J. van der Hout,	Deltares, TU Delft

An electronic version of this thesis is available at `http://repository.tudelft.nl/`.

Front cover made by Aditya Parulekar.

TU Delft

Deltares

Preface

This study marks the end of my study Hydraulic Engineering at the TU Delft, a period I thoroughly enjoyed. I enjoyed exploring this topic, and I hope I am able to transfer this to the reader, who might be inspired to continue the work on this topic.

I would like to thank my graduation committee for their support during the thesis work. Robert Jan Labeur, I would like to thank you for all the support throughout the thesis, from helping me set up the model to helping me structure the report. It would have been much more difficult to study this topic without the ability to add a moving ship in the model as was possible thanks to your code. Otto Weiler, thank you for suggesting this thesis topic, it was indeed very interesting! Thank you for the enthusiasm for my work during our meetings and for the short insights about maritime engineering. Arnout Bijlsma, you always had many valuable ideas and suggestions for further analysis, while also providing a critical eye to my both my results as the report, thank you for that. Julie Pietrzak, thank you for the words of encouragement and pushing me to focus my research. Furthermore, thank you for introducing me to the fascinating field of stratified flow in the first place, I really enjoyed your lecture series. Arne van der Hout, as you joined the committee later on in the process, you were able to give a fresh perspective on the work and were valuable in making sure the thesis is easily understandable. I would also like to thank Otti Kievits for helping me plan my meetings. It was always a pleasure to call you, especially in these strange times.

Furthermore, I would like to thank Deltares for facilitating my thesis and giving me a look inside this interesting research institute. I would also like to thank the people at Rijkswaterstaat and all the other people I spoke with over the course of this project. It was very valuable for me to hear about your experiences with salt intrusion in canals and to discuss possible ways ships contribute to mixing.

Another round of thanks goes to my family and friends, who have supported me throughout this project. My parents, Sander, Lotte for always being available to help or call, and also Bowie of course. Tess, I enjoyed our discussions on stratified flow and mixing a lot. Vesna, thank you for proof-reading and giving feedback. Margot, thank you for being my 'co-worker' this year, and, Anna-Lisa, thank you for filling in for Margot from time to time. Sheela, for cooking many meals for me in busy periods. I also would like to apologise to my rowing team for being somewhat distracted by passing barges on the Schie. Finally, I would like to thank Aditya, who has provided me with a gigantic amount of support and help. Thank you for being there for the highs and lows of this thesis.

N.J.M. (Noor) ten Harmsen van der Beek
Delft, April 2021

Contents

List of Symbols

Symbol	Unit	Description
APE	J/m^3	available potential energy
a	m	amplitude
C	$m^{\frac{1}{2}}/s$	Chézy coefficient
c_0	m/s	long wave speed
C_3	-	propeller coefficient
d	m	draught
D_p	m	propeller diameter
E_c	J	energy dissipation by a current
E_s	J	energy dissipation by ship traffic
E_w	J	energy dissipation by wind
f_p	%	percentage of propeller power used
Fr	–	Froude number
Fr_c	–	critical Froude number
$Fr_{c,L}$	–	critical Froude number taking into account the vessel length
g	m/s^2	gravitational acceleration
h	m	depth of the bed
$h_{1,2}$	m	height of layer 1 or 2
H	m	total water depth
KE	J/m^3	kinetic energy
k_h	–	horizontal wave number
L	m	length of canal or vessel
L_w	m	wave length
m	–	vertical wave number
$m_{1,2}$	–	canal blockage of layer 1 or 2
N	s^{-1}	buoyancy frequency
n	–	number of ships or wave mode
P	W	engine power
p	Pa	pressure
PEA	J/m^3	potential energy anomaly
P_d	W	maximum installed propeller power
r	–	slope internal wave characteristic distance from axis perpendicular to outflow of propeller jet

Symbol	Unit	Description
Ri_B	-	bulk Richardson number
Ri_g	-	gradient Richardson number
Ri_u	-	layer Richardson number
$R0$	-	relative density difference
$S_{1,2}$	$-$	surface of vessel in top or bottom layer
s	$-$	topographic slope
t	s	time
T	s	wave period
u	m/s	velocity
u_{grid}	m/s	velocity of the grid
U	m/s	vessel sailing speed
$\bar{u}$	m/s	depth-averaged velocity
V_{axis}	m/s	propeller jet velocity along the outflow axis
V_0	m/s	efflux velocity propeller
$V_{x,r}$	m/s	propeller jet velocity at distance from the outflow point
w_c	m	width of the canal
w_s	m	width of the ship
x	m	horizontal distance
z	m	vertical coordinate
γ	-	density ratio, $\gamma = \frac{\rho_1}{\rho_2}$
ϵ	$-$	relative density difference, $\frac{\rho_2 - \rho_1}{\rho_1}$
δ	m	thickness of mixing layer
η	m	free surface
κ	m^2/s	turbulence diffusivity
μ	m^2/s	kinematic viscosity
ξ	$-$	Iribarren number
ρ	kg/m^3	density
ρ_0	kg/m^3	reference density
ρ_w	kg/m^3	water density
$\bar{\rho}$	kg/m^3	depth-averaged density
τ	Pa	bottom shear stress
ϕ	rad	angle of V-shape of the waves

Summary

Salt intrusion poses a threat to the fresh water supply function of inland waterways. This threat will increase due to climate change, the construction of large sea locks, and deepening of channels. How far inland salt intrusion reaches is dependent on a balance of buoyancy forcing, water depth, discharge of the canal and the amount of mixing. Wind, bottom roughness, and sailing ships contribute to mixing. Currently little is known about the contribution of the latter to mixing. It is important to better understand the role of ship traffic in order to make more accurate models and take the right measures to protect the fresh water supply function of inland waterways. The aim of this study is to get insight in the amount of mixing ships generate and which processes are responsible for this. The final goal is to include mixing by ship traffic in large-scale numerical models.

The flow field in an unstratified canal has been well studied, however, little is known about the effects ships have in a stratified canal. Ships move water when sailing through a waterway. This induces three water movements: primary and secondary waves and the propeller jet flow. The locally large velocities of the return current related to the primary wave could contribute to mixing by shear instabilities. A ship sailing in a stratified canal generates secondary waves on the water surface as well as internal waves. This V-shaped wave pattern could contribute to mixing by shear instabilities in the wave field or wave breaking on the canal banks. The high velocities in the propeller jet could entrain surrounding fluid and contribute to mixing. Rough estimations based on the propeller power or data from a blockage of the waterway indicate that ship traffic is an important factor in the amount of stratification in a canal.

Numerical calculations are applied to study these processes in more detail and find the amount of mixing. A sailing ship in a stratified canal has been modelled using a moving grid approach in the 3D non-hydrostatic finite element model FinLab. The propeller has been neglected to simplify the model. A parameter study has been performed to observe the influence of several parameters (such as the canal blockage, internal Froude number, and canal bank slope) on the flow pattern and the amount of mixing. The results show that the interface between two layers of different density moves down around the vessel and comes up again behind the vessel. Internal waves follow the vessel in a V-shape, comparable to a supercritical surface wave pattern. The increased velocities around the vessel cause shear at the ship hull and the bed. Internal wave instabilities and interaction with the slope cause additional mixing.

The amount of mixing is found to be in the order of magnitude of 1 percent for one vessel over 600 m canal length a representative range of parameters of canal geometry, density profile, vessel draught and vessel speed. The actual effect will be larger since the internal wave field is still present at the outflow boundary and since the propeller has been omitted from the model set-up. Processes around the vessel and the internal waves contribute about equally to the amount of mixing in the model domain. The internal waves are estimated to have contribution of about twice as large if the modelled domain was longer. As the interface comes up behind the vessel, it is likely that the propeller jet can have a large impact on the density field directly behind the vessel.

The vessel speed, density profile, relative density difference, layer distribution in a two-layer flow, canal blockage, draught to top layer height ratio, and the slope of canal banks are important parameters in the amount of mixing generated. The canal blockage, vessel speed, and layer distribution a two-layer flow influence both the mixing from the return current as the internal waves. The draught to top layer height is found to be a good parameter to estimate the height of the interface deformations. The density profile and relative density difference mainly influence the mixing from the internal wave field behind the vessel. A sloped canal bank reduces the wave reflection and results in wave breaking at the banks. Of these parameters, the canal blockage and layer distribution in a two-layer flow showed the largest impact on the amount of mixing for representative values in a typical canal.

Due to the cumulative effect of the ship traffic, mixing by ship traffic is estimated to be of large importance on the density distribution in a canal. More research is needed to include this effect in large-scale numerical models and find a good parameterisation. How mixing by ship traffic could finally be implemented will be dependent on the numerical model that is used, and the amount of detail that is needed.

1 Introduction

1.1. Context: Salt intrusion and mixing processes

Inland waterways have many different functions. They are used by shipping traffic to transport goods and people. They discharge water to the sea, and supply water in times of drought. The supplied water is used for drinking water, cooling and process water. At the same time, inland waterways are also important for the ecological system of an area. (Savenije (2012)).

Salt water from the sea intrudes the fresh water in inland waterways via density currents. Closed systems have locks that allow shipping traffic to pass. These locks form a division between fresh and salt water. Without taking special measures, salt water intrudes into the fresh water. Internal pressure gradients drive a flow, which results in fresh water outflow at the top and salt water inflow at the bottom when a lock opens. The resulting density differences cause density-driven currents in the inland waterways. Examples of canals in the Netherlands with salt intrusion through a lock are the Noordzeekanaal, which is connected to the sea via the locks at IJmuiden, and the Antwerps Kanaalpand, which is connected to the Port of Antwerp and the Schelde.

The incoming salt is a threat to the fresh water supply function of a canal. Fresh water is important for drinking water, agriculture, industry, and nature. This makes it important to know how far the salt intrusion reaches to be able to take measures to prevent salt water reaching too far inland. Understanding the phenomena that play a role in salt intrusion becomes even more important when looking at recent and predicted developments. Climate change (resulting in longer dry periods, less water discharge from the rivers, and sea-level rise) and channel deepening will enlarge the salt intrusion problems (Haasnoot et al. (2018), Savenije (2012)).

How far the salt intrusion in a canal reaches is dependent on the balance of buoyancy forcing, discharge of the canal and turbulent mixing. A typical inland waterway forms a weakly dynamical system with low flow velocities and little mixing. There is not one dominant force that causes mixing. The length and shape of the salt intrusion is dependent on the amount of mixing and buoyancy forcing from the fresh and salt boundaries of the canal. The density profile can be vertically mixed or can have increasing density over depth, and sometimes a clear salt wedge can be observed. The Noordzeekanaal for example has a clear salt wedge, while the Antwerps Kanaalpand is mostly vertically mixed.

Stratification results in a damping of the amount of mixing and can also allow for internal waves (Sarkar, 2005). The buoyancy forcing is mainly dependent on the density gradient. More vertical mixing causes the density profile to become less steep. Discharge, wind, and sailing ships cause vertical mixing (Karelse and Van Gils, 1991). Wind and bottom roughness cause respectively a shear stress on the top or bottom of a water column, which results in turbulent boundary layer and mixing (Sarkar, 2005). A larger water discharge results in higher shear and thus more mixing. The channel depth is also of influence on how far the salt intrusion reaches. Ships move large amounts of water when moving through the water. This could lead to mixing due to shear stresses or internal waves. Below, Figure 1.1 summarises the above mentioned factors influencing mixing in a canal.

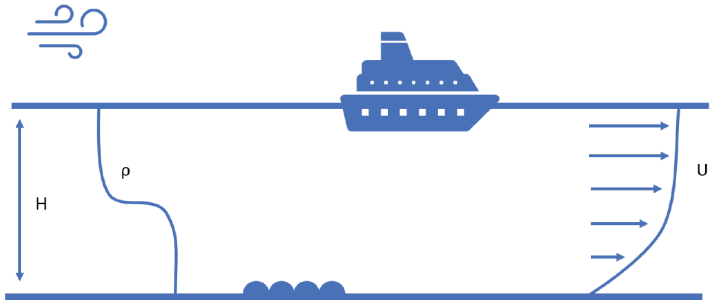

Figure 1.1: The density distribution is influenced by the density profile (ρ), the water depth (H), wind, bottom roughness, flow velocity in the canal (U) and sailing ships.

1.2. Problem statement: Unknown contribution of ship traffic

It is important to understand all factors in play from a system- and a physical understanding. The system understanding is important, because understanding the system means that the right measures can be applied to influence salinity levels. Understanding the physical processes is needed in order to make accurate numerical models of water quality and salinity. By understanding the process better, the fresh water supply functions of inland waters can be better warranted.

Currently, there is gap in knowledge of the role of ships in vertical mixing of salinity. Early research has been done with for example field observations and laboratory tests (Stefan and Riley, 1985) and field experiments (Moser and Bakker, 1989). Karelse and Van Gils (1991) estimated the impact of ship traffic on mixing in the Noordzeekanaal to be a few order of magnitudes higher than wind or bottom shear, however, there are a lot of uncertainties, such as for example how efficient a ship's energy is converted into kinetic energy for vertical mixing. Maderich et al. (2008) included the effect of ship traffic in a numerical model by adding a term to the vertical eddy and diffusion terms based on the assumptions that the influence of the vessel can be seen as an influx of turbulent energy in the top layer and that the mixing of water is related to the propeller jet. It is however unknown whether these assumptions are correct. During a blockage of the Schelde-Rijnkanaal, the amount of stratification increased which could be attributed to the lack of mixing by ship traffic (see later in this study). Additionally, a later data analysis from Hydrologic (2020) concludes that weekly variation in ship traffic is the most likely cause of the weekly variation in chloride levels in the Amsterdam Rijnkanaal. How much this is due to mixing by ship traffic or the amount of lock operations is unclear from this study.

These previously mentioned studies show that there is a contribution of ships to mixing in a canal, however, these studies have not studied which processes cause ship-induced vertical mixing and have not found a generic formulation to describe the mixing. Factors that have been found to play a role are the dimensions of the ship and waterway, sailing speed and passing frequency, level of the interface of fresh and salt water, and the density difference (Moser and Bakker (1989) and Stefan and Riley (1985)). Other factors than the above mentioned could possibly also play a role in vertical mixing by sailing ships.

The effect of ship traffic on the transport of salinity is also still largely unknown. A ship fills a certain volume in the waterway. When it moves, the water is pushed away in front and replaced in the back. In this way, ships are a source of transport of salinity, even when not taking into account mixing processes. In reality, mixing and transport occur simultaneously.

In many other cases, ship traffic is acknowledged as a factor but neglected (for example Verbruggen and Buschman (2020)). This lack in system understanding makes it harder to make accurate models and predictions of salinity levels in a waterway. Currently, there are only estimations that suggest that vessels have a role in mixing and transport of salinity, and no good quantification of the mixing caused by a ship is available. A better understanding of the physical processes that cause ship-generated mixing in a stratified canal is needed before a generic formulation or parametrisation for a large-scale model can be found. Figure 1.2 summarises the possible contributing processes to ship-induced mixing. This study will focus on finding the contribution of these processes to vertical mixing.

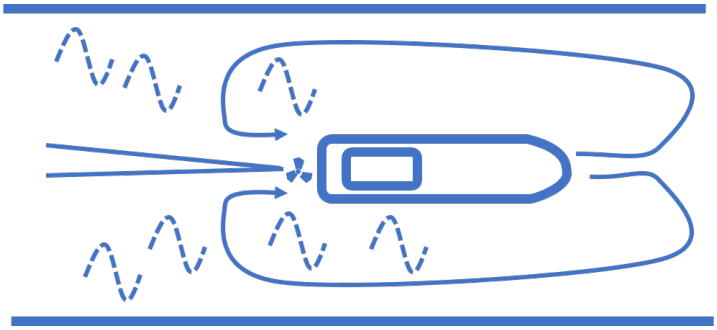

Figure 1.2: Ship-induced mixing processes could be the return flow around the vessel, internal waves and the propeller jet.

1.3. Objective and research questions

The research proposed in this project proposal aims to reach a better understanding of the effect of ship traffic on mixing and transport of salinity in order to include this effect, when relevant, in numerical models and to be able to model salinity levels better. The objective is to give an advice on how to implement this. First, an estimation of the order of magnitude of the effect is needed. The processes that play role need to be identified before their role can be investigated. This research focuses on processes in an inland waterway with fresh and salt water, not taking into account the processes near a lock, and will be limited to shipping traffic in canals.

This translates in the following main research question:

To what extent is ship traffic responsible for the vertical mixing in a stratified canal, and to which processes can this be attributed?

The following sub-questions are used to answer this main question and to further study this problem.

- What are the governing parameters in these processes, and how do these parameters influence vertical mixing and transport?
- How significant is the effect of shipping traffic on mixing and transport of salinity in relation to other mixing and transport terms?
- Which steps need to be taken to include the mixing and transport of salinity caused by ship traffic in weakly-dynamical inland waterways in 2DV- and 3D numerical models?

1.4. Research approach

First, an overview of current knowledge of mixing processes in density-driven flow, and the interaction between ships and water, both in a stratified and in a non-stratified case is given to identify key processes and parameters. This can be read in Chapter 2. In Chapter 3, the Noordzeekanaal and Antwerps Kanaalpand are introduced as typical canals with salt intrusion in the Netherlands. Also, the theoretical effect of the most relevant parameters is studied. This can only give limited insight in the effect of ship traffic on the salinity distribution in the canals. The effect of the identified parameters is therefore tested with numerical experiments in an advanced numerical non-hydrostatic 3D-model. Chapter 4 describes the set up of this numerical model and Chapter 5 describes the model results. The results of this study are discussed in Chapter 6 and the conclusions to the above research questions are given in Chapter 7.

2

Literature study

In this chapter, the aim is to give an overview of current knowledge on ship-induced mixing in a stratified flow. First, mixing mechanisms in stratified flow are discussed. This is followed by a description of the flow field around a vessel for an unstratified and stratified canal. The flow field in an unstratified canal has been well researched, however, less is known about ships in a stratified canal. Density differences in a canal might cause specific density-driven effects such as internal waves, shear between layers of different density, or density-driven flow.

A special focus will be on the three possible mixing processes mentioned already in the introduction:

- Return current
- Internal waves
- Propeller jet

2.1. Mixing mechanisms in stratified flow

Stratification can be the result of salinity, temperature, or chemical composition. In this study, only density differences caused by a salinity difference are discussed. The stratification can take different forms. This state is the result of the buoyancy forcing and the inertial forcing. In weakly-dynamical canals as studied here, mixing is not dominated by one mixing factor, but rather driven by a combination of different factors, such as wind forcing, discharge, lock operations, and ship traffic. This section does not look at these forcing-mechanisms, but rather at the mixing processes that are possibly relevant for mixing by ship traffic.

2.1.1. Quantifying stratification and mixing efficiency

The stratification in a canal is the result of the buoyancy forcing versus the amount of mixing. In this section, quantities that describe the amount of stratification are described. The mixing efficiency is discussed as well.

The buoyancy frequency and the potential energy anomaly are two parameters to describe the state of the flow with respect to stratification. The buoyancy frequency or Brunt-Väisälä frequency (N in s^{-1}) describes the oscillation frequency of a displaced neutrally buoyant particle in a stratified flow (Pietrzak, 2012).

$$N^2 = -\frac{g}{\rho_0}\frac{\partial \rho}{\partial z} \tag{2.1}$$

with reference density ρ_0 and the gradient of the density over depth $\frac{\partial \rho}{\partial z}$. The buoyancy frequency is constant for a linear density profile. Another parameter to describe the flow state is the potential energy anomaly (PEA in J/m^3). The PEA gives the potential energy relative to the mixed state, so the energy required to achieve a well-mixed state per volume (Simpson et al., 1990).

$$PEA = \frac{1}{H}\int_{-h}^{\eta} (\bar{\rho} - \rho) g z \, \mathrm{d}z \tag{2.2}$$

with depth of the water column $H = \eta + h$ and $\bar{\rho}$, the depth-averaged density. It can be used to quantify the effect of mixing processes and to express the amount of stratification.

Mixing can transform a two-layer fluid into linearly stratified fluid into a continuously stratified fluid. A difference can be made between mixing and stirring. Mixing is a diffusive and irreversible process while a stirred fluid may later restore to the former condition under gravity (Peltier and Caulfield, 2003). In this case, the interest is in mixing. Mixing is thus an irreversible increase in potential energy of the density distribution (Fringer and Street, 2003). The efficiency of this energy conversion is expressed in parameter called the mixing efficiency. The mixing efficiency has different formulations which result in significant differences (Venayagamoorthy and Koseff, 2016). The flux Richardson number is often used as measure of mixing efficiency. It is defined as the ratio of the buoyancy flux over the rate of production of turbulent kinetic energy (Venayagamoorthy and Koseff, 2016) or as $R_f \cong B/(\epsilon + B)$ with vertical buoyancy flux B and dissipation ϵ (Geyer et al., 2008).

The mixing efficiency is not constant. It is dependent on among other factors the mixing mechanism Ivey et al. (2008). In the next sections, mixing due to stratified shear flow and mixing by internal waves are described in more detail. As an indication of the order of magnitude, the mixing efficiency found by earlier studies will be given as well.

2.1.2. Stratified shear flow

One of the processes that can lead to mixing by ship traffic is shear flow. Velocity differences could occur due to for example the return current or propeller jet of the the vessel. Velocity shear in between two layers causes entrainment of fluid from the other layer. This gives rise to a mixing layer in between the layers and a lower overall density difference. Turbulence is suppressed by the density differences, which gives the mixing layer a limited thickness. This process of entrainment and formation of a mixing layer can be seen in Figure 2.1.

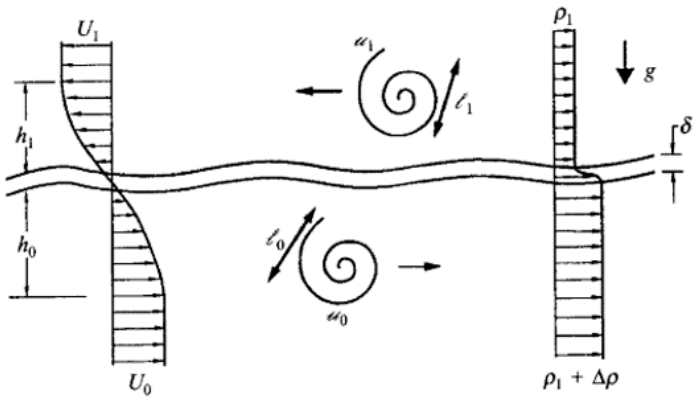

Figure 2.1: Density interface of an entraining two-layer shear flow with a mixing layer (Sullivan and List, 1994). There is a velocity difference and a density difference over the depth. The velocity difference causes shear between the layers of different density resulting into entrainment of the bottom and top layer in the mixing layer.

Several mixing regimes in shear flow can be identified, often based on a typical Richardson number (see for example Narimousa and Fernando (1987), Sullivan and List (1994), and Strang and Fernando (2001)). Several definitions of the Richardson number are in use. The gradient Richardson number is the buoyancy frequency squared divided by the square of the velocity shear and gives the ratio of buoyancy forcing to inertial forcing. The Richardson number is therefore an indication of stability. For gradient Richardson values larger than 0.25, the flow is stable (Kundu, 2013). The flow can be unstable for lower values of the gradient Richardson number.

$$Ri_g = -\frac{g}{\rho_0} \frac{\frac{\partial \rho}{\partial z}}{\left|\frac{\partial u}{\partial z}\right|^2} \tag{2.3}$$

Sullivan and List (1994) found that for low Richardson numbers a turbulent interface is visible between the shear layers. For higher Richardson numbers, asymmetric Kelvin-Helmholtz instabilities are

formed. For even higher Richardson numbers, wave breaking is found to be the main mixing mechanism and for even larger Richardson numbers, the mixing is diffusion-dominated (Sullivan and List, 1994). This is comparable to the regimes as identified by Narimousa and Fernando (1987) (large eddy formation to breaking internal waves). Narimousa and Fernando (1987) and Sullivan and List (1994) use a different definition of the Richardson number than defined above, the layer Richardson number, which is proportional to the gradient Richardson number (Narimousa and Fernando, 1987). The layer Richardson number is $Ri_u = \Delta b \delta / \overline{U}^2$, with $\Delta b = g\Delta\rho/\rho_0$, δ is the interface layer thickness, and $\overline{U}$ is the mean interface velocity.

Lawrence et al. (1991), Strang and Fernando (2001), and Hogg and Ivey (2003) identified additionally to the previous categories, a regime with an interaction between Kelvin-Helmholtz instabilities and Hölmboë waves and a regime of Hölmboë waves. The interaction of these wave-like instabilities causes them to break and cause mixing. Strang and Fernando (2001) used the bulk Richardson number, $Ri_B = \Delta b D / \Delta U^2$, as well as the gradient Richardson number defined above.

The gradient Richardson will be of more practical use in this study. Strang and Fernando (2001) gives the following limits: for $Ri_g < 0.36$ Kelvin Helmholtz instabilities are dominant, for $1 < Ri_g < 1.3$ asymmetric waves are dominant with a transition zone in between 0.36 and 1 in which both are present. The last regime identified by Strang and Fernando (2001) is for $Ri_g > 1.3$, in this regime Hölmböe waves are dominant.

The mixing process has an influence on the mixing efficiency. A mixing efficiency of 0.2 is for example typical for mixing by Kelvin-Helmholtz instabilities (Peltier and Caulfield, 2003), while an efficiency of 0.4-0.5 is found for a regime with both Kelvin-Helmholtz as Holmboë instabilities (Strang and Fernando, 2001). Strang and Fernando (2001) found that the most efficient entraiment occured at $Ri_g = 1$.

Comparison of the studies done is difficult because of the different definitions of the Richardson number and experimental set-up. It does show however that there are different regimes to be recognised in stratified shear flow. A gradient Richardson number lower than 0.25 (or 1 in some cases) can indicate instabilities.

2.1.3. Internal waves

As well as waves on the surface, ships in stratified flow can create internal waves. Internal waves are waves in the water column of a stratified flow. A special category of internal waves are the interfacial waves, waves that occur on the interface between layers of different densities. Internal waves carry energy and momentum, and when the waves break or become unstable due to shear instabilities energy can be dissipated or contribute to mixing.

Different types of waves give different types of breaking and dissipation mechanisms (Lamb, 2014). Interfacial waves in a two-layer flow and internal waves in a linearly stratified flow behave differently (Lamb, 2014). Internal waves in a continuously stratified flow can propagate both horizontally as vertically. This also affects the way these waves break and dissipate their energy. Internal waves can break as result of shear instabilities or a too high wave steepness (Staquet and Sommeria, 2002). These phenomena are shortly discussed here. Staquet and Sommeria (2002), Ivey et al. (2008) and Lamb (2014) give an extensive overview of current knowledge on internal wave breaking and dissipation.

Shear instabilities have already been described above. An internal wave will cause velocity differences which can lead to shear instabilities in the same way as is described above. For a two-layer fluid, the limit given in Equation 2.4 can be found using the phase velocity (Pietrzak, 2012). If this is true, the phase velocity is not complex. If the phase velocity becomes complex, the amplitude grows exponentially which causes wave breaking and mixing.

$$\Delta U^2 < (T_1 + T_2)\frac{\epsilon g}{k} \tag{2.4}$$

with ΔU^2, the velocity difference between the layers, $T_n = \tanh kh_n$ with wave number k and h_n the layer thickness, and $\epsilon = \frac{\rho_2 - \rho_1}{\rho_2}$. For short waves (with a large wave number), small velocity differences can already cause instabilities (Pietrzak, 2012). However, this is not valid inside the mixing layer formed by the breaking waves. Turbulence damping suppresses unlimited growth of the mixing layer. The Richardson number can be used to identify instabilities in the same way as described above for the stratified shear flow. However, there cannot be one minimum Richardson number to identify shear instabilities, this is dependent on the type of waves (Lamb, 2014).

Waves can also break by a too high wave steepness. The wave steepness is defined as the product of the wave number and the wave amplitude (Fringer and Street, 2003). Overturning occurs if the wave steepness is larger than a certain number. In this case, the maximum fluid velocity in the wave becomes larger than the wave speed and the wave breaks (Fringer and Street, 2003).

Waves can steepen by a slope in the topography. Inland waterways can have a rectangular, trapezoidal, or combined trapezoidal-rectangular profile (Verheij et al., 2008). Interaction of waves with the banks of the canal could cause the waves to break or reflect. Two parameters for wave breaking on a slope have been found, which will be discussed below. Both take into account the wave steepness and the slope of the topography.

Linear waves propagate horizontally and vertically. The slope of the internal wave characteristic, r, is given by the ratio of the horizontal wave number (k_h) to the vertical wave number (m) (Lamb, 2014). This is compared to the slope of the topography, s, to give three slope ratios (larger/equal/smaller than 1). Critical slope ratios ($s/r = 1$) cause the most dissipation and mixing. (Lamb (2014)).

Another definition is the internal Iribarren number as formulated by Boegman et al. (2005) and Aghsaee et al. (2010) (see Equation 2.5). It is a ratio of the geometry slope to the square of the wave steepness with the wave steepness the ratio of the wave amplitude (a) to the (half) wave length (L_w). Figure 2.2 shows different breaking mechanisms as used by Sutherland et al. (2013). Depending on the internal Iribarren number, a non-breaking, surging, collapsing, or plunging breaker is found. The highest mixing efficiency is found for plunging breakers (Boegman et al., 2005). Arthur and Fringer (2014) found an increase in dissipation and mixing for smaller or larger internal Iribarren numbers. However, Aghsaee et al. (2010) found the internal Iribarren number not to be a good classification tool for breaker types. Masunaga et al. (2019) also points to the use of wave slope to topographic slope to characterise breakers as shown by Aghsaee et al. (2010).

$$\xi_i = \frac{s}{\sqrt{a/L_W}} \tag{2.5}$$

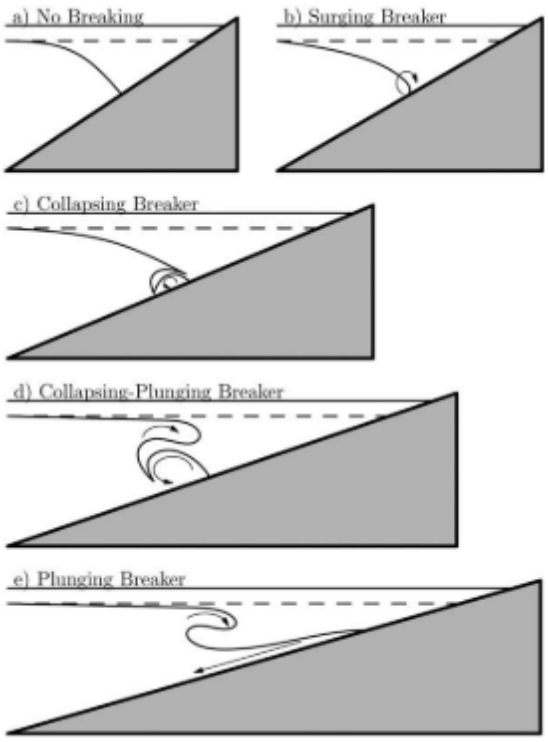

Figure 2.2: Different breaking mechanisms for solitary waves of depression as defined by Sutherland et al. (2013). The Iribarren number is decreasing from top to bottom as the slope steepness decreases for the same wave steepness. Figure from Sutherland et al. (2013)

Both definitions are very similar. They both use a ratio of the slope steepness over the wave steep-

ness. The s/r-ratio is mainly used for internal waves in a linearly stratified flow, while the internal Iribarren number is used in two-layer flows. It is unclear how much of the above definitions can be applied to internal ship waves in an inland waterway, however, there will be some interaction between internal waves and the canal banks which could result into mixing. As discussed above, internal waves can also contribute to mixing by shear instabilities.

2.1.4. Overview mixing mechanisms in stratified flow

Shear instabilities and wave breaking have been discussed as potential mixing mechanisms. The mixing efficiency is not a constant, and is dependent on many factors. The PEA can be used as a measure of the stratification in a canal. The gradient Richardson number can indicate shear instabilities in stratified flow. Low Richardson numbers, generally lower than 0.25, can indicate that the velocity shear is stronger than the buoyancy forcing. Internal waves can contribute to mixing due to velocity shear or a too high wave steepness, a product of the wave amplitude and wave number. A slope can cause a higher wave steepness, and several ratios of the topography slope and the wave steepness are in use to indicate breaking waves.

2.2. Ship-water interaction

Ships move water when sailing through a waterway. This induces three water movements: primary and secondary waves and propeller jet flow. This section is based on an overview of the theory as given by Verheij et al. (2008). Depending on, among other factors, ship dimensions in relation to canal dimensions, one of these effects is more significant. Figure 2.3 shows an overview of the water movement around a ship on a restricted waterway. The return current and associated front and stern wave is visible, as well as the Kelvin pattern of the secondary waves, and the wake of propeller. In this section, an overview of current knowledge on the flow field around a vessel for homogeneous and stratified flow is given.

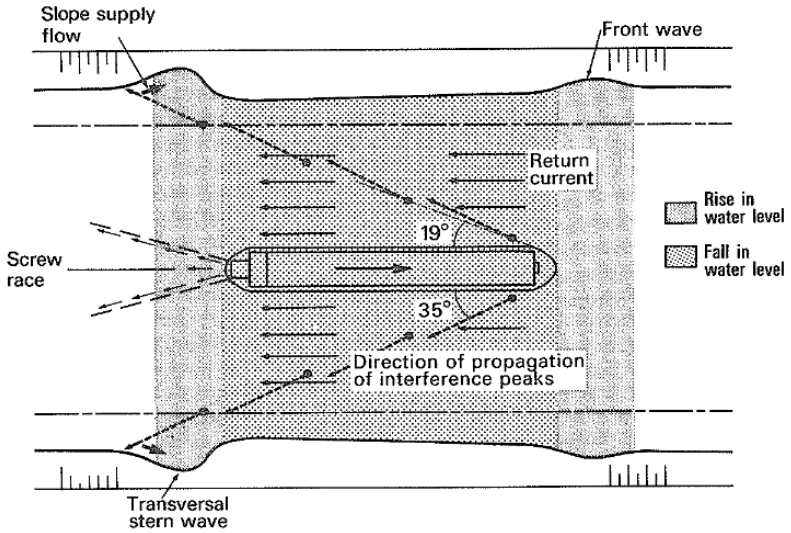

Figure 2.3: Overview of the water movement around a ship in a restricted waterway (figure 3.39 from PIANC (1987)).

2.2.1. Primary wave system and the return current

Unstratified canal

The primary wave system is caused by the water displacement of the ship. The bow pushes water away in the front, which results in a return current around the ship, and behind the vessel the water level comes up again in the stern wave. The return current results in a water level depression next to the ship and squat of the ship. Figure 2.3 shows the front and stern wave and the water level depression in between. The primary wave system can be seen as the large wave system which is bound to the vessel.

Several methods to describe these waves have been suggested. The most widely-used one is the method of Schijf from 1949 based on preservation of energy, Bernouilli, and continuity. This method can be used to calculate the return current. Other methods are based on the preservation of momentum, such as the one of Bouwmeester from 1977. Both these methods are described in more detail in Verheij et al. (2008). The return current is a function of the canal blockage, water depth, and vessel speed. These methods give a one-dimensional maximum velocity and not a velocity field.Verheij et al. (2008) gives empirical formulations for the transversal and vertical distribution of the return current. Beneath the bow, the return flow velocity is maximum. For small underkeel clearances, a large amount of water will move to the sides of the ship. Figure 2.4 gives a schematic overview of the flow around a ship for different vessel draught to water depth ratios. This picture shows well how the flow is diverted to the side of the vessel for different underkeel clearances.

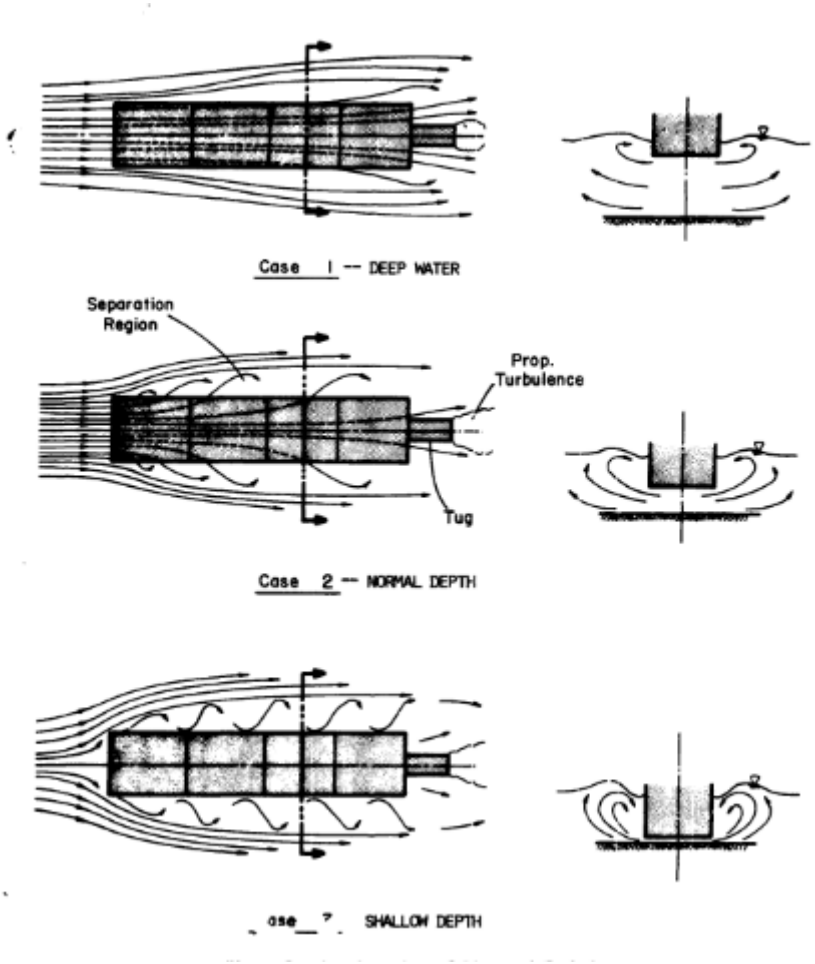

Figure 2.4: Schematised drawing of the return current for different water depths and vessel draughts (Figure 3 from Karaki and VanHoften (1975))

More complex flow patterns are created by ships sailing eccentrically and the combined effect of multiple ships in a canal. This can be found in Verheij et al. (2008).

Stratified canal

The return current in a stratified canal is less well documented. Most of the research on ships in stratified waters is focused on the flow pattern in oceans or waters of infinite depth and width. The primary wave does not play a dominant role in these systems. As discussed above the return current means a local change in velocity. This could lead to shear and possibly mixing. Furthermore, the flow underneath the ship's hull could lower or deform the interface. Another scenario is that the ship moves through the interface, disturbing it, which will result in mixing.

Stefan and Riley (1985) named barge traffic as most important source of turbulent mixing in a river with low flow rates. This is the case for both loaded and unloaded barges. It is unclear whether this is because of the return current or because of internal waves. Bijlsma (2020) made a calculation using the return current to estimate the effect of shipping traffic. An averaged loaded vessel (CEMT II Class V) in the ARK/NZK gives a return discharge of 220 m^3/s, which depending on the ship length and sailing speed is present for 16 to 22 seconds. However, for the maximum vessel this can go up to 456 m^3/s for 37 to 39 seconds. The return flow therefore causes a sudden large discharge locally, which might in turn create internal waves.

A parallel can be drawn with research on sailing over fluid mud and the nautical bottom. The main differences with a ship sailing over a layer of saltier water is that the density difference and viscosity is larger for the fluid mud case. Vantorre and Coen (1988) and Vantorre (1991) derive a one-dimensional estimate of the interface deformation and return flow velocities of a ship sailing over a fluid mud layer similarly to the derivation of Schijf in an unstratified canal. Three speed ranges are described in Vantorre (1991) and Vantorre (2001). At low speeds, no effect is visible on the interface. At intermediate speeds, the interface sinks first and then rises quickly to form an internal hydraulic jump. At higher speeds, the hydraulic jump does not occur underneath the vessel, but behind the stern.

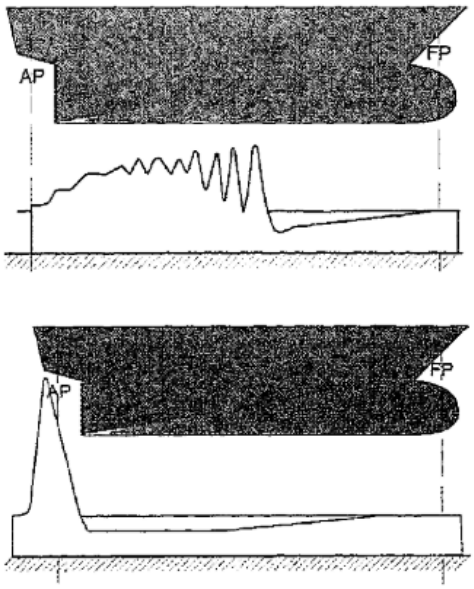

Figure 2.5: Illustration of the second and third speed range for a vessel sailing above a fluid mud layer from Vantorre (2001). In the first speed range, no interface effects are visible. In the second speed range, an internal hydraulic jump occurs underneath the vessel and in the third speed range, the hydraulic jump occurs behind the stern.

A parallel can also be drawn to research into the flow field and mixing by topography in stratified flow. Early laboratory research in that field is done by pulling a topographic feature through the top layer of a two-layer system (see for example Baines (1984)). The flow pattern found is dependent on the internal Froude number, and again for some situations hydraulic jumps are observed. The internal Froude number gives information about whether the flow state is sub-critical, critical, or supercritical, and whether hydraulic jumps will occur. As with the Richardson number, different definitions are in use. Baines (1984) used the Froude number is based on the towing speed of the obstacle and the local linear interfacial long-wave speed.

$$Fr_i = \frac{U}{c_0} \tag{2.6}$$

This could also be applied to a sailing vessel using the speed of the vessel relative to the velocity of the internal waves. The internal wave speed is dependent on the density distribution. The internal Froude number also gives information on the wave pattern behind the vessel. This is described in the next section.

Baines (1984) identified several regimes for two-layer flow over topography. These regimes can be seen in Figure 2.6. Depending on the flow state, the interface moves up or down in front, underneath or

behind the vessel. The flow pattern over the width is not considered in these experiments. A hydraulic jump could lead to mixing due to shear instabilities in the interface layer (Baines, 2016). Studies into the effect of topography on stratification give a first indication what could happen with the flow around a vessel. However, a ship is a 3D object in a waterway. The flow will therefore not only flow underneath the vessel, but also around the vessel. Snyder et al. (1985) identified a dividing streamline between streamlines that pass around from those that pass over a hill. This could be explained simplified by whether the kinetic energy is high enough to overcome the potential energy difference. The topographic features used in the previously mentioned studies are usually less high compared to the total water depth than a vessel in an inland waterway which might make a direct comparison impossible.

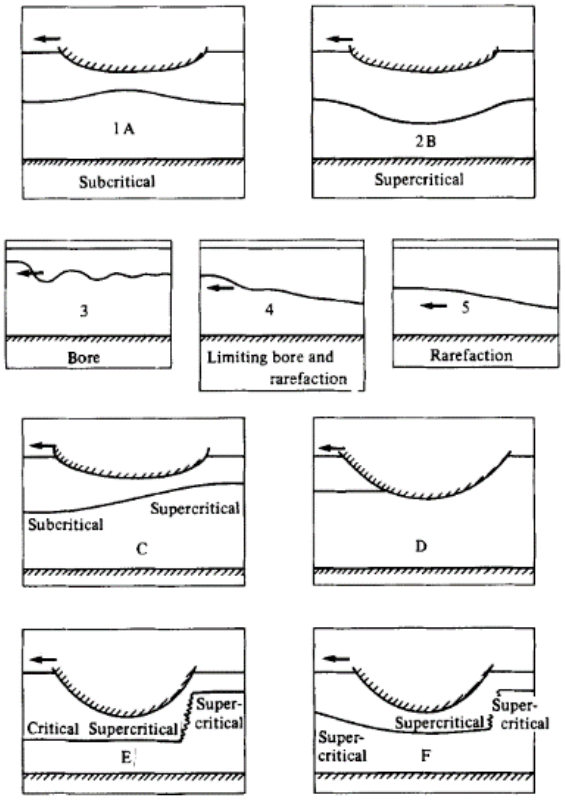

Figure 2.6: 2DV flow states in two-layer flow over a towed topographic feature as identified by Baines (1984). The flow state determines the response on the interface. The letters refer to the type of motion over the obstacle. The numbers 3 to 5 refer to the type of upstream disturbance. A bore is a moving hydraulic jump and a rarefaction is a wave that grows in length.

There are no studies found that study the return current of vessel in an inland waterway with salt intrusion. It is likely that there are resemblances with flow over topographic features and that the Froude number can be helpful in determining the flow state and flow response. The formulations derived by Vantorre and Coen (1988) could potentially also be used to estimate the flow velocities in a two-layer flow. It is unknown to what extent the return current concentrates in one layer for small density differences. If the return current would be concentrated in the top layer, large velocity differences could occur, which could contribute to mixing.

2.2.2. Secondary wave system

Unstratified canal

Secondary waves are the short waves caused by the disturbance of the vessel in the water, and consist of divergent and transversal waves (see Figure 2.7). The interaction between these two types of waves form inference cusps. The wave pattern changes for critical or supercritical conditions. At supercritical conditions, only divergent waves are present. The angle of the diverging waves is dependent on the Froude number ($U/\sqrt{gH}$). Barges and tankers in an inland waterway have low sailing speeds, and have therefore a subcritical wave pattern. (Verheij et al., 2008).

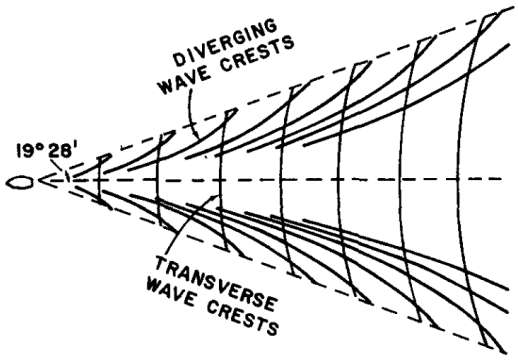

Figure 2.7: Typical deep water ship wave pattern (Figure from Sharman and Wurtele (1983))

Stratified canal

Similarly to the generation of waves on the surface, ships can also generate internal waves if they are sailing over a stratified flow. Several researchers have observed internal waves when a ship sails in a stratified canal (for example Stefan and Riley (1985)) or suggested that ship-generated internal waves have an important role in vertical mixing in a canal (for example Moser (1985)). As Bijlsma (2020) suggests the relatively large local return currents could generate internal waves.

Little research has been done on internal ship wave generation in a canal, more research is focused on waves in the ocean or pressure points or spheres in infinite depth. Similar results for surface waves are derived for a moving pressure point over two-layer system with an infinite bottom layer (Crapper, 1967), for a continuous density gradient (Sharman and Wurtele, 1983), and a moving source in two-layer ocean of finite depth (Yeung and Nguyen, 1999). Sano and Kunitake (2017) derived a similar set of equations for ships sailing over a fluid mud layer.

These studies found two regimes for internal ship waves: (1) diverging and transverse waves, (2) only diverging waves. The critical Froude number is dependent on the layer thickness and density difference. Figure 2.8 shows the result of one of the calculations of Yeung and Nguyen (1999), and shows that while the surface wave pattern is subcritical, the wave pattern between the two layers is supercritical. Chang et al. (2006) showed a smaller Kelvin angle for an increase in Froude number as well as an increase in internal wavelength using numerical simulations for a submarine in a two-layer fluid. The numerical calculations of Esmaeilpour et al. (2016) showed that the distance to the interface is an important parameter in the generation of ship-generated internal waves. They also showed an increase in resistance due to the energy input needed to generate the internal waves.

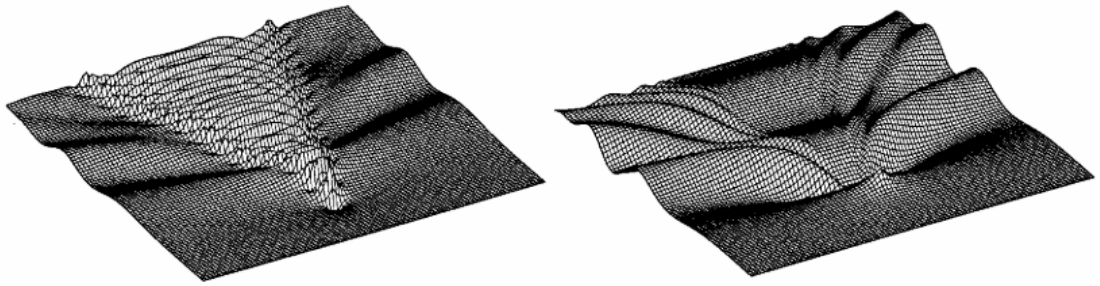

Figure 2.8: Example of a surface (left) and internal (right) wave pattern by a moving source in an ocean of finite depth as found by Yeung and Nguyen (1999). The surface wave pattern has diverging and transverse waves, while the internal wave pattern is supercritical.

A question that is still open is how much of this research can be directly applied to flow in restricted waterways. Moreover, it is still unclear how the internal waves contribute to mixing in restricted waters. Do the internal waves break on the canal bed or banks or do they become unstable? What is the mixing efficiency of the waves?

2.2.3. Propeller jet flow

Unstratified canal

A third effect is that of the jet flow of the main propellers and manoeuvring thrusters. The jet flow from these thrusters will not be taken into account here, as they are mainly used for (de-)berthing in harbours (Verheij et al., 2008). Most inland waterway vessels in the Netherlands have one or two main propellers placed in a tunnel shaft (Ten Hove, 2008). The main propeller draws in surrounding water and propels it downstream to move the ship forward. It produces a high flow velocity jet and an increase in turbulence. The diameter of this propeller is about two meters (Verheij et al., 2008). A tunnel shaft increases the efficiency of the propeller. A rudder is placed behind the propeller to be able to manoeuvre the vessel. The jet velocity will decay with distance from the propeller by entraining surrounding fluid as can be seen in Figure 2.9. Jet flow has a zone of flow establishment (ZFE) and a zone of established flow (ZEF) (Lam et al., 2011)

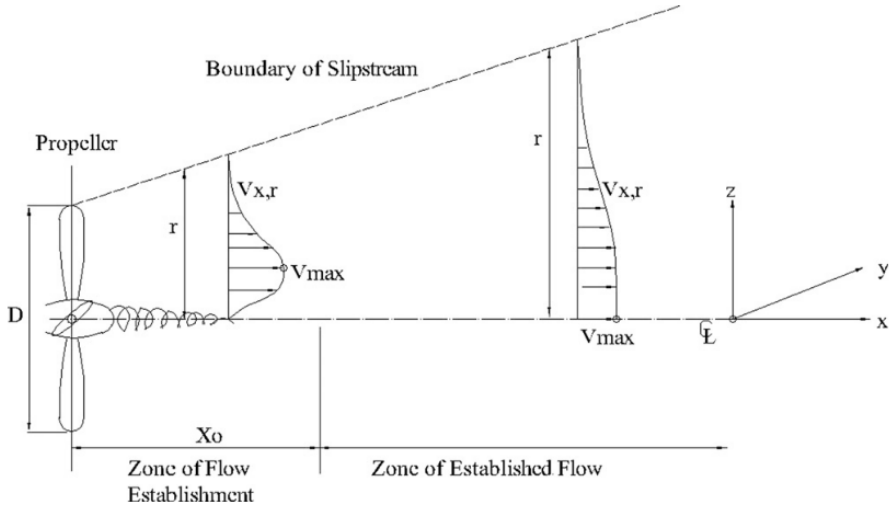

Figure 2.9: Jet flow produced by the main propeller (Figure from Lam et al. (2011))

A more elaborate discussion on the flow field caused by a propeller jet in homogeneous flow can be found in Verheij et al. (2008) and Lam et al. (2011). More information on mixing caused by jet flow can be found in Fischer (1979).

Stratified canal

In Figure 2.10, a typical wake of a vessel is visible. The dashed line shows the wake for a homogeneous fluid. For stratified flow, turbulence is suppressed and the wake reaches less deep. A pressure drop in the wake drives entrainment causing the wake to grow with distance from the vessel. The wake of a vessel in stratified fluid is therefore relatively flat compared to the half-round shape of a wake in homogeneous flow. (Voropayev et al., 2012). A wake does survive longer in a stratified fluid because of the reduced turbulent production as found by Brucker and Sarkar (2010). Furthermore, the addition of a propeller will change the wake of the vessel as the wake of a self-propelled and a towed sphere is different (see Figure 2.11). The velocity shear of the propeller jet with the surrounding fluid creates turbulence and mixing.

Propeller power is often used as an estimate of the mixing caused by ships in stratified water (see for example Moser and Bakker (1989), Karelse and Van Gils (1991), and Maderich et al. (2008)). Moser and Bakker (1989) find an efficiency coefficient of two to ten percent for the conversion of propeller energy to potential energy or mixing, which is a relatively large efficiency factor. Stefan and Riley (1985) concluded that for a small tow boat the direct mixing of the propeller is more important than the water displacement by the hull. The effect is, however, small and local. For unloaded barges, the addition of a towboat (with a propeller) increased the mixing. For loaded barges, the effect was not observed and the return current is dominant over the towboat jet flow. Esmaeilpour et al. (2016) concluded that in the near field the wake is mostly influenced by the disturbance of the hull and the propeller mixing.

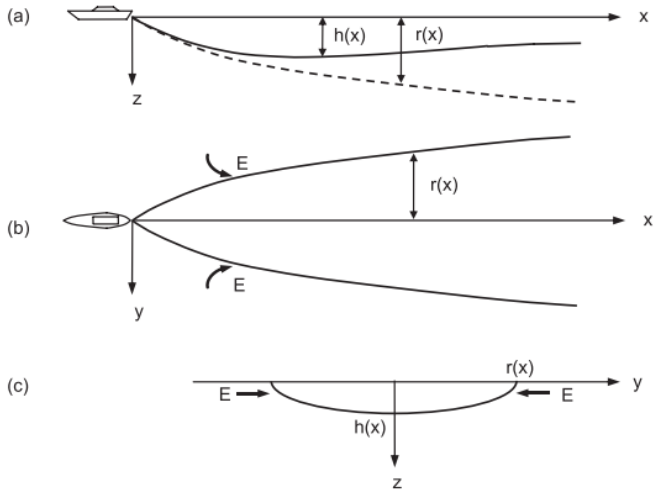

Figure 2.10: Schematised wake of a ship in a stratified fluid. It is shown that the wake depth decreases for a stratified fluid as compared to a homogeneous fluid (dashed line). Lateral entrainment is shown in b) and c) (Figure 2 from Voropayev et al. (2012))

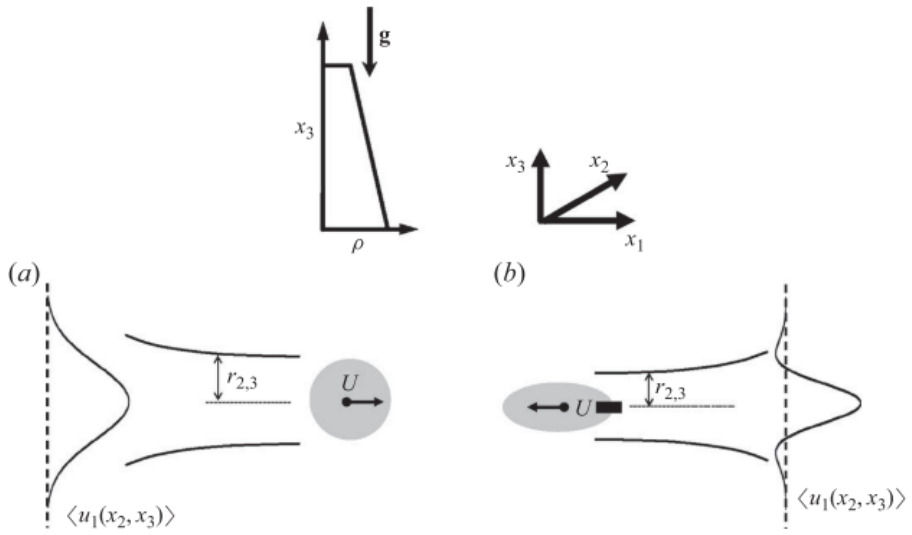

Figure 2.11: Towed (left) and self-propelled, jet-driven (right) bodies give a different wake flow. Note the opposite velocities in the wake relative to the direction of the body. Figure from Brucker and Sarkar (2010).

2.2.4. Overview of ship-water interaction

The interaction between a sailing ship and the surrounding water has been described in three parts. The primary wave system and return current are caused by the displacement of water by the ship. The primary wave system in stratified water is not well documented. The return current could give rise to velocity differences between the layers, which might lead to an internal hydraulic jump behind the vessel or instabilities. The internal secondary wave system shows probably a wave system in the shape of a V behind the vessel. The propeller jet flow is the third effect that is discussed above. The propeller jet causes increased velocity and turbulence behind the vessel. In the next section, the implications for mixing are discussed, as well as the currently unknown factors.

2.3. Discussion of possible ship-induced mixing processes

Mixing is an energy transfer from kinetic energy to potential energy. An important question is how much of the energy is used for mixing, the mixing efficiency. Stratification has a damping influence on the turbulence, which results in less mixing compared to an unstratified flow. This chapter shows that there is a complex flow field around a ship in restricted, stratified water. Several processes have been identified as possible mixing processes. The return flow leads to locally high velocities around the vessel with possibly velocity shear in between the layers or a hydraulic jump behind the vessel. The flow instabilities can consequently lead to mixing. The stability of the flow can be expressed with help of the Richardson number. A ship sailing over or through a stratified fluid will leave internal waves in its wake, which have been well described in literature. Internal waves can result in mixing due to shear instabilities, a too high wave steepness, or breaking on a slope. A third possible mixing process is mixing due to the propeller jet.

From this literature study, no conclusion can be drawn on which mechanisms would be the most relevant for mixing in a canal. In general, little research has been done into ship-induced mixing in stratified waters, especially not for inland waterways. The return current is important because of the limited dimensions of an inland waterway. It is however unknown how the return current is distributed over the depth for a stratified flow and how much the return current contributes to mixing. Although the wave pattern behind a vessel has been well described in literature, little knowledge is available on the effect of these waves on mixing. The limited dimensions of an inland waterway will cause reflection or breaking of the waves on the banks of the canal. However, the characteristics of the waves and therefore the expected mixing resulting from this is still unclear. It is also unclear how much instabilities in the wave field would lead to mixing. Propeller jets entrain surrounding fluid and are a source of turbulence. Previous research has stated that the influence of the propeller jet is small for barges and limited to the near field of the vessel.

This chapter therefore concludes the following about the processes mentioned in the beginning of the chapter.

- **Return current**
  The knowledge on the return current in a salinity-stratified canal is very limited. Possible mixing processes are shear instabilities between the layers and hydraulic jumps.
- **Internal waves**
  The knowledge on internal ship waves is large for the open ocean, but little is known about the process in stratified canals. Possible mixing processes in a stratified canal are shear instabilities and wave breaking on the canal banks.
- **Propeller jet**
  The knowledge on the propeller jet is also relatively large for the open ocean. Knowledge of the process in stratified canals is limited. The propeller can contribute to mixing due to shear instabilities.

This literature study shows that there are still many questions to be answered to give a clear answer to the question how and how much ships sailing in an inland waterway contribute to mixing. The return current, internal waves, and the propeller jet will have an influence on the stratification. The relevant order of magnitude of these processes is still unclear. The next chapter of this report will give an estimation of the order of magnitude of mixing in typical inland waterways and zoom in on the governing parameters for the return flow, internal waves, and propeller jet. What is the effect of these parameters and how will they influence mixing in an inland waterway? This will also form the basis of the numerical

study later on in this study which will give a better picture of the flow field around a vessel in stratified inland waterway and the resulting mixing.

3

Canal characteristics and parameter influence

In the literature study, three possible causes of mixing have been identified: shear in between layers, internal wave breaking, and propeller mixing. In this chapter, the contribution of these processes is further investigated. Two canal systems are introduced to give insight on typical dimensions and orders of magnitude of the processes. Next, two examples are given to illustrate and estimate how large the contribution of ship traffic to mixing in these canals is. Next, formulas to describe the processes are given, and the influence of the main parameters on mixing is discussed. The outcomes of this study are later tested in numerical model runs.

3.1. Typical canal characteristics

The Noordzeekanaal (NZK), Amsterdam-Rijnkanaal (ARK) and Antwerps Kanaalpand (AKP) are introduced below as typical examples of Dutch canals with salt intrusion. The geometry, typical discharge, salinity profile as well as vessel distribution are discussed. These values will later be used to calculate the order of magnitude of the different processes in this chapter and to design the numerical calculations in the next chapter.

3.1.1. Noordzeekanaal and Amsterdam-Rijnkanaal

The NZK runs from Amsterdam to the North Sea. It is connected to the North Sea by locks at IJmuiden, and through lock exchange processes the NZK is brackish. In Amsterdam, the NZK connects to the river IJ and later the Amsterdam-Rijnkanaal (ARK). The discharge from the ARK prevents salt from the NZK intruding in the ARK. (Verbruggen and Buschman (2020)).

From IJmuiden until the Coentunnel, the water depth of the NZK is at least 15 m in the shipping lane. From there, it decreases step-wise to 6 m in the ARK. There is a large depth difference between the two canals, which can act as a sort of barrier for the saltier lower layer in the NZK. This depth-profile can be seen in Figure 3.2. The width of the NZK is about 250-300 m at the top without taking into account side canals and ports, and about 170 m at the bottom. The ARK is about 100 to 120 m wide. (Verbruggen and Buschman (2020)).

The discharge over the NZK varies a lot over the length as there are a lot of in- and outlets. The discharging at low water at IJmuiden creates a pseudotide at the canal. (Verbruggen and Buschman, 2020). Kikkert (2015) gives a multiple year-average of 65.5 m^3/s to 95.6 m^3/s with the note that the variation between and in the years is large. Based on that analysis, a range of 68 to 84 m^3/s multiple year-averaged is taken into account in Bijlsma and Weiler (2016). Verbruggen and Buschman (2020) gives a maximum peak discharge at IJmuiden of 700 m^3/s in 2018. This is a rare value. A peak discharge of (a few) hundred m^3/s is normal, with 500 m^3/s as the maximum peak discharge. These discharges give a velocity range of 0.021 to 0.15 m/s averaged over the cross section of the NZK.

The discharge from the ARK is used to counter salt intrusion from the NZK in the ARK. This discharge varies a lot over a day. The average multi-year discharge over the ARK at Weesp is 37 m^3/s

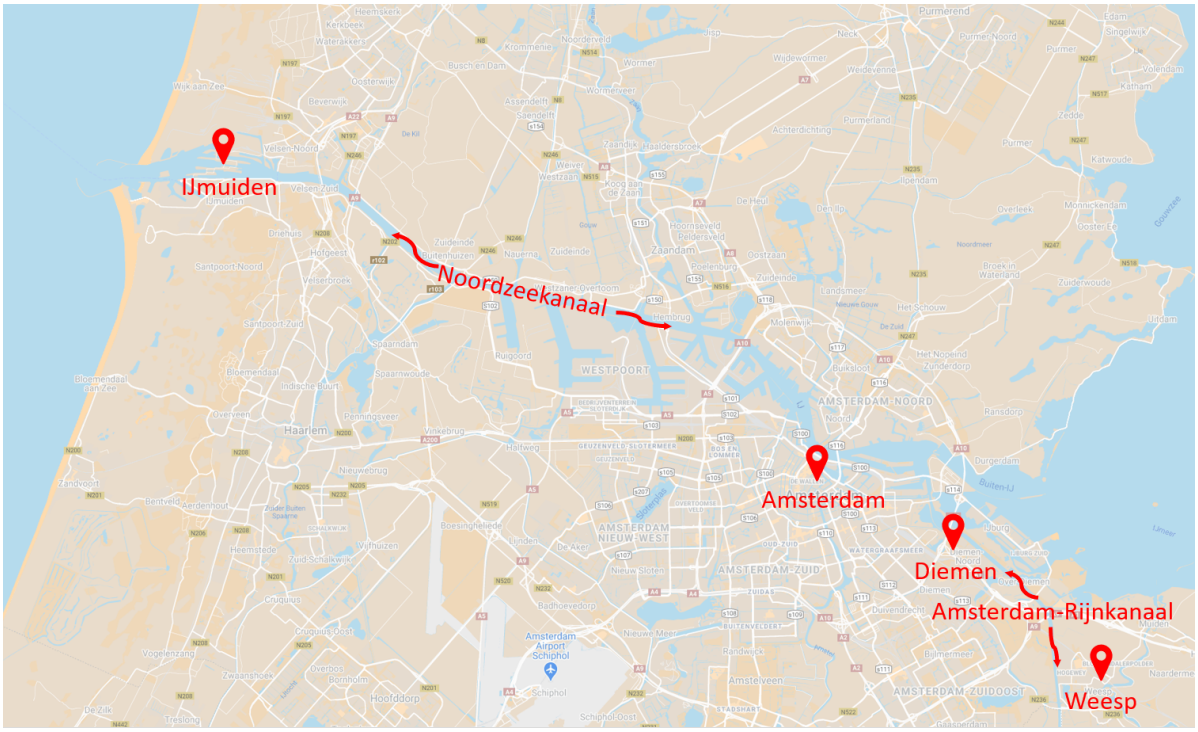

Figure 3.1: The Amsterdam-Rijnkanaal flows into the IJ in Amsterdam which continues into the Noordzeekanaal. The Noordzeekanaal is connected to the North Sea via the IJmuiden locks. (Map: Google Maps)

with peaks in 2018 up to about 120 m^3/s (Verbruggen and Buschman, 2020). This gives a velocity of 0.056 to 0.18 m/s averaged over the cross section of the canal.

The salinity profile in the NZK shows a salt wedge. Figure 3.2 shows the 100-point measurements done in the NZK and ARK from the 3rd to the 8th of September 2018. This was a dry period in the Netherlands. It shows fresh water at the ARK-side and a maximum of 22 PSU in the NZK. In the appendix, Figure A.1 and Figure A.2 show the results of measurements in July and August 2015. This shows the salinity distribution is dynamic and dependent on (among other factors) the discharge of the ARK.

As has been shown above, a lot of factors influence the salinity distribution in the NZK. The operation of the discharge sluices and pumps introduces a tide dependent motion in the system called pseudo tide and translation waves. There are several in- and outlets and much ship traffic. Information on the vessel distribution on the NZK is available from the PONTIS system. This system records the lock processes and passing vessels at the sea locks at IJmuiden from which data from the years 2013 and 2014 is available. The analysis done by Rietveld (2015) shows that the traffic intensity varies much per weekday, week, and year with both years showing the same trends. This data set gives an indication of the intensity of the ship traffic on the NZK. Averaged over both years, yearly 38172 vessels go through the locks which gives an average of 4.4 ship per hour. Hydrologic (2020) give an estimation of about 150 ships a day passing Weesp at the ARK, which translates to an average of 6.25 ships an hour. The maximum sailing velocity is 18 km/hour for most parts of the NZK and ARK.

The NZK and ARK are both designed for a VIb vessel (Rijkswaterstaat, 2020a). A maximum allowed ship on the NZK (km 0 to 18.1) has a length of 325 m, a width of 42 m, and a draught of 13.1 m (Rijkswaterstaat, 2020a), giving a blockage factor of 0.17. The data from the IJmuiden locks gives as most occurring vessel port tugs, followed by (inland) cargo ships and tankers. The median vessel has a length of 73 m, width of 10 m, and a draught of 3.5 m, which gives a blockage factor of 0.011. For the ARK, maximum allowed dimensions are 200 x 23.5 x 4.0m (Rijkswaterstaat, 2020a), giving a blockage factor of 0.14. Further information on ship measurements in Dutch waterways can be found in Koedijk (2020).

The return currents for typical vessels given by Bijlsma (2020) result in 0.067 to 0.14 m/s averaged over the cross section of the NZK and 0.33 to 0.69 m/s averaged over the cross section of the ARK.

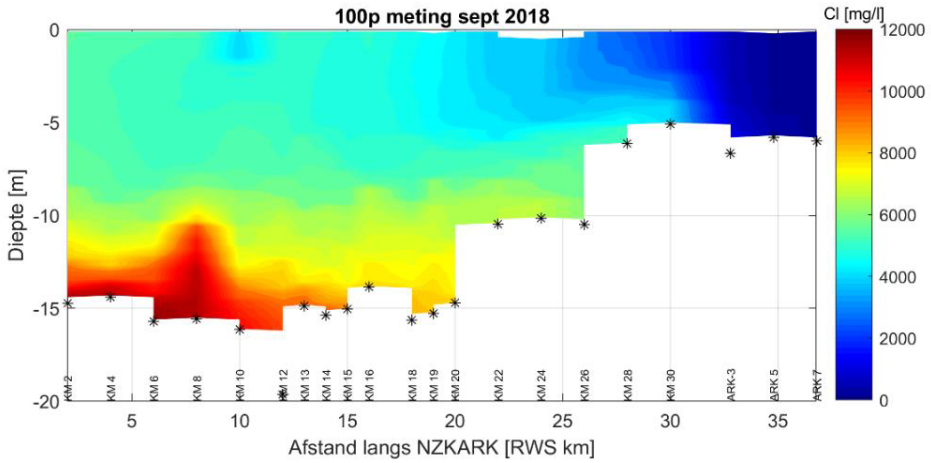

Figure 3.2: 100-point measurement in the NZK and ARK in September 2018, the stratification is clearly visible. IJmuiden is at RWS km 2 and Diemen at RWS km 33. Figure from Verbruggen and Baan (2020).

For a short duration, ships therefore generate currents of the same order of magnitude as the peak discharge in the canals. In reality, the return current of a vessel is not equal over the cross section of the canal. The highest velocities are found underneath the vessel. The return current gives therefore relatively high velocities for a short duration in the canal.

A summary of the data of the Noordzeekanaal and the Amsterdam Rijnkanaal is given in Table 3.1

		NZK - IJmuiden	ARK - Weesp
Salinity profile		Well-mixed until -10 m depth followed by a linear profile	(Usually) fresh water
Density difference	kg/m^3	10	-
Depth	m	15	6
Width	m	170-270	100-120
Average discharge	m^3/s	68-84	37
Peak discharge	m^3/s	500	120
Ship traffic	ship/hour	4.4	6.25
Maximum sailing velocity	km/hour	18	18
Maximum blockage factor		0.17	0.14

Table 3.1: Data from the Noordzeekanaal and the Amsterdam Rijnkanaal.

3.1.2. Antwerps Kanaalpand

The Antwerps Kanaalpand is part of the Schelde-Rijnkanaal, and connects the Volkerak and the Zoommeer to the Port of Antwerp. A 'pand' is the part of a canal in between two lock complexes. In this case, that is the part between the Kreekraksluices (NL) and the locks in the Port of Antwerpen (BE). Through lock exchange processes to the Schelde, salt comes in the southern part of the AKP. The salinity level is dependent on the Schelde river discharge.

The bottom of the canal is about 120 to 150 m wide and has a width of about 160 m at the top. The canal has a depth of minimum 5 m. The AKP is 14 km long. (Steenepoorte (2016)). The target water level north of the locks is 0.00 m NAP and the target water level at the AKP is +1.80 m NAP (Steenepoorte (2016). The chloride-level close to the locks is about 400 mg/l, while about 5 to 10 km

Figure 3.3: The Antwerps Kanaalpand connects the Volkerak and the Zoommeer to the Port of Antwerp. (Map: Google Maps)

further in the AKP the chloride-level is about 3500 mg/l (van Page et al. (2018)).

The lock complex also has a pumping station. This pumps fresh water into the AKP to prevent salt intrusion via the sluices to the Zoommeer. The locking processes would allow about 9 m^3/s to intrude the Zoommeer. However, because of the pumping station, there is a resulting average discharge of 3.5 m^3/s into the AKP. (van Page et al., 2018). This gives a cross section averaged velocity of 0.010 m/s.

In Figure 3.4, monthly chloride measurements in the Antwerps Kanaalpand in 2019 are shown. As can be seen there is a large variability over the year, even though the boundary conditions stay relatively constant. How far the salt intrudes in the canal varies as well as the slope of the isohalines. This is dynamic over the year and between different years.

Next, the ship traffic through the AKP is discussed. 69.000 vessels passed the Kreekrak locks in 2015 of which 67.000 were commercial inland vessels and 2.000 recreational vessels (Steenepoorte, 2016). That is 184 commercial vessels per day and 7.6 commercial vessel per hour on average.

An AIS data set for January 2018 of Rijkswaterstaat is available. The data is collected at the entrance of the Eendracht canal. It is assumed that almost all ships entering the Eendracht canal will continue their journey from the Eendracht to the port of Antwerpen through the AKP. Bruggeling et al. (2014) has made an analysis of the ship traffic through the Krammer locks. This showed almost no variability over the year for commercial ship traffic. It is therefore assumed that this is also the case for the ship traffic through the Kreekrak locks and that the data of January 2018 gives a good indication of the ship traffic.

Analysis of the AIS data shows that the predominant vessel types are cargo and tanker vessels with a dominant length of 110 m and a width of about 11 m. This corresponds to a Va ship. Motor cargo vessels of the Va class have a loaded draught of 3.5 m and unloaded draught of 1.8 m (Koedijk, 2020), giving a blockage factor of 0.06 and 0.03 respectively. The waterway is designed for VIb vessels and the maximum allowed vessel is 225x23.5x4.3 m Rijkswaterstaat (2020a), giving a maximum blockage

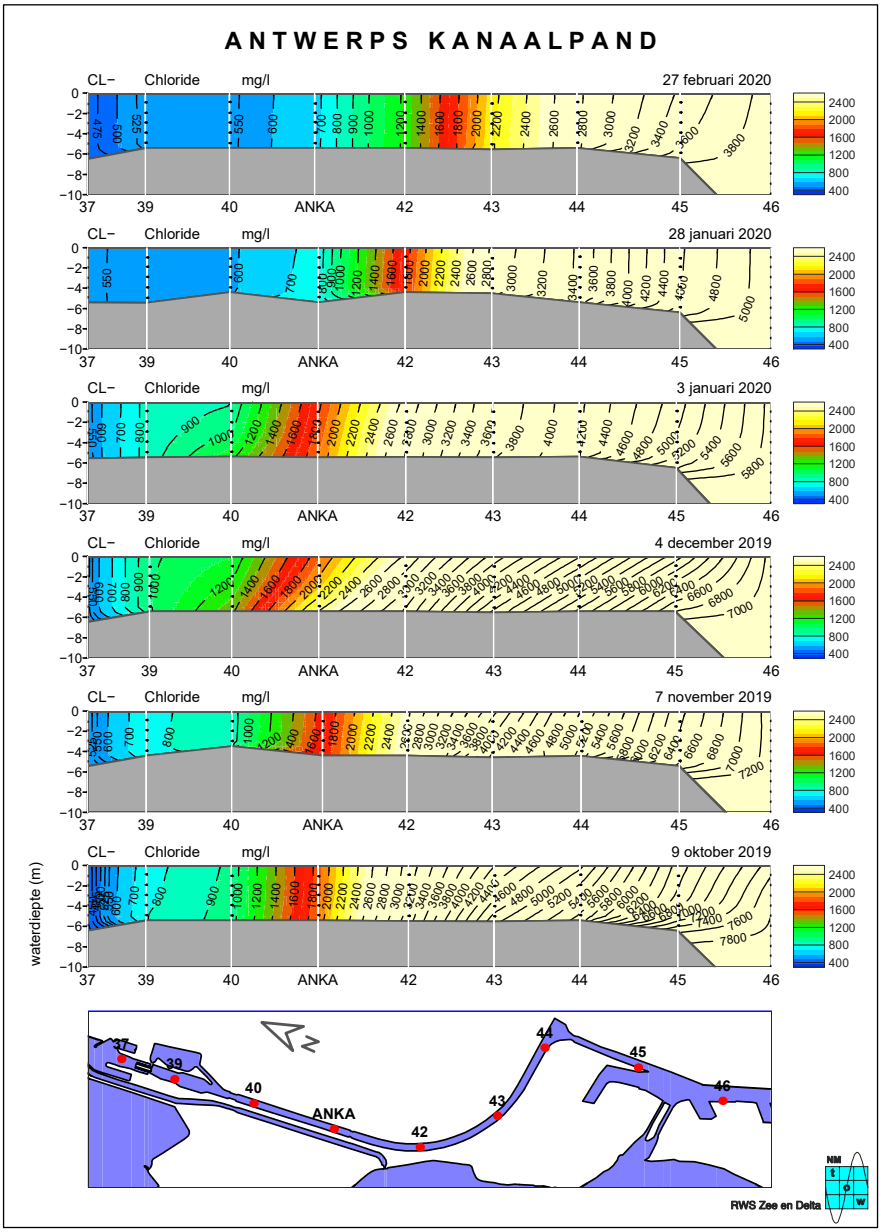

Figure 3.4: Monthly chloride measurements (mg/L) in the Antwerps Kanaalpand in 2019 (Figure from Waterberichtgeving Rijkswaterstaat (16/04/2020)

factor of 0.14.

The return current velocities are about 0.12 to 0.84 m/s when using the diagram of Schijf given in Verheij et al. (2008) with the above blockage factors and a sailing velocity of 3 m/s. The return current velocities are thus one order of magnitude larger than the discharge velocity. Locally, the return current velocities are even higher.

Table 3.2 summarises the data of the Antwerps Kanaalpand.

		AKP
Salinity profile		Well-mixed over the vertical
Density difference	kg/m^3	0-2
Depth	m	5
Width	m	140
Average discharge	m^3/s	3.5
Ship traffic	ship/hour	7.6
Maximum blockage factor		0.14

Table 3.2: Data from the Antwerps Kanaalpand.

3.2. First estimates of effect ship traffic on mixing

The previous section introduced the NZK, ARK, and AKP and shows that ships generate locally high return current velocities compared to the discharge in the canals. Below, two examples are given of the effect of ship traffic on the mixing of salinity. First, the case of the blockage of the Eendracht canal in 2014 is given. The time-period of the blockage corresponds to a period of more stratification in the nearby AKP. Secondly, an estimate of the contribution of wind, bottom shear, and ship traffic to mixing is given for the NZK, ARK, and AKP.

3.2.1. Effect of a waterway blockage on a salinity profile

In October 2014, the Schelde-Rijnkanaal was partly blocked for ship traffic due to a sunken vessel in the Eendracht, close to Nieuw Vossemeer. The Eendracht is in between the Volkerak and the Zoommeer, to the North of the AKP. The waterway was completely blocked for one day (from the evening of the 2nd to the 3rd of October during the day), followed by a week of little ship traffic and again a complete blockage of the waterway for a short duration for the salvage of the sunken vessel on the 8th of October[1,2]. Limited ship traffic was still possible and the total time of the blockage was relatively short, still an effect seems to be visible in the AKP.

Figure 3.5 shows the difference between the 10-minute averaged chloride levels in the AKP. A clear peak in the difference between the top and bottom sensor is visible in the period of the blockage, meaning that there was a larger difference in the salinity of the top and bottom layer of water, and that there was more stratification. It is a clear event and not a measurement error. It is clearly visible that the differences increases during the time that the waterway was fully blocked. It takes about a day until the canal is well-mixed again. In following week, no clear effect is visible from the decrease in ship traffic. No effect is visible of the second complete blockage of the waterway on the 8th of October. This blockage was estimated to last four to six hours [3]. The second peak visible in the blockage period could be assigned to lower ship traffic during the weekend. Hydrologic (2020) also noted a weekend pattern in the chloride-levels at Diemen (ARK) as well as in the ship traffic intensity.

The peak between the 3rd and 4th of October is the highest peak recorded in five years. In other years (see Appendix B), large differences have also been observed, however these occur generally in a period with more large peaks. The absence of ship traffic thus resulted in an increase of the stratification. This would indicate that the ships usually contribute to mixing in the canal, in combination with wind and bottom shear. It gives a hint that ship traffic might be crucial in keeping the AKP fully mixed.

[1] NU, 'Stremming Schelde-Rijnkanaal voorbij', https://www.nu.nl/binnenland/3898591/stremming-schelde-rijnkanaal-voorbij.html (last accessed on 24/02/2021)

[2] TotaalTrans, 'Stremming Schelde-Rijnkanaal vervroeg naar woensdag zes uur', http://www.totaaltrans.nl/stremming-schelde-rijnkanaal-eerder/ (last accessed on 24/02/2021)

[3] See footnote 2.

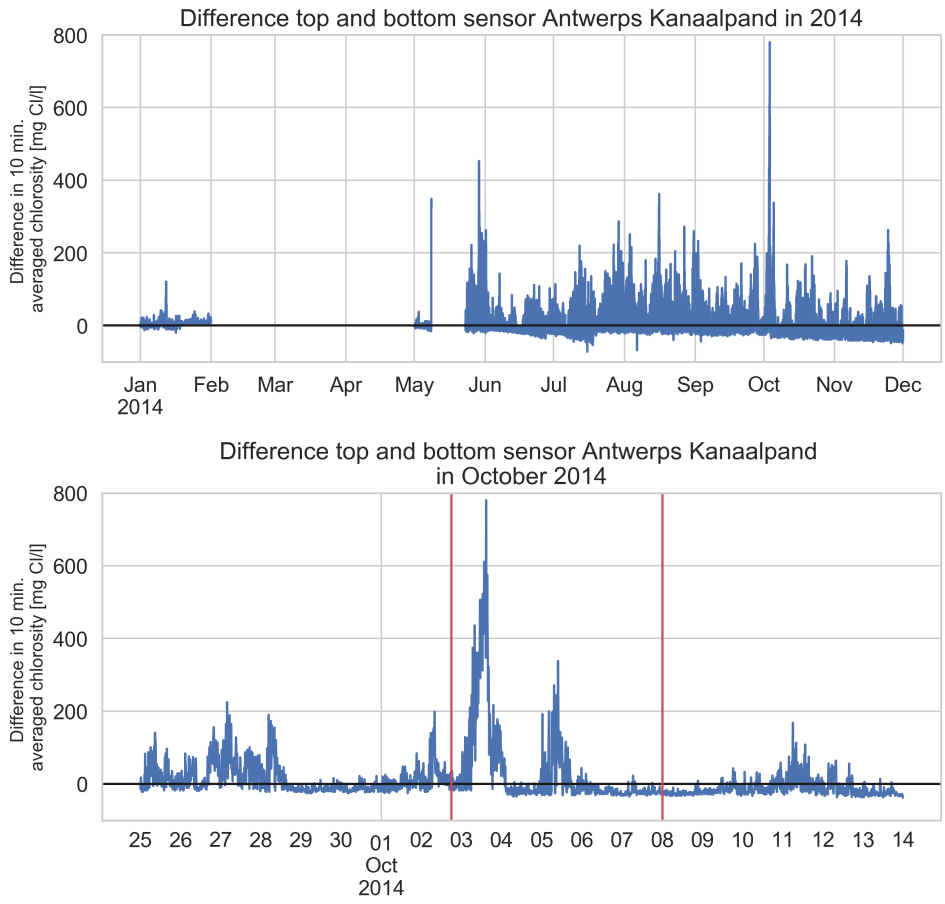

Figure 3.5: Difference between the top and bottom chloride-sensor in the Antwerps Kanaalpand (data from February to May missing). The time period of blockage is indicated in red. From the evening of the 2nd to the 3rd of October the waterway was completely blocked. (Data from Rijkswaterstaat (2020b))

3.2.2. Estimation of energy dissipation by mixing processes

Karelse and Van Gils (1991) made an estimation of the energy dissipation by wind, current and ships in the NZK. Propeller power was used to estimate the energy input of the ships, making the assumption that the amount of mixing is directly related to the amount of propeller power. Their conclusion was that wind and current contribute equally to mixing and ship traffic one or more orders of magnitudes more. The calculation is done here again for more recent numbers for the Noordzeekanaal at IJmuiden (KM2), the Amsterdam Rijnkanaal at Diemen (KM28), and the Antwerps Kanaalpand.

The energy dissipation for the three processes is calculated per km length of canal. The energy dissipated by the current is calculated by the shear stress (τ) times the width of the canal (W_c) times the depth-averaged velocity (U). The shear stress is calculated using the average density (ρ), gravitational acceleration (g), coefficient of Chézy (C), and the depth averaged velocity.

$$\frac{dE_c}{dt} = w_c \tau U \text{ with } \tau = \rho \left(\frac{g}{C^2} \right) U^2 \tag{3.1}$$

Karelse and Van Gils (1991) used the maximum depth-averaged velocity, as this will give the highest bottom shear and the most mixing. The depth-averaged velocity is calculated using the maximum discharges. The discharge of the AKP is relatively stable over time, therefore, no maximum discharge is available, so an average discharge is used.

The energy dissipated by the wind is given by the wind shear at the surface times the velocity at the surface times the width of the canal. Karelse and Van Gils (1991) used a relation between the wind shear and wind velocity and a relation between the wind velocity and current velocity at the surface,

which results in the following formula:

$$\frac{dE_w}{dt} = (0.6 \cdot 10^{-4} \text{ to } 0.9 \cdot 10^{-4}) \cdot Bw_c^3 \tag{3.2}$$

A wind speed of 5 m/s is used in all the calculations.

The energy dissipated by boats is calculated using the average number of boats present in the canal at a certain time (n) and the average propeller power (P).

$$\frac{dE_s}{dt} = nP \tag{3.3}$$

The number of vessels present in the canal length is estimated using the recorded vessel passages and the average sailing speed combined to find the average number of vessels in a km-length of canal. A sailing speed of 4 m/s is chosen as representative. The propeller power is equal to the values used by Karelse and Van Gils (1991).

In Table C.1, an overview of the input data is given.

This energy is only partly attributing to an increase in potential energy in the water, so only a part of the energy dissipation contributes to mixing. Karelse and Van Gils (1991) use a efficiency of one percent for all three phenomena. This is a rough estimate. The efficiency of mixing by ships is based on the work by Moser and Bakker (1989). This study found a range from two to ten percent, so the value used is conservative. This results in the following order of magnitudes for the energy converted into mixing.

	Noordzeekanaal	Amsterdam Rijnkanaal	Antwerps Kanaalpand
Current	$\mathcal{O}(+1)$	$\mathcal{O}(+1)$	$\mathcal{O}(-4)$
Wind	$\mathcal{O}(+1)$	$\mathcal{O}(+1)$	$\mathcal{O}(+1)$
Ships	$\mathcal{O}(+3)$	$\mathcal{O}(+2)$	$\mathcal{O}(+3)$

Table 3.3: Order of magnitude estimate of contribution to mixing in the Noordzeekanaal at IJmuiden, the entrance of the Amsterdam-Rijnkanaal, and the Antwerps Kanaalpand per km. Note that for the AKP only the average discharge was available which has led to a very low contribution of the current to mixing.

The low contribution of the current in mixing in the Antwerps Kanaalpand can be explained by the low discharge compared to the other canals. Mixing by vessels gives by far the largest contribution to mixing in these canals according to this method, however, it should be noted that this is a very rough estimation. First of all, the mixing efficiency is a rough estimation. Secondly, the formulas for the three processes can only give a rough estimation. It is unclear whether the energy input by the propeller of a vessel can be directly related to the amount of mixing. The increased velocities due to the return current are for example not taken into account in this estimation. Thirdly, the values used are, although based on data of the canals, only estimations.

Both the example of the canal blockage in the Eendracht as the above estimation show that ship traffic has an important role in mixing of salinity. These examples do not show which processes are responsible for mixing by ship traffic. In Chapter 2, the return current, internal waves, and the propeller jet have been identified as possible processes. The next sections will further study these processes to identify which parameters will play a role in these processes in inland waterways.

3.3. Processes: Return current

It might be possible that in a two-layer system, the return current creates shear between the layers. This might create instabilities, overturning, or an internal backwater curve resulting in mixing. The question is how large the velocity difference between the layers is and if it is large enough to result in mixing. In Section 2.1.2, a short overview of mixing processes in stratified shear flow is given. The Richardson number gives an indication of shear instabilities in the flow. In this section, the return current in a stratified canal is discussed. This is followed by a discussion on how large the velocity difference should be to completely mix the flow over the vertical. Finally, the most important parameters in defining the return current in stratified canals are discussed.

3.3.1. Return flow formulas

There are two main approaches for describing the primary wave system next to the ship. The method of Schijf is based on the preservation of energy, and the method of Bouwmeester is based on the preservation of momentum. The difficulty in using these methods is that they approach the flow pattern as to be one-dimensional, and that they do not describe the gradient of the velocities underneath the ship or next to the ship. It might be possible to estimate the return flow velocities in a two-layer system by adjusting these equations.

In their research into sailing over a fluid mud layer, Vantorre and Coen (1988) and Vantorre (1991) derived formulas for a return current in a two layer system following a similar method as Schijf did for an unstratified canal. Unfortunately, the copy of these articles that was available to the author was hard to read and an attempt to derive the formulas from the continuity equation and the preservation of energy was unsuccessful. The method would have some drawbacks as well, as this would result in an one-dimensional formulation, while the flow around a vessel is three-dimensional. Using the data from the graphs provided by Vantorre and Coen (1988) and Vantorre (1991) is not possible as they only include much larger density differences than typically found in a canal.

It is therefore not known what a possible velocity difference due to the return current would be. The formulas do give some insight in which parameters might play a role in how fast the return current is and how it is spread over the layers. These are discussed in a later section.

3.3.2. Mixing by velocity shear

Velocity shear between the layers will occur if the return current of the vessel is indeed unevenly spread over the layers. Mixing is an energy exchange. To fully mix a stratified flow by velocity shear, the decrease in kinetic energy should equal the potential energy. Cushman-Roisin (1994) used this to derive a criterion for complete vertical mixing by velocity shear in a two-layer flow:

$$\frac{\epsilon g H}{\Delta U^2} < 1 \tag{3.4}$$

with $\epsilon = \frac{\rho_2 - \rho_1}{\rho_0}$ the relative density difference with $\rho_{1,2}$ the density in the top or bottom layer in kg/m^3 and ρ_0 the reference density in kg/m^3, H the total water depth in m, and ΔU the difference in velocity between the top and bottom layer in m/s. This formula is derived using the shift in potential energy from the initial state to a fully mixed state and conservation of linear momentum for the kinetic energy loss. This criterion shows that for a less deep canal, a smaller velocity difference is needed to fully mix the same density difference. In a less deep canal of the same width, the return current for the same ship will be higher. This would mean that a potential velocity difference due to the return current would more easily mix the AKP than the NZK for example. If the above criterion is not met, the mixing will only occur locally. Pietrzak (2012) gives a resulting thickness of the mixing layer of:

$$\delta = 0.3 \frac{\Delta U^2}{\epsilon g} \tag{3.5}$$

with δ the thickness of the mixing layer and ϵ the relative density difference.

3.3.3. Main parameters

The formulas as given by Vantorre and Coen (1988) and Vantorre (1991) give insight in a few dimensionless parameters that are important for the return current. The effect of these and some additional parameters on mixing by shear is analysed below. These hypotheses will be tested in a numerical model in the next chapter.

- **Canal blockage**
  Vantorre and Coen (1988) and Vantorre (1991) make a distinction between canal blockage in the top layer ($m_1 = \frac{w_s d_1}{w_c h_1}$) and canal blockage in the bottom layer ($m_2 = \frac{w_s d_2}{w_c h_2}$). w_s is the width of the vessel, d the draught in the top or bottom layer, w_c is the width of the canal, and h is the height of the layer (see also Figure 3.6). The draught to top layer height ratio (d/h_1) and the layer distribution (h_1/h) are likely to have an influence on the distribution of the return current.

  A higher canal blockage in the top layer leads to higher return flow velocities as a larger volume of water is moved. For high density differences, this higher return flow velocity is relatively more

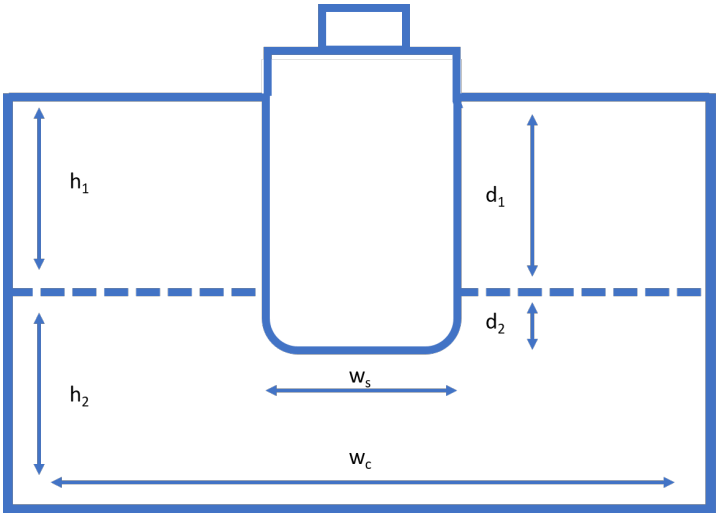

Figure 3.6: Cross section of a canal with a ship and parameters describing canal blockage.

visible in the top layer resulting in more shear between the layers. This effect reduces when the underkeel clearance of the vessel to the interface becomes too small.

A higher canal blockage in the bottom layer leads to even higher return flow velocities. For m_2 is not zero, both layers are directly disturbed by the vessel. The higher return flow velocity does not result in more shear as both layers are moved. However, the disturbance of the interface leads to mixing.

The draught to top layer height ratio could give information on how much influence a ship has on a layer. There are two possible cases. If a ship is sailing above the interface,d/h_1 gives information on the amount of shear and the influence on the bottom layer. If the ratio is 1, the ship is sailing on the interface. It is likely that the interface will deform under the vessel. For values close to 1, the top layer will be partly forced under the vessel. For larger values, the top layer moves completely next to the vessel. When the top layer is less deep for the same draught, the influence on the bottom layer is higher. This could result in less shear between the layers. This is the ratio h_1/h.

- **Internal Froude number**
  Vantorre and Coen (1988) and Vantorre (1991) used a separate Froude number for the top and for the bottom layer. The situations that they studied have dense fluid mud bottom layer with a limited height. As this is not the case for a typical canal with salt intrusion, the internal Froude number based on the ratio of the sailing speed to the interfacial wave velocity is used in this report (see Equation 2.6).

  A higher sailing speed gives a higher internal Froude number. When the sailing speed is higher, the same volume of water is moved at a higher speed, which results in a higher return flow velocity. This can give more shear if the return flow is concentrated in the top layer. Furthermore, the Froude number might give indication of the state of the flow and possible hydraulic jumps.

  The internal wave speed is dependent on the density profile, and therefore the density profile will also change the internal Froude number. A higher relative density difference could give more shear in between the layers. Turbulence will be suppressed by the higher stratification. For a lower density difference, the flow pattern will approach the flow pattern of a homogeneous density profile more.

- **Eccentricity of vessel in canal, shape of vessel, effect canal banks**
  The eccentricity of the vessel in a canal, the vessel shape, and the canal geometry will influence the return flow as well as they do for a unstratified flow (Verheij et al., 2008). It is expected that these parameters will have a smaller impact on the overall return flow compared to the above mentioned parameters.

3.4. Processes: Internal waves

Internal waves behind the vessel can lead to mixing due to shear instabilities or wave breaking on a slope. In this section, the internal Froude number, wave angle, wave dimensions, and wave energy for vessels sailing in a two-layer stratified canal are discussed.

3.4.1. Wave pattern

Several different definitions of the internal Froude number are used. Two of them are discussed here. Both can be used to see whether the conditions will create a sub- or supercritical internal wave pattern. The wave pattern gives information on how the internal waves reach the canal banks, which might be important for breaking processes.

The first definition of the internal Froude number is based on sailing speed and the long wave speed. For a Froude number higher than one, the flow is supercritical (Baines, 1984). The interfacial long wave speed for a two-layer flow can be calculated using the density difference and layer height as shown below (Sutherland, 2010). It is similar to long wave speed of surface waves ($c_0 = \sqrt{(gH)}$, only the gravity has been replaced by the reduced gravity and instead of the the total water depth, an equivalent depth taking into account the layer distribution is used.

$$c_0 = \sqrt{g \frac{\rho_2 - \rho_1}{\rho_2} \frac{h_1 h_2}{H}} \tag{3.6}$$

$$Fr \equiv \frac{U}{c_0} \tag{3.7}$$

For an inland vessel, the internal Froude number is almost always higher than one. The vessels are sailing much faster than the internal wave travels, which means that the wave pattern will be similar to the surface waves of a speed boat travelling in shallow water.

The second definition uses a critical Froude number that is compared to the total depth Froude number. Yeung and Nguyen (1999) give a derivation of the waves generated by a point source moving over two-layers of finite depth. They formulated a critical Froude number.

$$Fr_c^2 = \frac{1}{2} + (-1)^{n+1} \sqrt{\frac{1}{4} - \frac{(1-\gamma) h_1 h_2}{h^2}} \tag{3.8}$$

with $\gamma = \frac{\rho_1}{\rho_2}$, and h_1, h_2, h, the top, bottom, and total layer thickness respectively, and n the wave mode. Surface and internal waves consist of contributions of both the surface and internal wave mode, however for small density differences, only the internal wave mode ($n = 2$) can be considered. Sano and Kunitake (2017) present a similar critical Froude number that includes the length of the vessel as well. It multiplies the previous critical Froude number with the square of the ratio of the water depth to the vessel length.

$$Fr_{c,L} = Fr_c \sqrt{\frac{h}{L}} \tag{3.9}$$

This critical Froude number is compared to the total depth Froude number $Fr^2 = \frac{U^2}{gh}$ (or $Fr = \frac{U}{\sqrt{gh}}$) to find the pattern of the waves using $\phi = \arcsin \frac{Fr_c}{Fr}$ (Yeung and Nguyen, 1999). This gives for internal waves in a typical inland waterway, a supercritical wave pattern with only diverging waves as the total depth Froude number is always larger than the critical Froude number. Sano and Kunitake (2017) does not mention a formula for the wave angle, it is therefore unclear whether this critical Froude number can be used to calculate the angle the waves make. Both methods give a supercritical pattern for the interfacial waves when using a typical density gradient and sailing velocity. The second method has as advantage that also the angle of the waves can be calculated.

Baines (1987) discusses three definitions for the Froude number for linearly stratified flows describing internal wave drag using the obstacle length, a ratio of fluid speed to internal wave speed using the

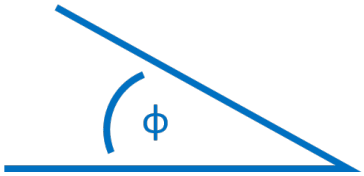

Figure 3.7: Definition of the wave angle ϕ. It is the wave angle between the sailing direction and the crests of the waves.

fluid depth, and one describing wave steepening and blocking using the height of the obstacle. In this case, the ratio of fluid speed to internal wave speed is needed. This Froude number is defined as:

$$Fr = \frac{U}{NH} \tag{3.10}$$

with U the speed of the obstacle, N the buoyancy frequency, and H the depth of the flow (Baines, 1987). It is unclear how this relates to the wave angle. The formulas of Sharman and Wurtele (1983) could be used, but are difficult to apply to a quick estimation.

3.4.2. Wave dimensions

In the previous section is shown that in inland waterways only supercritical wave patterns are to be expected. In this section, the characteristics of these diverging waves are explored for both a linearly stratified fluid as a two-layer stratified flow. Yeung and Nguyen (1999) give the following non-dimensional parameters for the wave height: location of source to water depth, h1/h, gamma, Fr. The reader is referred to Yeung and Nguyen (1999) for the derivation of the corresponding formulas. A short summary of the effects of these parameters is given below. Corresponding the analysis above, this will focus on divergent internal waves.

The first non-dimensional parameter given by Yeung and Nguyen (1999) is ζ/h. As Yeung and Nguyen (1999) derived the formulas for a point source, ζ is the depth of the point source in the upper layer fluid. Yeung and Nguyen (1999) derived the formulas for a point source and not a vessel. Additionally, the formulas are not derived for a disturbance in the bottom layer. The internal wave height decreases when the point source moves closer to the surface and farther away from the interface, meaning a larger ζ/h.

As shown in Equation 3.8, the critical Froude number is dependent on the density distribution. Yeung and Nguyen (1999) studied the influence of the layer distribution, density difference and vessel speed separately. Yeung and Nguyen (1999) showed that an increase in h_1/h means a decrease in wave amplitude, so for a larger top layer, smaller internal waves are created. Equation 2.4 shows that the layer distribution also influences the stability of the internal waves.

The density difference ($\gamma = \rho_1/\rho_2$) has a complex effect on the wave height as it also influences the critical Froude number. The internal wave amplitude increases largely for small density differences ($\gamma = 0.97$) compared to larger density differences (Yeung and Nguyen, 1999). In an inland waterway, only smaller density differences than 0.97 are present. As explained above, the speed of the vessel influences the wave pattern, which results in either a subcritical or supercritical wave pattern. Yeung and Nguyen (1999) show that for larger Fr/Fr_c (faster sailing speeds) the diverging wave amplitude decreases.

Chang et al. (2006) found a larger wave length for a larger Froude number. Medjdoub et al. (2020) confirmed that the wave length and amplitude of internal ship waves are set by the sailing speed, density profile and ship's length. Medjdoub et al. (2020) found that the amplitudes are largest when the wave length of the interfacial waves (dependent on the ship's sailing speed) is equal to the wave length of 'trapped' lee waves (dependent on the buoyancy frequency). This resonance creates the largest waves, and the amplitude of the waves is set by a combination of lee waves and propagating interfacial wave modes (Medjdoub et al., 2020). However, this study did not take into account the three-dimensionality of flow around a vessel.

Section 2.1.3 gave a short introduction in the reflection and breaking of internal waves on a slope. A combination of wave steepness to slope steepness determines the amount of breaking and reflection. More study is required to get a good estimation of the contribution to breaking, especially since many studies focus on internal solitary waves which probably behave different from internal ship waves. Both

the NZK as the AKP have a canal bank slope of about one on three. This is a relatively steep slope. It is the maximum slope studied by Aghsaee et al. (2010) for example. Aghsaee et al. (2010) found surging, plunging and collapsing breakers for steep slopes, however, this was for internal solitary waves and it unknown how the steepness of ship-induced internal waves relates to that of internal solitary waves.

3.4.3. Wave energy

The generation of internal waves requires energy resulting in an increase in resistance. An extreme case of this is the dead-water phenomenon, where all the energy produced by a vessel is used to generate waves. This was first researched by Ekman in 1904. More than hundred years later this phenomenon is still studied, for example by Esmaeilpour (2017), Esmaeilpour et al. (2018), Fourdrinoy et al. (2020) and Medjdoub et al. (2020). For this research, the dead-water phenomenon will not play a role, however the wave energy is an important component to study as the wave energy will eventually either contribute to dissipation or mixing. The amount of wave energy generated is the product of the drag and the speed of the ship (Kundu, 2013)

The total wave energy consists of potential energy and kinetic energy. This wave energy can be either dissipated or contribute to an change in background potential energy by diffusion (Arthur and Fringer, 2014). The amount of potential energy available to be converted to kinetic energy (and consequently to mixing) is called the available potential energy. The amount of kinetic energy is roughly equal to the amount of available potential energy Lamb (2014). For a free wave, the potential energy is equal to the kinetic energy, while for a forced wave this equipartition is not valid.

The available potential energy in J/m^3 is based on the difference between the disturbed and background density profile and can be expressed as:

$$APE = g \int \rho' dV \tag{3.11}$$

with ρ' the density relative to a background or reference density. Kang and Fringer (2010) discusses different formulations of the APE. The kinetic energy in J/m^3 is expressed as:

$$KE = \frac{1}{2}\rho_0 \int u_i^2 dV \tag{3.12}$$

with ρ_0 a reference density and u_i the velocity vectors in all directions (Moum et al., 2007). The total wave energy density is then given by $E = KE + APE$.

3.4.4. Main parameters

Several parameters have been shown to influence the wave dimensions and pattern. The internal Froude number is an important parameter herein. Below, a short summary of the main parameters for internal waves are given, which will be tested using numerical runs in the next chapters.

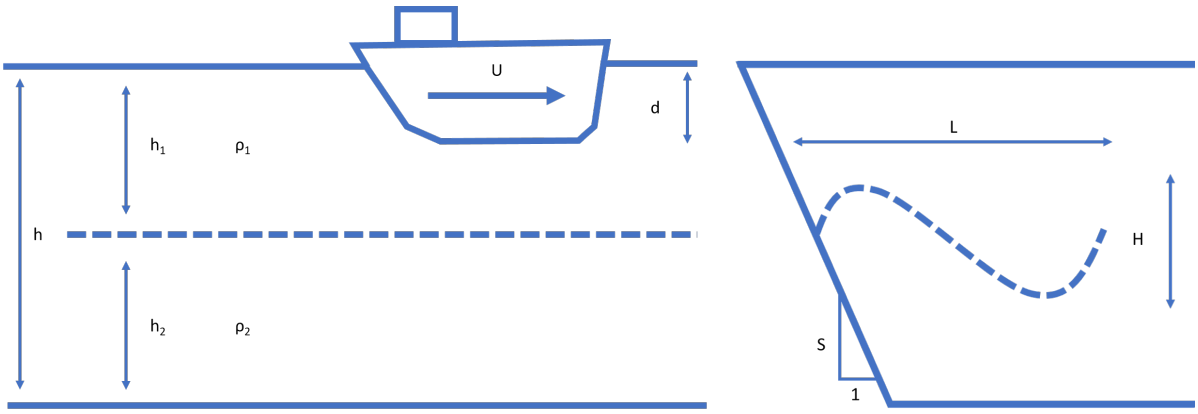

Figure 3.8: Left: Ship sailing in a canal and relevant parameters. Right: Cross section of a canal with parameters describing the slope of the canal bank and the internal wave.

- **(Critical) internal Froude number**
  The ratio of the internal Froude number to the critical internal Froude number determines the angle of the V-shape of the waves. This ratio takes into account the layer distribution, density difference, length of the ship and the sailing speed. This angle determines how the waves reach the banks of the canal. The internal Froude number is also expected to have an influence on the wave length and height (see Yeung and Nguyen (1999) and Chang et al. (2006)).

- **Layer distribution:** h_1/h
  The layer distribution influences the critical Froude number. A larger top layer gives smaller internal waves (Yeung and Nguyen, 1999). Furthermore, the layer distribution influences the stability of the internal waves.

- **Density difference:** ρ_1/ρ_2
  The density difference influences the critical Froude number. A small density density difference results in smaller wave heights for supercritical conditions (Yeung and Nguyen, 1999).

- **Relative depth:** d/h
  A larger relative depth of the source results in an increased wave height (Yeung and Nguyen, 1999). When the source moves closer to the interface, the interface disturbance is larger.

- **Wave steepness to slope ratio**
  The wave steepness to slope ratio can be expressed in different ways as described in Section 2.1.3. It influences wave breaking and reflection. A typical canal bank slope is relatively steep compared to slopes found in previous studies. From Figure 6 of Aghsaee et al. (2010), from a small to large wave steepness would mean surging, collapsing to plunging waves.

3.5. Processes: Propeller mixing

Previous studies suggest that the effect of the propeller is small and local (see Section 2.2.3). At the same time, the propeller power is often used as a first estimation of the effect of ships in a canal. In this section, an estimation of the propeller velocities is made. A previous calculation by Karelse and Van Gils (1991) is redone for the NZK, ARK, and AKP to estimate the energy dissipation by ships compared to wind and bottom roughness. Finally, some important parameters influencing the propeller jet are given.

3.5.1. Propeller velocities

In 1950 Albertson et al. (PIANC (2015)) presented a series of equations on the diffusion of submerged jets based on the actuator disk or axial momentum theory. In these equations it is assumed that the jet flow can be schematised as a free jet discharging from an orifice into an infinite fluid. In this section, a quick estimation of propeller velocities for vessels sailing in a canal is made.

The canals are designed for VIb vessels. The analysis above showed that Va vessels are predominantly present at the AKP. Ten Hove (2008) gives an overview of properties of Dutch inland waterway vessels based on interviews with owners of the vessels. The installed main power system is on average 740 KW with a reported minimum of 75 kW and a reported maximum of 4511 kW. A Va vessel has an average main power system of 1067 and 1266 kW respectively. Ten Hove (2010) gives for VIa vessels an average main power system of 1573 to 2404 kW. The main power sytem of push boats is larger. Ten Hove (2008) gives an average value of 4080 kW for the largest type of push boat (Duw4). Acccording to Ten Hove (2008) most commercial inland vessels have a ducted propeller.

The method described by PIANC (2015) is used to estimate propeller velocities. First, the formula of Blaauw and van de Kaa (1978) is used to estimate the efflux velocity, V_0. This is an empirical relation that is easy to use.

$$V_0 = C_3 \left(\frac{f_p P_D}{\rho_w D_p^2} \right)^{0.33} \tag{3.13}$$

with C_3, a coefficient for the type of propeller, f_p, the percentage of installed engine power, P_D, the maximum installed engine power in W, ρ_w, the water density, and D_p, the propeller diameter. f_p is generally 5 to 15 % (PIANC, 2015), D_p is 2 m (Verheij et al., 2008). For a ducted propeller, C_3 = 1.17 (Verheij et al., 2008).

Main power system (kW)	$V_{0,min}$ (m/s)	$V_{0,max}$ (m/s)
1000	2.69	3.87
2000	3.38	4.86
4000	4.25	6.11

Table 3.4: Estimates of the efflux velocity for several main power systems using C_3 = 1.17, f_p is 5% ($V_{0,min}$) to 15 % ($V_{0,max}$), and D_p is 2 m.

Using the efflux velocity, the German or Dutch approach can be followed to approximate the development of the flow field. The Dutch approach is given below following PIANC (2015).

First, the development of the velocity along the axis can be calculated using the formula below.

$$V_{axis} = (2.0 \text{ to } 2.8) V_0 (D_p / x) \tag{3.14}$$

with x the distance from the axis behind the propeller. The distribution of the velocity over the width and depth can be calculated using the formula below.

$$V_{x,r} = V_{axis} \exp(-15.4 r^2 / x^2) \tag{3.15}$$

with r the distance from the axis perpendicular to the outflow velocity. This shows that the velocity behind the propeller decreases linearly, while the velocity perpendicularly decreases exponentially. Figure 3.9 gives an example of how the flow field of an propeller jet looks using the above equations. The velocity distribution of a jet will be disturbed by the channel bottom, water surface and the movement of the flow. Furthermore, the density distribution will change the development of the jet.

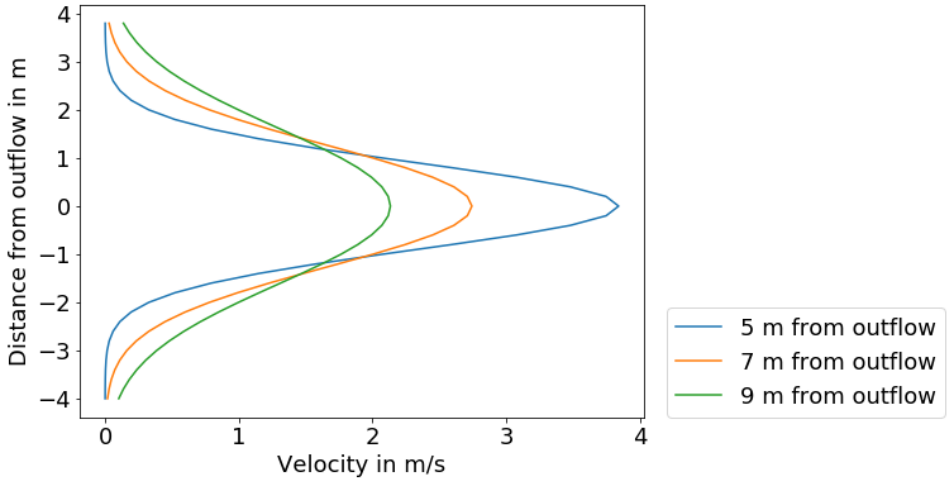

Figure 3.9: Velocities in the propeller jet at 5, 7 and 9 m from the propeller for a outflow velocity of 4 m/s.

3.5.2. Main parameters

More research is needed to get a full picture of how mixing by the propeller is influenced. The propeller jet can entrain surrounding fluid and contribute to mixing (Voropayev et al., 2012)) or generate internal waves (Brucker and Sarkar (2010), Esmaeilpour et al. (2016)). Some parameters that are likely to play a role are given below. This list is incomplete as more knowledge on mixing by propeller jets in stratified canals is needed.

- **Jet velocities**
  For sailing in a straight canal, little power is need. The propeller power increases when ship accelerates or navigates. Other characteristics of the propeller also play a role in the velocities behind the propeller, such as the propeller diameter and whether the propeller is ducted or not.

- **Distance of the propeller to the interface layer**
  Esmaeilpour et al. (2016) showed that the distance of the propeller to the interface layer is an important parameter in the response of the interface.

- **Density gradient close to the propeller**
  The density gradient close to the propeller will play an important role in the amount of entrainment. Mixing a stratified flow requires energy. If the density gradient is larger, more energy is needed to mix the flow.

3.6. Discussion of possible mixing processes

At the start of this chapter, two typical canals in the Netherlands were introduced. The salt intrusion in the Noordzeekanaal is characterised by a salt wedge, while the Antwerps Kanaalpand is over most of the year well-mixed. Data from a canal blockage seems to show less mixing in the AKP during the blockage, although other factors such as wind might have played a role as well. The variability over the week seems to support the idea that less ship traffic during the weekend results in more stratification over the weekend, as was also observed for the Amsterdam-Rijnkanaal by Hydrologic (2020).

With respect to the studied mixing mechanisms, the following conclusions can be drawn.

- **Return current**
  The return current is likely to be important in mixing, since it causes locally large velocities. The main parameters of influence are the canal blockage and the internal Froude number.

- **Internal waves**
  The contribution of the internal wave system to mixing is unknown. Internal waves could contribute to mixing in by shear instabilities in the wave field and by wave breaking. Again, the internal Froude number is of importance. This means that the sailing speed, layer distribution, density difference, and relative depth of the vessel are important in determining the wave pattern and dimensions. Furthermore, the slope of the canal bank is of importance as internal waves could break on the side slopes.

- **Propeller jet**
  The propeller jet is also likely to be important in mixing, since it causes locally large velocities. The propeller power and dimensions, location of the propeller to the interface and the local density gradient are parameters that will influence this process.

No parameter studies on these processes in stratified canals have been found. The influence of stratification on the return current and the amount of mixing generated by the return current is still unknown. Although internal waves and the propeller jet behind a vessel have been studied in much more detail, their contribution to mixing in a canal is still unclear. These processes and their influence on the mixing of salinity in a canal are therefore further studied in a numerical model which is described in Chapter 4. The results of this study are discussed in Chapter 5.

4

Numerical modelling approach

A numerical is used to see how much ships contribute to mixing in an inland waterway, and to which processes this can be attributed. The numerical analysis follows from the work done in the analytical analysis in the previous chapter. Several variations of canal dimensions, ship characteristics, and density profile are done to see how different parameters influence different processes and in which cases mixing is generated. The cases are selected based on the insights done in the analytical part, and the canal characteristics found. In this chapter, the numerical modelling approach, numerical model, and model set-up are described. Also, a short description of how the results will be analysed is given.

4.1. Numerical model

First, the aim and planned approach is discussed. This approach poses several requirements on the model. Following these requirements, a numerical model is chosen, and a description of the model is given. This section ends with an overview of available validation for the chosen model.

4.1.1. Aim and approach

The aim of the numerical runs is to find out to what extent mixing is generated by a vessel, and which processes are responsible for the mixing. The influence of the identified parameters on these processes is investigated.

First, a reference run with a ship in canal with stratification is done. The characteristics of this run are based on typical values found in the previous chapter. This is followed by several parameter variations. The parameter study focuses on the return current, interface deformations and internal waves, and the breaking process of these waves. Missing from this list compared to the previous chapter is the propeller jet. The jet has been excluded to simplify the model. Adding a propeller to the model would make the model much more complicated.

The return current and internal waves are studies in three parts. The influence of the canal blockage, internal Froude number, and canal bank slope on the amount of mixing and the mixing processes is investigated. These parameters are influenced by several other parameters. The canal blockage is for example influenced by both ship dimensions as canal dimensions. As it is not yet clear whether the canal blockage or ship or canal dimensions is dominant in determining the flow response, both the ship and canal dimensions will be varied. The same goes for the internal Froude number. A more detailed run plan follows in the next chapter.

4.1.2. Requirements

The approach described above poses some requirements to the numerical model.

The flow field around a vessel is 3D. A vessel is relatively small compared to the canal geometry. It is therefore important to model the problem in 3D. Furthermore, non-hydrostatic effects will be important. The hydrostatic pressure assumption neglects vertical accelerations. The pressure gradients in stratified flow give vertical accelerations and as the goal is to study vertical mixing, it is important to use a non-hydrostatic model. The model should be capable of representing internal waves, internal

wave breaking and shear instabilities in stratified flow well. It should also be capable of representing long and short waves to accurately model the primary and secondary internal wave.

Moreover, a moving vessel should be able to be modelled. It is not easy to add a moving vessel to a numerical model. It quickly requires a lot of computation power and produces numerical artefacts. In Appendix D, several methods to add a moving vessel to a model are discussed. A method that introduces little numerical diffusion should be chosen. As multiple canal geometries and ship draughts will be used, it is important that the geometry is easily adaptable and the mesh easily generated.

FinLab meets the requirements for the numerical model best, as it allows to model a moving vessel accurately. It is a fully non-hydrostatic finite element model based on the incompressible Navier-Stokes equations. The model is developed at Svasek and Delft University of Technology by Robert Jan Labeur.

4.1.3. Model description

FinLab solves the incompressible Navier-Stokes equations. These consist of the momentum equation (see Equation 4.1) and the transport equation based on the incompressibility of water (see Equation 4.2). The transport of salinity is modelled by Equation 4.3. In this section, these equations are discussed as well as the required boundary conditions.

FinLab works with an unstructured mesh of tetrahedra. The vessel can be added by deforming the mesh with a ship hull. This mesh moves with the speed of the ship ($\mathbf{u}_{grid}$ in m/s). The method used in FinLab is such that the velocities calculated in the model are the velocities as would be observed from a fixed point. This is the most accurate way to model a moving vessel, however, it requires an uniform canal.

$$\frac{\partial(\rho\mathbf{u})}{\partial t} + \nabla\cdot(\rho(\mathbf{u}-\mathbf{u}_{grid})\otimes\mathbf{u}) + \nabla p - \nabla\cdot(2\mu\nabla^s\mathbf{u}) = \mathbf{F} \tag{4.1}$$

with velocity vector **u** in m/s, p the fluid pressure, (turbulent) kinematic viscosity μ in m^2/s, the symmetric gradient operator $\nabla^s = \frac{1}{2}\nabla(\cdot) + \frac{1}{2}\nabla(\cdot)^T$, and the sum of the external forces **F** in N/m^3 which includes the buoyancy term ($-\rho g e_z$)

$$\nabla\cdot\mathbf{u} = 0 \tag{4.2}$$

$$\frac{\partial\tilde{\rho}}{\partial t} + (\mathbf{u}-\mathbf{u}_{grid})\cdot\nabla\tilde{\rho} - \nabla\cdot(\kappa\nabla\tilde{\rho}) = f \tag{4.3}$$

with relative density difference $\tilde{\rho} = \frac{(\rho-\rho_0)}{\rho_0}$, κ the turbulence diffusivity, and f the source term.

The model needs a divergence-free initial velocity field and several boundary conditions. A choice can be made between a wall, surface, level, velocity, Riemann, wave, and symmetry boundary. At an open boundary, **u**-$\mathbf{u}_{grid}$ is used as boundary. The shear at the ship hull is calculated using the combined velocities in the model with the velocity of the mesh. The shear at the walls is calculated using solely the velocities in the mesh. This method of a moving mesh reduces numerical artefacts. The wall shear stress for a non-moving wall is:

$$\tau_w = c_f|\mathbf{u}|\mathbf{u} \tag{4.4}$$

with c_f a dimensionless friction factor. For a moving wall **u** is replaced in the above equation with the relative velocity to the moving wall, **u** - $\mathbf{u}_{grid}$. In this case, the ship hull is a moving wall. The normal velocity at the closed boundaries is zero. For the ship hull (moving, closed boundary), the normal velocity of the combined **u** - $\mathbf{u}_{grid}$ is zero.

The reader is referred to Labeur (2009) for a more elaborate description of the model.

4.1.4. Model validation

Some validation for FinLab is available. Pietrzak and Labeur (2004) validated the response of FinLab to reproduce field data of the Rotterdam Waterway and internal wave response predicted by analytical theory. Labeur and Pietrzak (2005) showed that FINEL3D (the predecessor of FinLab) accurately models trapped internal waves and internal lee waves. Boon (2011) has done several validation tests for modelling internal waves using FinLab. The energy loss of breaking of internal solitary waves on a sloping bottom has been validated using laboratory results of Boegman et al. (2005). The wave

breaking is found to be well simulated. Boon (2011) also validated the behaviour of FinLab for lee waves. This was in line with what found using analytical calculations.

Although there are similarities expected between topography and ships in a stratified canal, more validation is be needed for the way the model will now be used. No validation has been done yet on the moving mesh method.

4.2. General model set-up

In this section, the general model set-up for this study is discussed. First, the mesh generation is discussed. This is followed by the numerical set-up in which a more detailed description of the initial and boundary conditions is given as well as the most important numerical parameters used.

4.2.1. Mesh generation

As discussed before, FinLab uses a mesh of tetrahedra. Several steps are needed to make a mesh of a canal with a ship hull.

First, the geometry is modelled in Rhinoceros®, a 3D CAD software programme from Robert McNeel & Associates[1]. To facilitate adjustments to the geometry, Grasshopper®(also from Robert McNeel & Associates) is used. A good representation of a ship hull is needed to minimise effects of sharp corners on the result. To make such a faired ship hull, the rapid ship hull modelling tool developed by RhinoCentre[2] is used as a basis. A barge model is adjusted to match dimensions typical for inland waterways. As standard dimensions, the barge is made 110 m long, 11.45 m wide with a draught of 3.5 m and a sailing speed of 3 m/s. A simple barge shape is used in order to have a 'real' hull shape.

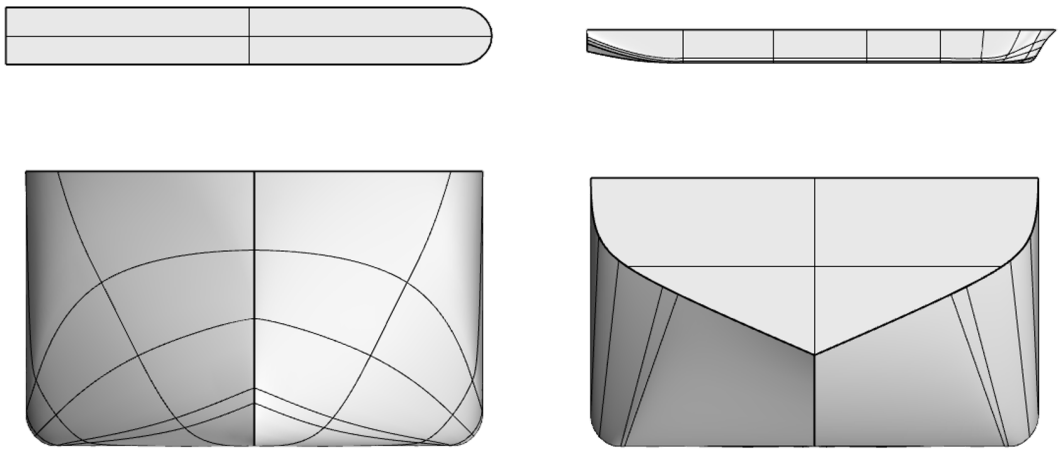

Figure 4.1: Top, side, front and back view of the barge used.

This geometry is subsequently loaded into Gmsh (version 4.6.0) (Geuzaine and Remacle, 2009) to make a 3D mesh consisting of tetraeders. Gmsh is chosen as it is easy to use and works well together with the Rino-output. The aspect ratio of a typical canal is very high, as it is a very flat and long. To simulate the effects on the interface well, enough elements over the vertical are needed. A range of 15 to 30 elements over a depth of 15 meters will produce good results. To limit the number of elements needed and because of the high aspect ratio of a typical canal, the tetraeders are deformed. This is done by scaling the model before meshing. In the last step, the model is re-scaled to its original dimensions.

Several limitations limit the number of elements in the mesh. Too much elements in the vertical gives strongly deformed elements, which leads computational errors. Too much elements in total lead to long computation times. Iteration between element size and scaling factors is therefore needed to

[1]Version 6. URL: https://www.rhino3d.com/[last accessed on 14-4-2021]

[2]RhinoCentre, URL: http://rhinocentre.blogspot.com/2009/12/grasshopper-parametric-ship-hull.html [last accessed on 8-4-2021]

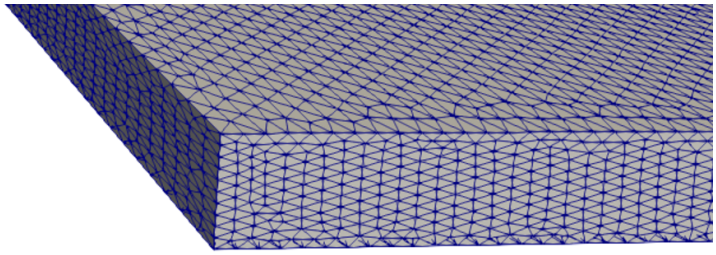

Figure 4.2: Example of a part of the mesh generated.

find a well-working mesh with as much elements as possible. The first tests are done in a rectangular 800 m long canal of 220 m or 50 m wide and 15 m deep. These meshes have 300.000 elements. The runs with a slope are done in a canal of 2000 m long of on average 220 m wide and 15 m deep. These meshes have about 500.000 elements. All meshes have about 15 elements over the depth. The high aspect ratio and scaling used result in a relatively large number of poorly shaped tetrahedra which consequently makes convergence of the solution more difficult.

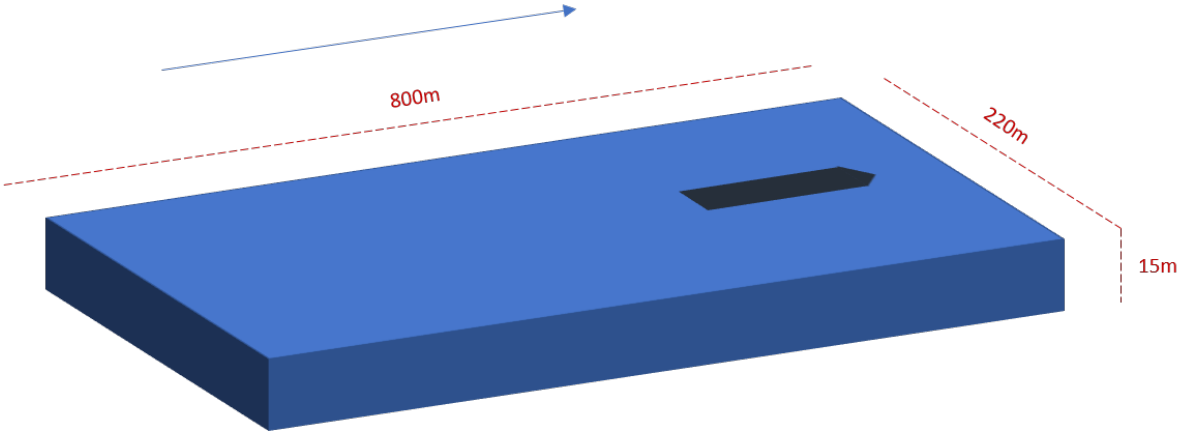

Figure 4.3: Schematic drawing of the geometry used for most runs. A rectangular canal is deformed with the hull of a vessel. This geometry is subsequently transformed into a mesh. During the calculations the mesh moves with speed of the vessel.

4.2.2. Numerical setup

Initial and boundary conditions

The density distribution is applied as initial condition in the model, as well as on the inflow boundary. Most runs are done with a tanh-profile. The tanh-profile is chosen such that numerical diffusion is low. This means that mixing layer is relatively large. A few runs are done with a linear density profile.

The damping time damps the velocity of the vessel during the first steps. The speed of the vessel increases exponentially until the given velocity is reached. This is done to not disturb the water abruptly.

The following boundary conditions have been applied:

- **Wall**
  A wall boundary is applied at the bed and banks of the canal and at the ship hull. The shear at the non-moving walls is calculated using the velocities in the mesh, while the shear at the ship hull uses the velocity relative to the moving wall (see Section 4.1.3).
- **Level**
  At the outflow boundary a water level boundary is set. A combination of a water level at the outflow boundary and a velocity boundary at the inflow works usually best for stratified flows.
- **Velocity**
  At the inflow boundary a velocity boundary is set. In this case, no discharge is applied. At this

boundary the salinity distribution is applied as well.

- **Symmetry**
  The water surface is modelled with a symmetry boundary without friction. The water surface is modelled with a rigid-lid. This means there is no propagation of surface waves which results in a quicker steady state solution. It is assumed that the lack of surface waves does not influence the internal wave generation too much.

Numerical parameters

The most important numerical parameters are discussed here. Appendix E gives an overview of all the parameters that are used.

The fractional step method is as time integration method (see Labeur (2009) for more information). Test runs show that the solution only converges on the mesh used with this method. It is a second-order accurate, strongly stable method. To reach convergence of the solution, the Mach number has been set to a relatively high value. The Mach number is the ratio of the flow velocity to the local speed of sound. It is assumed that this does not influence the model results too much.

LES (Large Eddy Simulation) is used as turbulence model. In this model, the anisotropic large scale eddies are separated from the isotropic small scale motion. The large eddies are solved explicitly. For the smaller scales, a subgrid model is needed for which the Smagorinsky model is used. The use of this model is closely related to the grid size, which is relatively rough in this case as described above.

A linear polynomial order advection scheme and an adaptive polynomial transport scheme is used as this gave the best results in the test runs. In a canal without disturbances the density distribution at the inflow and outflow boundary was most comparable for the adaptive polynomial order transport scheme. However, the density distribution does change slightly over the length of the canal as will be shown in the next chapter.

4.3. Analysis of the results

The analysis of the results consists of three parts. The results are analysed with the questions from Section 5.1.1 in mind. The results are analysed using Paraview (version 5.8.0), a data analysis and visualisation application developed by Kitware (Ahrens et al., 2005).

The result are also interpolated to a regular grid of 1 by 1 by 0.5 m and further analysed in Python. This is done using the 'griddata' option of the Scipy interpolate package with the linear method. This method deforms the results at the location of the ship. The results of the interpolation at that location are therefore not reliable.

For most of the runs, a corresponding run without a vessel is done. This run can be used to remove most of the numerical effects and to see the added contribution of the vessel.

The plan of approach for the analysis of the results is described below.

- **Flow pattern and shear instabilities**
  Velocity contours give insight in the velocity differences. Special attention is payed to velocity differences between the layers. The gradient Richardson number is calculated everywhere in the model domain and might indicate the location of instabilities.

- **Interface deformations and internal waves**
  The interface deformations around the vessel are measured, as well as the internal wave characteristics behind the vessel. The results are given in a dimensionless salinity from 0 to 1, which can be translated to density by using the relative density difference. The interface can be plotted by plotting a contour where the salinity is 0.5. Using this contour, waves on the interface can be plotted in various ways to measure wave height, length, and the angle of the waves.

- **Mixing**
  Mixing will result in a change in density distribution. Density profiles and the PEA (see Equation 2.2) are used to measure the the effect on the density distribution and the amount of mixing.

$$PEA = \frac{1}{H}\int_{-h}^{\eta}(\bar{\rho}-\rho)gz\,\mathrm{d}z \tag{4.5}$$

The width-averaged PEA can be used to have a quick overview of the changes over the length of the canal. As the PEA is different for runs with a different density distribution, the relative difference in PEA is used to compare the runs. This is calculated using the width-averaged PEA.

$$\text{Relative difference PEA} = \frac{PEA_{\text{vessel,avg}} - PEA_{\textit{without vessel,avg}}}{PEA_{\text{without vessel,avg}}} * 100\% \tag{4.6}$$

with $\rho_{vessel,avg}$ the width-averaged density of the run with a vessel and $\rho_{withoutvessel,avg}$ the width-averaged density of the corresponding run without a vessel. The relative changes in the density profile are given by:

$$\Delta\rho = \frac{\rho_{\text{vessel,avg}} - \rho_{\text{without vessel,avg}}}{\rho_0} * 100\% \tag{4.7}$$

with reference density ρ_0 = 1000 kg/m^3. These width-averaged profiles are compared at the outflow boundary.

5

Results of the numerical model

This chapter discusses the results of the numerical runs. First, an overview of the runs done is given. Next, the general flow field is described. This is followed by a discussion of the effect of the different parameters. An overview of the run numbers and parameters is given at each section. This chapter ends with a discussion of the observed effects.

5.1. Model setup and runs

The model setup has been discussed in general in Chapter 4. In this section, the focus of the model runs is discussed. This is followed by a detailed overview of the runs done.

5.1.1. Focus of the run analysis

The main question is how much mixing is generated by ship traffic and which process is most important in generating this mixing. With help of the numerical model, the return current and the internal waves behind the vessel can be studied. The previous chapters have found several parameters influencing these processes. A reference run and parameter study are done to find study these effects. The runs are discussed in three steps.

First, the return current in a two layer system is studied with a focus on velocity gradients in the model and potential shear instabilities. Also of interest is how the flow pattern changes if the top layer is 'blocked' by the vessel and how the return current is influenced by the layer distribution and density profile. The next part of the analysis focuses on the interface deformation and the wave pattern on the interface. It looks at the characteristics of these interface motions and their contribution to mixing by either shear instabilities or internal wave breaking. The third part of the parameter study focuses on the amount of mixing observed and whether this can be attributed to the return current or internal waves.

5.1.2. Reference case

As a reference for the parameter study and to study the effect of a ship in a canal in general, a run will be made based on parameters of the Noordzeekanaal. The canal is simplified to a rectangular canal of 220 m wide and 15 m deep without discharge. The density distribution is schematised as a two layer flow with a density difference of 10 kg/m^3 similar what is found in the NZK. This corresponds to a relative density difference, R0, of 0.01. A barge of 100 m long, 11 m wide and with a draught of 3.5 m sailing at 3 m/s is used. The mesh generation has been described in the previous chapter. At the ship hull, canal bed, and canal banks a Nikuradse wall roughness of 5e-03 m is applied following the method described in Chapter 4. For more detailed simulations, a difference between the roughness of the ship hull and the canal should be made. This value is for now good enough to study the processes and get insight in the amount of mixing.

Parameter		Value
Ship length	m	100
Ship width	m	11
Draught	m	3.5
U	m/s	3
Canal length	m	800
Canal width	m	220
Canal depth	m	15
h_1/h		0.5
R0		0.01

Table 5.1: Parameter values for the reference run

5.1.3. Parameter study

The parameters that will be varied are based on the previous chapter. Their expected influence is described in Section 3.3.3 and Section 3.4.

The canal blockage is varied by varying the draught of the vessel for a canal width of 220 m and 50 m wide. The analysis in Chapter 3 showed that median to maximum values for the canal blockage are in the range of 0.03 to 0.17 for the studied canals. The variations done explore this range. First, the draught is varied. A few of these runs are repeated for a 50 m wide canal to study larger canal blockages and to see whether the processes are determined by the draught or the canal blockage.

The internal Froude number is varied in several ways. This is done because it is not entirely certain whether the internal Froude number is a good predictor of the flow behaviour and amount of mixing. It is likely that the vessel speed, relative density difference, and density profile (variations of a two-layer and a linear profile) are more important in determining the flow response.

The vessel speed is varied from 0.5 to 7 m/s. The maximum sailing velocity in most canal is 5 m/s as discussed in Chapter 3. The relative density is varied from 0.001 to 0.020 with the former corresponding to density difference of 1 kg/m^3 and the latter to a density difference of 20 kg/m^3, which is close to the difference between North Sea water and fresh water. These density variations are repeated for a linear profile instead of a tanh-profile to study the effect of a different density profile. The layer distribution of the semi-two layer tanh-profile has been varied as well. Finally, a sloped canal bank is added to the canal to investigate the effect on the internal wave field. For these runs, the canal length is increased to 2000 m.

A run without a vessel is done for the different density distribution and mesh speeds. An empty canal with the characteristics of run 2 are used to compare to run 1 to 12. For run 13 to 28, a separate run has been done. These runs will be indicated as run 0 in this chapter. For run 29 to 36, no run without a vessel has been made.

Run	Canal width (m)	Draught (m)	Vessel speed (m/s)	R0 (-)	Density profile	h_1/h (-)	Slope of canal bank
1 to 8	220	1.5, 3.5, 5.5, 7.5, 8.5, 10.5, 12.5, 14.5	3	0.01	tanh	0.5	-
9 to 12	50	5.5 ,7.5, 10.5, 12.5	3	0.01	tanh	0.5	-
13 to 16	220	3.5	0.5, 1, 5, 7	0.01	tanh	0.5	-
17 to 20	220	3.5	3	0.001, 0.005, 0.015, 0.020	tanh	0.5	-
21 to 24	220	3.5	3	0.001, 0.005, 0.010, 0.015	linear	0.5	-
25 to 28	220	3.5	3	0.01	tanh	0.33, 0.20, 0.80, 0.67	-
29 to 36	220*	3.5	3	0.01	tanh	0.5	1 on 3, 1 on 4, …, 1 on 10

Table 5.2: Parameter values for the different model runs. *the width at z = -7.5 m is 220 m for all the runs with a sloped canal bank.

5.2. Reference case (Run 2)

In this section, the results of the reference run are described. This run is used to give an idea of the general flow pattern and to compare the effect of several parameters with. First, the general flow field is described. This is followed by a more detailed description of the effect on the interface, the internal wave pattern, and the velocity difference between the layers. This is followed by a discussion on the consequences for mixing.

5.2.1. General results

First, the effect on the interface (where the density is 1010 kg/m^3) is described. The interface can be seen in Figure 5.1. Similarly to the squat of a vessel in an unstratified canal, the interface is lowered at the location of the vessel (x = 5 to -96 m). The interface goes down underneath the vessel and moves up after the stern of the vessel in a hump higher than the original interface. This hump splits in two and moves in a V-shape behind the vessel, similar to a supercritical surface wave pattern. After a few hundred meter, a second V-wave appears within the first. The angle of the V-shape corresponds to the average found using the formulas given in Section 3.4.1.

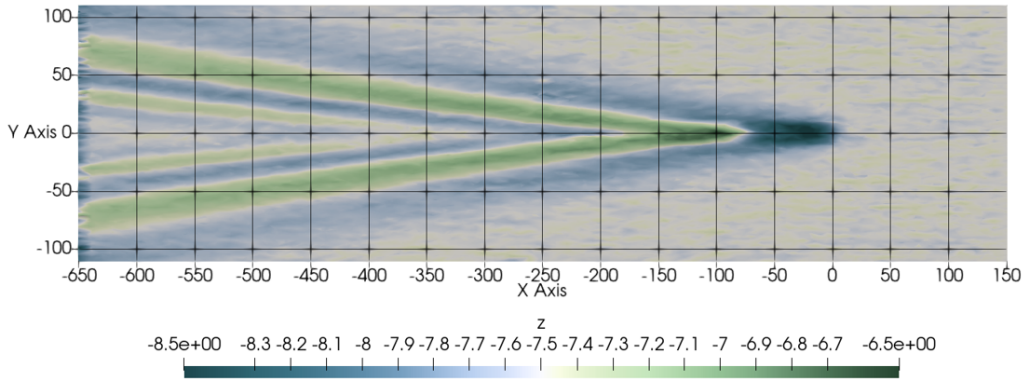

Figure 5.1: The contour plot of the height of the interface in m shows the interface squat and the wave field behind the vessel.

Next, the velocity field is described. In Figure 5.2, the velocities in x-,y-, and z-direction are visible. The velocities are largest around the vessel. In x-direction, the flow increases opposite to the sailing direction around the vessel. The wake of the vessel is directed in the sailing direction. In the y-direction, the flow is pushed sideways around the vessel, and the z-velocity plot shows how the flow is first moved underneath the vessel before it moves up again. Underneath the vessel at x = - 50 m, a clear velocity difference in y-direction between the layers is visible as the bow pushes water to the side, the water flows back inward at the bottom. The velocity plot in y- and z-direction also clearly shows the wave pattern. The wave system already starts underneath the boat as can be seen in the y-velocities at x = -50 m. The wave pattern can be seen as a mode 1 wave pattern.

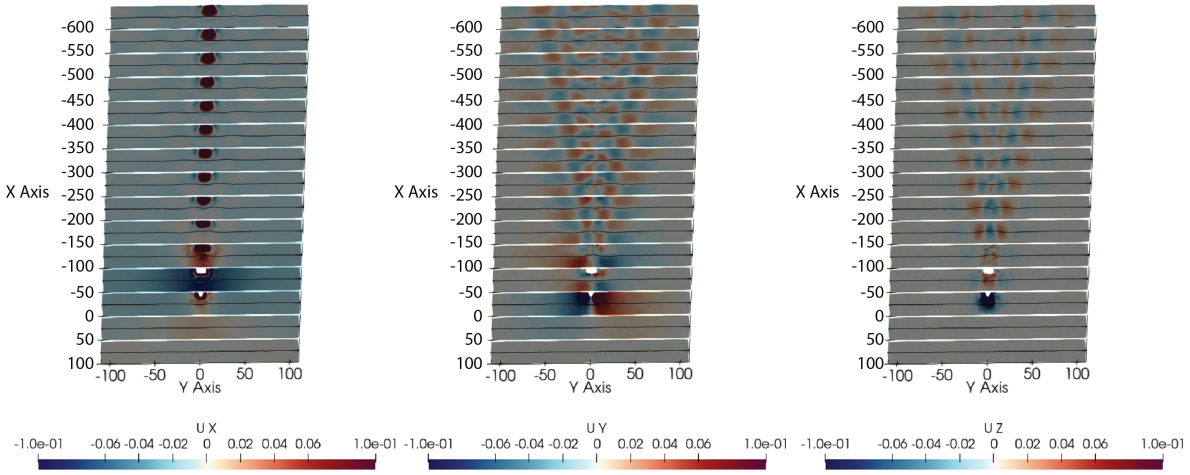

Figure 5.2: Every 50 m a slice of the velocity field in x-,y-, and z-direction has been taken. The interface between the layers is plotted as a black line. The return current and wave pattern are well visible. Except for in the wave pattern no clear velocity difference is visible between the layers. For better visibility of the flow patterns, the colour scale has been set from -0.1 to 0.1 m/s for each direction, even though higher velocities are reached around the vessel and in the wake. The z-axis is scaled with a factor 2.

5.2.2. Return current

Figure 5.3 zooms in on the return current around the vessel. The vessel pushes the water in the sailing direction and from there it moves around the vessel. The flow is accelerated under the vessel. At the stern of the vessel the streamlines move inwards again. The vessel leaves a long wake where the flow is following the vessel. High flow velocities are found underneath the vessel, especially at the bow and stern, where the water moves respectively down and up, and in the wake of the vessel. This is similar to the return flow in an unstratified system. No clear velocity difference between the layers is visible. The largest velocity difference is visible underneath the vessel for the velocities in x-direction. This is due to shear at the ship hull. Figure 5.2 shows a velocity difference in y-direction at the interface. Figure 5.2 also shows a long wake following the vessel in x-direction. The velocity difference with the surrounding fluid is large.

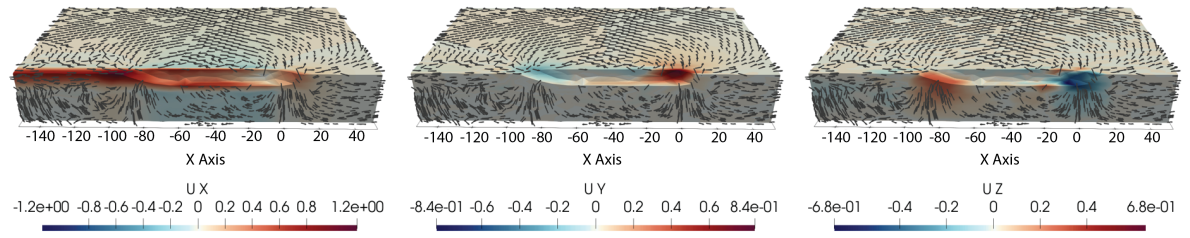

Figure 5.3: The velocity field in x-,y-, and z-direction around the vessel shows a return current around the vessel. The flow is forced around and under the vessel. The z-axis is scaled with a factor 2.

The Richardson number takes into account both the velocity and the density difference, and low values indicate shear instabilities or unstable stratification. At most places in the model, the velocity difference is so small that the Richardson number becomes extremely large. These have been removed from Figure 5.4. Low Richardson values can mainly be found at the vessel hull and at the bottom underneath the vessel. Some low values are also found directly behind the vessel. At the ship hull, a large velocity gradient is visible. At the bed, almost no velocity gradient is visible. The density gradient at the top and bottom of the canal is very small given the tanh-profile, so a small velocity difference is quickly large enough to give small Ri-numbers. The small Richardson numbers found therefore do not give a clear indication of mixing of salinity. At the mixing layer, the density gradient is large, which means that a large velocity gradient is needed for low Ri-numbers. This is apparently not the case, as could also be seen in Figure 5.2 and 5.3.

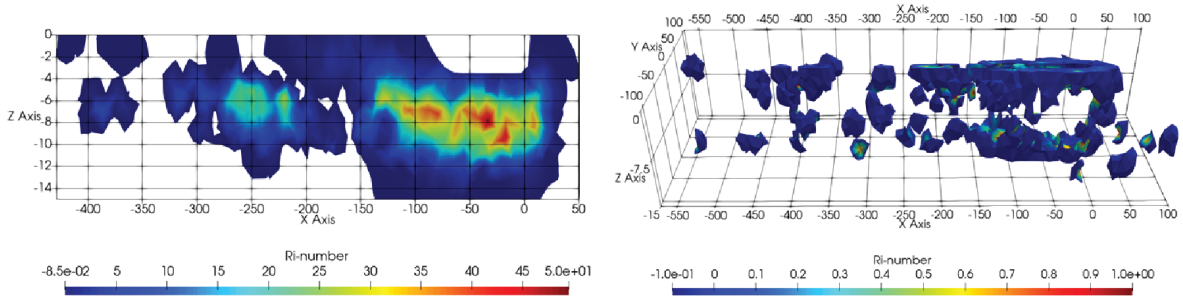

Figure 5.4: Richardson numbers found in the model with large Richardson values removed. Left: A slice at y = 0 (sailing line of the vessel) shows Richardson values up to 50. Right: Richardson values under 1 in the model, these small Richardson number can lead to mixing.

5.2.3. Interface deformations and internal waves

In this section, the interface deformations around the vessel and the internal wave field behind the vessel are described.

The undisturbed position of the interface is at z = -7.5 m. Figure 5.5 shows that the interface moves down to -8.6 m (about one meter down) underneath the vessel. It then start to move up and reaches a depth of -6.7 m (about one meter above the original position) behind the vessel. This rise of the interface already starts underneath the vessel as the cross section of the vessel becomes smaller from that point on.

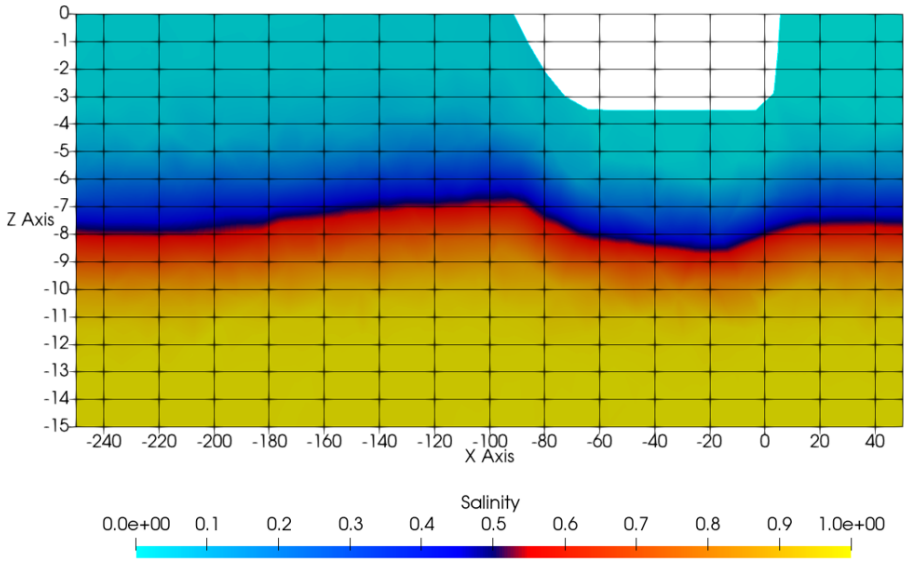

Figure 5.5: The interface deformation at the vessel sailing line (y = 0 m). The interface first moves about one meter down before it moves up about one meter from its original position. The z-axis in this figure is scaled with a factor 10.

Figure 5.6 shows a detailed view of development of the wave field. The hump behind the vessel has a height of 1.2 m above the interface. 100 meters behind the vessel, the hump has split into two waves with a height of 0.5 m above the interface and 0.3 m below the interface. The wave crest is initially narrow and high, while the trough is long and flat. The wave height is decreasing over the length of the canal. From x = -400 m on, a second V-wave starts to develop. At x = -600 m , the wave troughs are reaching the side slopes. The domain is too short to see the full effect of the waves. The wave steepness is about 0.01.

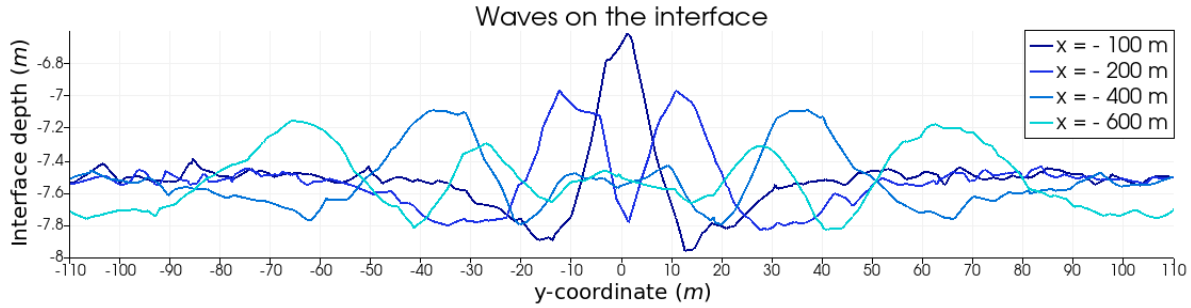

Figure 5.6: Development of the wave field behind the vessel at x = -100 m (directly behind the vessel), -200 m, -400 m, and -600 m. The initial hump behind the vessel splits into two waves that are moving outwards in a V-shape. At x = -400 m and -600 m, the second V-wave is visible between the original V-wave shape.

The orbital motion of the wave field cause velocity differences in the y-direction in the wave field as could be seen in Figure 5.2. This is not clearly recognisable in the low Richardson numbers of Figure 5.4.

5.2.4. Mixing

The effect of the disturbance on mixing cannot be easily determined. Comparing the density profile at the in- and outflow boundary to a run with an empty canal shows a larger spread for the run with a vessel, however, this can be explained by the waves on the interface at the outflow boundary (see Figure 5.7). Also, a slight change in the mixing layer steepness is visible compared to the inflow boundary. This effect is also visible for run 0 and therefore does not directly say something about the effect of the vessel. From this figure, no clear shift in the density profile can be observed.

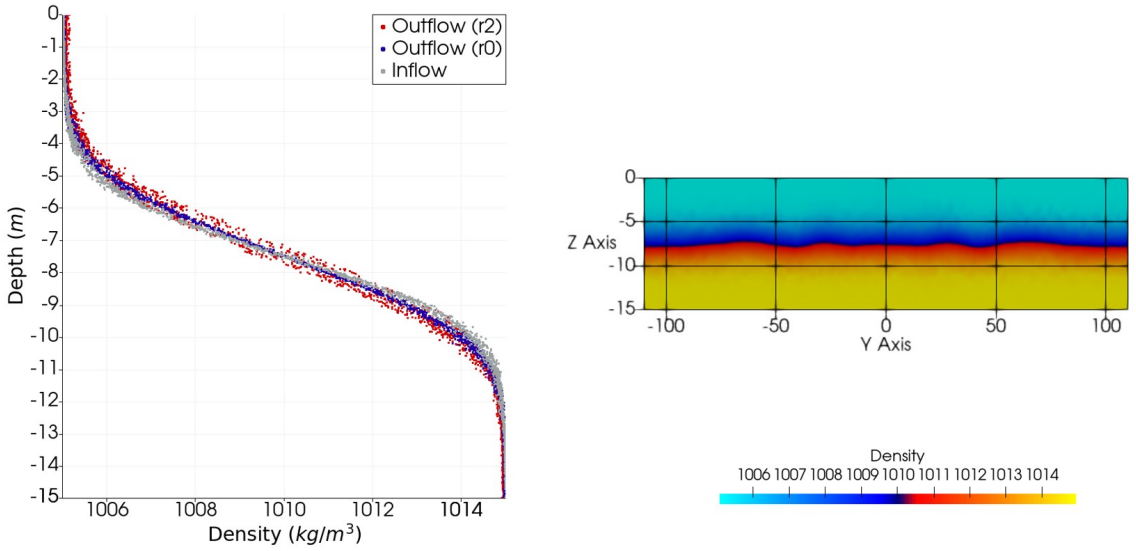

Figure 5.7: Left: Density profile over depth of all cell values over the width at 50 m from the in- and outflow boundary for run 0 (empty canal) and run 2. The density profile at the outflow seems to show a thicker mixing layer, however this is probably due to the waves on the interface as can be seen on the contour plot on the right. Right: Density contour plot at 50 m from the outflow boundary for run 2. The z-axis is scaled with a factor 4.

The PEA might give better insight in the amount of mixing as it takes into account the average density distribution. Figure 5.8 shows the width-averaged PEA and the PEA at every location of the model compared to run without a vessel. A clear decrease in PEA over the length of the canal can be seen. However, the run without a vessel also shows a decrease in PEA. The difference between the two lines can be contributed to the effect of the vessel. This contributes to about 2 J/m^3, which corresponds to about 1.2 % decrease of PEA. About half of this can be contributed to processes directly around the vessel and the other half originates from the wave field, however, the total effect of the wave field is not visible.

There is a small difference between run 0 and run 2 in the start-PEA on the right (see Figure 5.8). This can be contributed to velocity disturbances from the return current at the inflow boundary. The vessel could have been placed further from the inflow boundary to reduce this.

At the location of the hump behind the vessel (x= - 100 m) and at the wave crest of the second V-wave (see dark V-shape in Figure 5.8), the difference in PEA between run 2 and run 0 is largest. Additional mixing from for example a propeller could therefore be quickly effective in mixing the salinity distribution at these locations. This is especially relevant for the hump as this exactly the location where the propeller influence would be strongest.

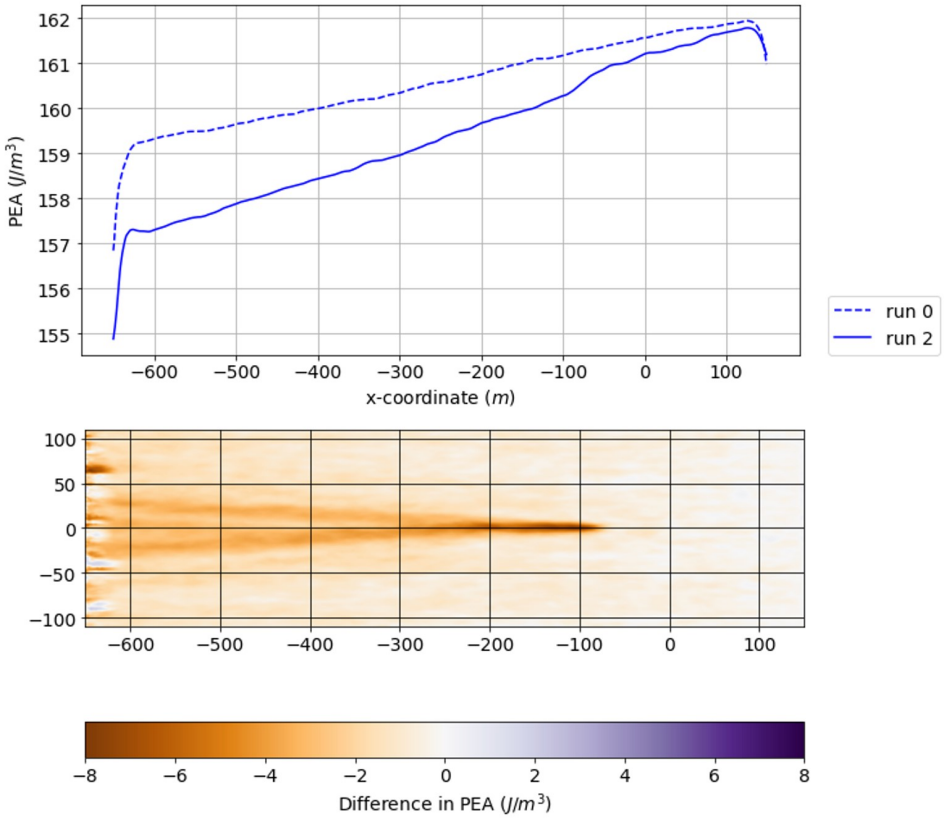

Figure 5.8: Top: Width-averaged PEA for run 0 (without a vessel) and run 2. The difference between the two lines is contributed to the vessel disturbance. Note: In the simulations the ship is moving from left to right. $5 < x > 96$ m is the location of the vessel. The PEA is decreasing underneath and behind the vessel. Bottom: Difference in PEA between run 2 and run 0. The difference in PEA is largest directly behind the vessel and at the wave crest of the second V-waves.

Relatively, the decrease in PEA is small for this run. Both processes around the vessel as processes in the wave field contribute equally to this decrease. Small Richardson values around the vessel indicate shear instabilities due to the large velocity gradient at the ship hull. These low Ri-numbers correspond with the quick drop in PEA at that location. Both the high velocities in the return current and the internal waves seem to contribute to mixing can be concluded from this analysis.

5.3. Canal blockage

The canal blockage has been increased by increasing the draught and by using a less wide canal. The draught has been increased with steps from 1.5 to 14.5 m in a depth of 15 m. A few runs with a less wide canal of 50 m wide have been run to achieve larger canal blockage ratios and to be able to compare the draught for different canal widths. The interface is at -7.5 m for each run.

5.3.1. Draught in 220 m wide canal (run 1 to 8)

First, the runs with a canal width of 220 m are discussed. The variable that is changed is the draught. This is done by lowering the ship hull deeper in the canal before creating the mesh. With an increase in draught, the canal blockage is increased.

Run	Draught	Canal blockage
1	1.5	0.0052
2	3.5	0.012
3	5.5	0.019
4	7.5	0.026
5	8.5	0.029
6	10.5	0.036
7	12.5	0.043
8	14.5	0.050

Table 5.3: Draught and canal blockage of run 1 to 8.

General results

A larger draught and a larger canal blockage gives a higher return current and higher waves. A larger canal blockage means that more water is moved by the vessel, so therefore the return current increases as well and this gives more shear. A larger draught means that the interface layer disturbed more, which increases the height of the interface motions. This gives more low Richardson numbers as can be seen in Figure 5.9. These effects combined give more mixing for a larger draught and canal blockage.

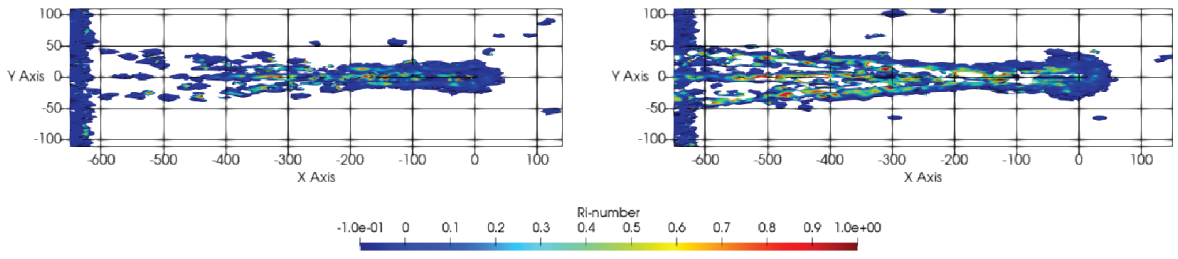

Figure 5.9: Negative to low Richardson values for run 3 (draught = 5.5 m, left) and run 8 (draughts = 14.5 m, right). Compared to Figure 5.4, the wave pattern is recognisable. For larger draught, the wave pattern, wake behind the vessel, and the return current show more low Richardson values that could indicate mixing.

Return current

A larger blockage factor leads to higher return current velocities. Figure 5.10 shows the velocities in x-direction for run 6 as example. The return current of run 6 is about double that of run 2 with velocities in the wake following the vessel even more than three times at high at some locations. Moreover, the shape of the wake changes for larger draughts. The wake becomes more triangular instead of half-round and continues deeper in the water column.

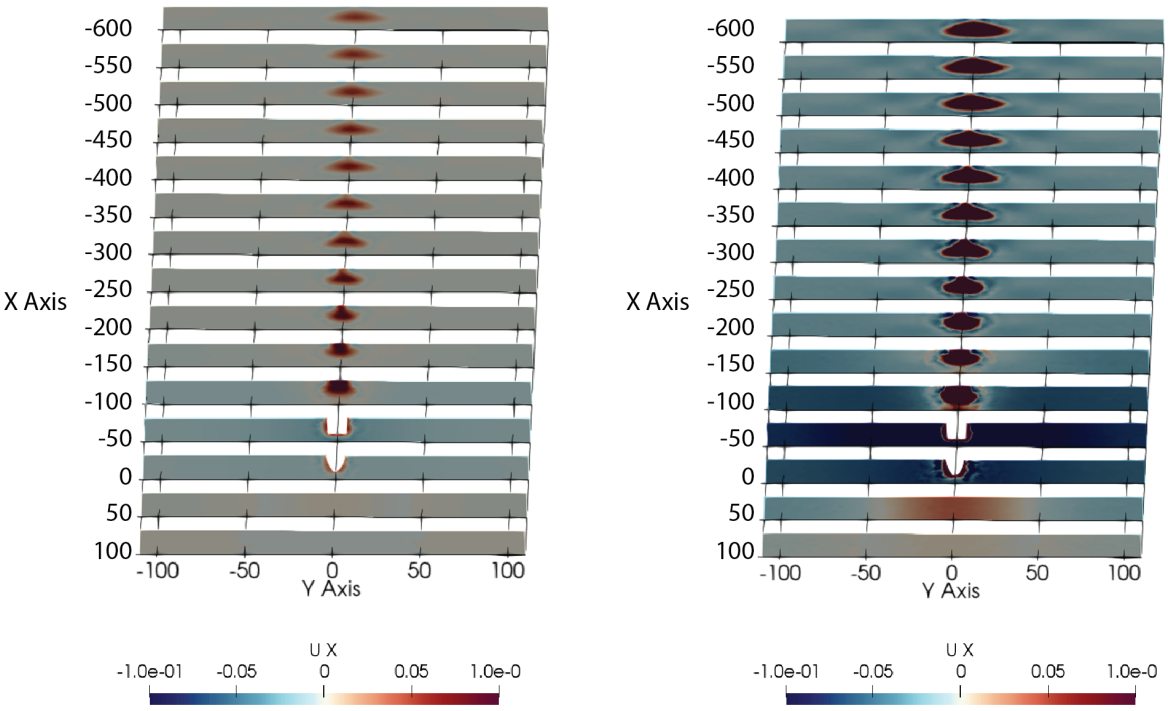

Figure 5.10: The velocities in x-direction for run 6, note the different scales of the x-velocities between left and right. The velocities are larger compared to the velocities for run 2 in Figure 5.2. This trend is visible for all larger canal blockages.

The changes in the wake are also visible in the Richardson values as can be seen in Figure 5.9. On the left, a difference with Figure 5.4 is already visible. In this figure, only the negative values or values below 1 are visible. For an increasing draught, the flow features are better recognisable. The figures on the right in Figure 5.9, show for example clearly the wave pattern and the wake behind the vessel. Also, the return current, especially water being pushed forward by the bow of the vessel, is clearly visible. Again, these low values mainly occur at the top and bottom of the water column. The density difference is small at these locations, and apparently the velocity gradient is large enough to give these low values.

Interface deformations and internal waves (run 1 to 8)

The draught has a clear influence on the squat of the interface as can be seen in Figure 5.11. The interface squat increases for increasing draught. For small draught, the interface is deformed at the location of the vessel and the most of the top layer flows underneath the boat.This is also the case for run 4 where the vessel draught is equal to the depth of the interface. Run 5 has a draught of 8.5 m. In this run, the interface comes up underneath the vessel and reaches the hull. For even larger draughts, the vessel moves through the interface between the layers, and therefore there is no interface squat in the middle of the vessel visible anymore, and the top layer flows around the vessel. It should be noted that the mesh quality is bad for the large draughts. The number of cells underneath the vessel is too low for the larger draughts. Furthermore, a draught of 14.5 m on a water depth of 15 m is not realistic. These runs do show largely the same trend as the other runs. Improving the mesh is outside of the scope of this research, however, this is a point of attention for a follow-up study.

Figure 5.12 shows the development of the interface squat and wave amplitude behind the vessel for increasing draught. Up to a d/h_1 ratio of 1 (see Figure 3.6 for the definition), the interface squat and wave heights increase in an almost linear line. The amplitude of the hump behind the vessel increases with the draught and is about equal to the interface squat for a draught between 3.5 and 7.5 m. From run 4 (draughts = 7.5 m), the hump reaches the level of the bottom of the boat, and from run 5 the hump is connected to the hull of the boat. For the smaller draughts, the wave height at x = - 200 m (100 m behind the vessel) is about half the wave amplitude directly behind the vessel, which means that the original hump behind the vessel has split into two. This is not the case for larger ratios of the

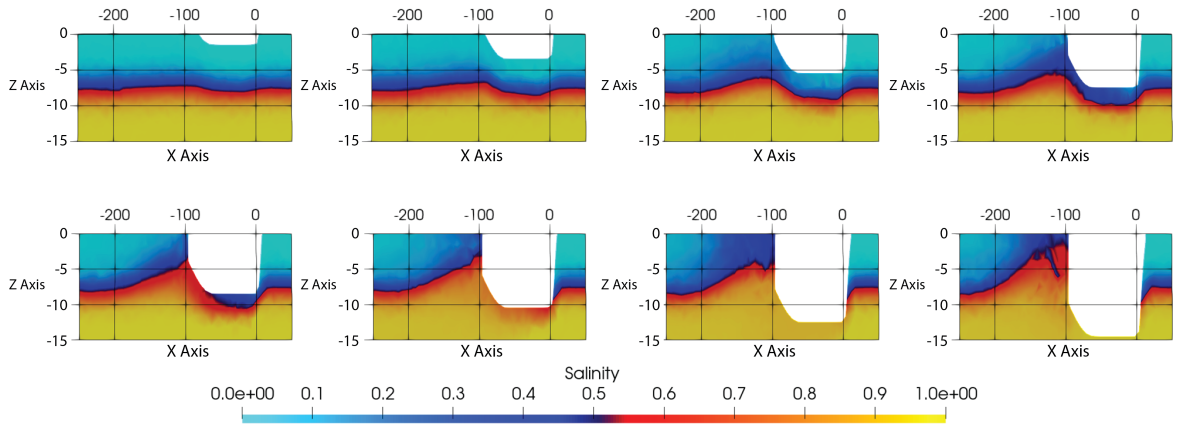

Figure 5.11: Interface deformation underneath the vessel at the sailing line (y=0). The top layer is forced underneath the vessel for the smaller draughts and the interface is deformed. For larger draughts, the top layer flows around the vessel completely. The z-axis is scaled with a factor 10.

draught/interface depth. Except for run 7, the ratio between the wave amplitude behind the vessel to the wave height at x = - 200 m is around three for these larger ratios.

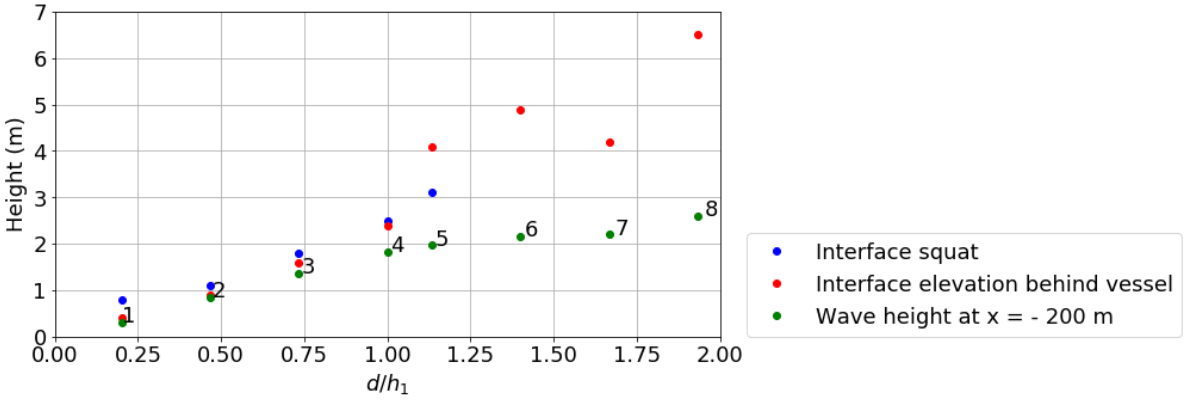

Figure 5.12: The interface squat relative to the interface increases almost linearly for an increase in draught to top layer ratio, d/h_1. The wave amplitude directly behind the vessel also shows a linear increase with larger draughts, however, for a draught/interface depth larger than 1, the wave is stuck to the ship hull and the linear increase is no longer visible. For a d/h_1 smaller than or equal to one, the original hump behind the vessel splits into two waves behind the vessel. For larger draughts, the wave amplitude at x = - 200 m is damped (see main text).

Run 1 deviates a little as the ship hull is too far from the interface to have big influence on it. For the larger draughts, the vessel is sailing through the bottom layer as well and no interface squat is visible anymore and the ratio of the wave amplitude behind the vessel and the wave height at x = - 200 m is changing. The wave height at x = - 200 m does not show an increase for the larger draughts. The amplitude of the waves is likely to be damped by the restricted water depth and layer thickness. Due to the wave motion, the top layer becomes less high for a wave top for example.

As noted before, Figure F.3 shows that for larger draughts the wave pattern becomes better recognisable in the low Richardson values. This is due to the higher velocities in the wave field due to the larger waves. Figure 5.13 shows this more clearly. The velocities in y-direction are oppositely directed at both sides of the interface. The orbital velocities are largest at the wave top and trough. The highest velocity differences between the layers and lowest Richardson numbers are therefore found at the location of the wave tops and troughs.

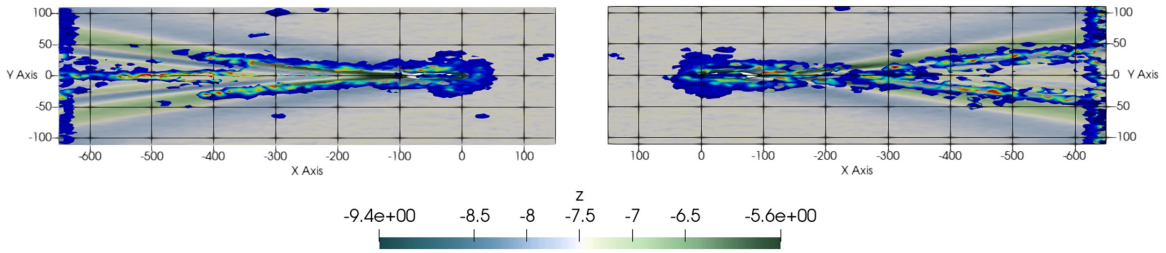

Figure 5.13: Top (left) and bottom (right) view of negative low Richardson values for run 8 combined with a contour plot of the interface height shows that the low Richardson numbers at the top correspond to the wave tops and the low Richardson numbers at the bottom to the wave trough.

Mixing

To show the influence over the length of the canal, the PEA averaged over the width of the canal relative to run 0 has been calculated in Figure 5.14. A larger draught causes a larger decrease in PEA. The PEA decreases in two big steps in front and behind the vessel. The Ri-numbers showed the wave pattern more clearly for the larger draughts, as the velocities of the orbital motions become larger and move in opposite direction for the top and bottom layer. The decrease of PEA in the wave field is also larger for the larger draughts.

A large difference between run 3 and run 4 is visible. Run 3 is the last run where the vessel sails over the interface. The draught of run 4 is equal to the interface depth. Figure 5.11 shows that there is more disturbance of the density field for run 4 than run 3.

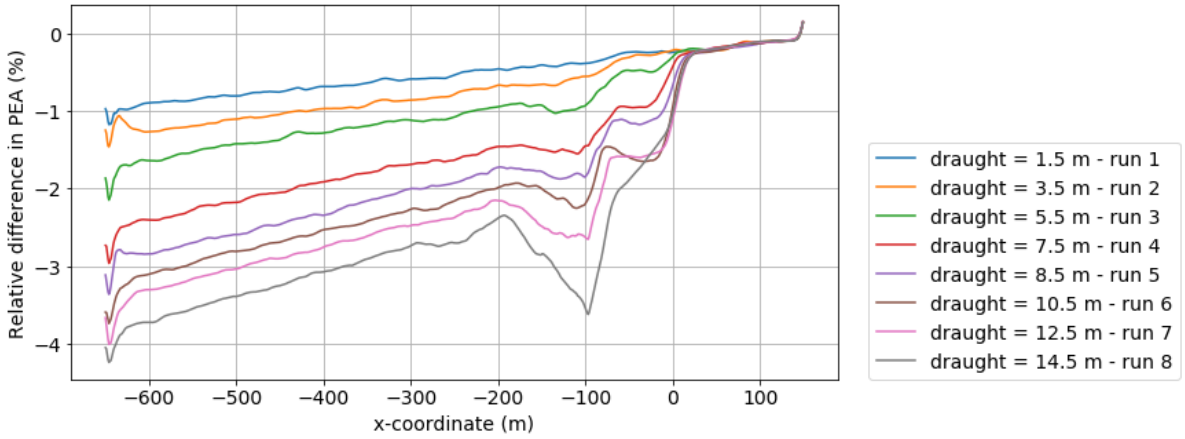

Figure 5.14: The relative decrease in width-averaged PEA of run 0 to 8. An increase in draught means a larger decrease in PEA.

This effect is also visible when comparing the changes in density profiles as Figure 5.15 shows. The change in density is larger for the top of the water column than the bottom of the water column.

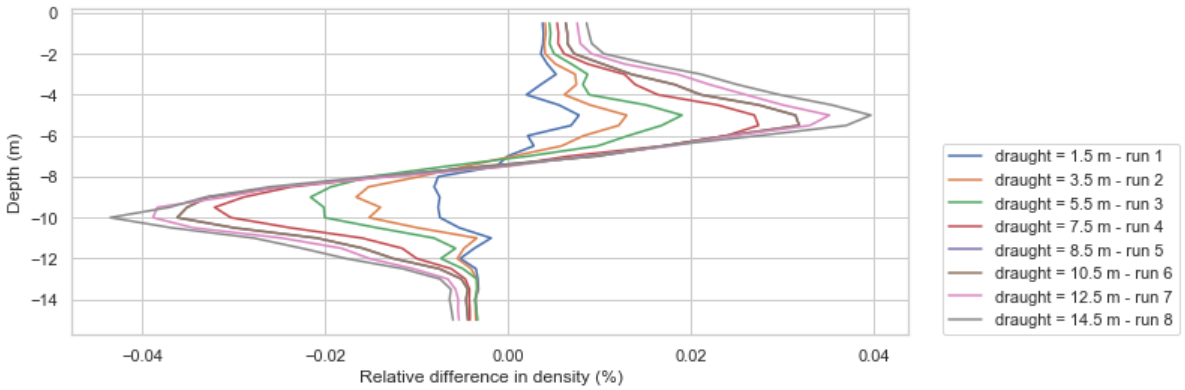

Figure 5.15: The difference in width-averaged density profiles at the outflow boundary ($x = -600m$) between a run without and with a vessel shows a larger effect for a larger draught.

5.3.2. Comparison with a 50 m wide canal (run 9 to 12)

The runs with a smaller width have been executed to have data on a larger canal blockage and to whether effects are mostly influenced by the canal blockage or the draught. A larger canal blockage was reached by repeating a few runs (run 3, 4, 6, and 7) with a more narrow canal. The canal width is 50 m instead of 220 m.

Run	Draught (m)	Canal blockage
9	5.5	0.084
10	7.5	0.12
11	10.5	0.16
12	12.5	0.19

Table 5.4: Draught and canal blockage of run 9 to 12.

General results

The main difference between the runs in a wider canal is that the runs in a less wide canal have a higher return current due to the larger canal blockage. The small canal width also results in wave reflection at the canal banks.

Return current

Figure 5.16 compares the velocity in x-direction for a draught of 5.5 m in a 50 m and 220 m wide canal. The higher velocities due to the larger canal blockage are clearly visible in the smaller canal. The maximum return current velocity around the vessel is about twice as large. The high velocities due to the return current reach also the canal banks. For even higher canal blockages, these velocities increase even more. Figure F.3 in the appendix shows a comparison of the low Richardson numbers for these runs. No large difference is visible in the pattern. The values around the vessel seem to be slightly lower for the smaller canal.

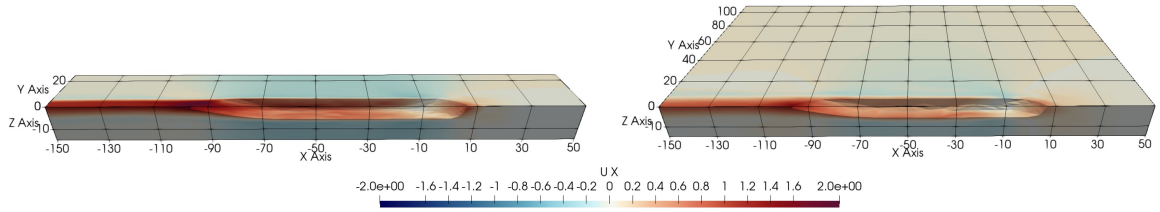

Figure 5.16: Velocity in x-direction around the vessel for run 9 (left, canal of 50 m wide) and run 3 (right, canal of 220 m wide). Both runs have a vessel with a draught of 5.5 m.

Interface deformations and internal waves (run 9 to 12)

The smaller canal means that the waves are reflected a few times against the banks of the canal as can be seen in Figure 5.17. The canal is less wide than the wave length observed in the reference run. The high amount of wave reflection make the results hard to interpret.

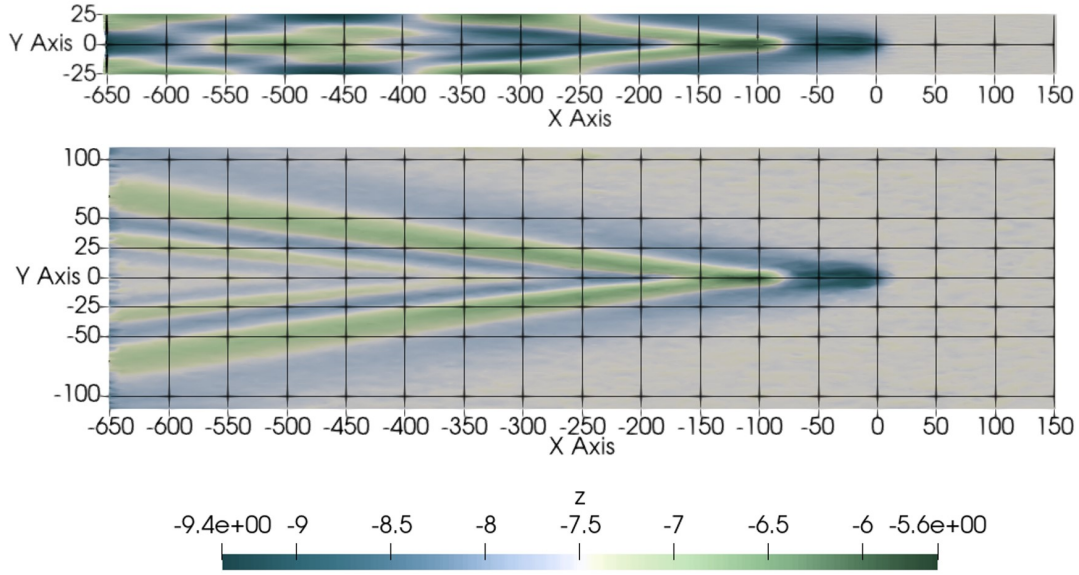

Figure 5.17: From top to bottom: Interface height in m for run 9 (top) and run 3 (bottom), both have a draught of 5.5 m. A less wide canal results in wave reflection at the banks of the canal.

Figure 5.18 and Figure 5.19 show that not the canal blockage, but the draught is important in the interface deformations. The data for a canal of 50 m wide shows the same pattern as the canal of 220 m wide.

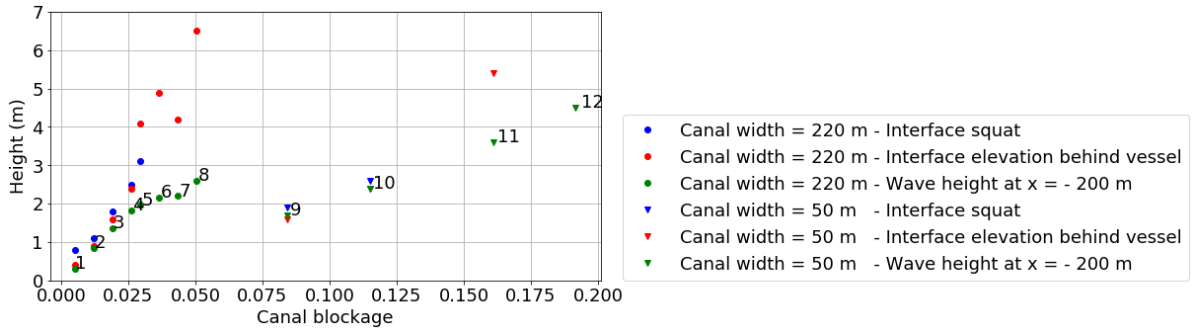

Figure 5.18: An increase in canal blockage does not necessarily result in higher wave heights. An increase in draught does result in higher wave heights as can be seen in Figure 5.19.

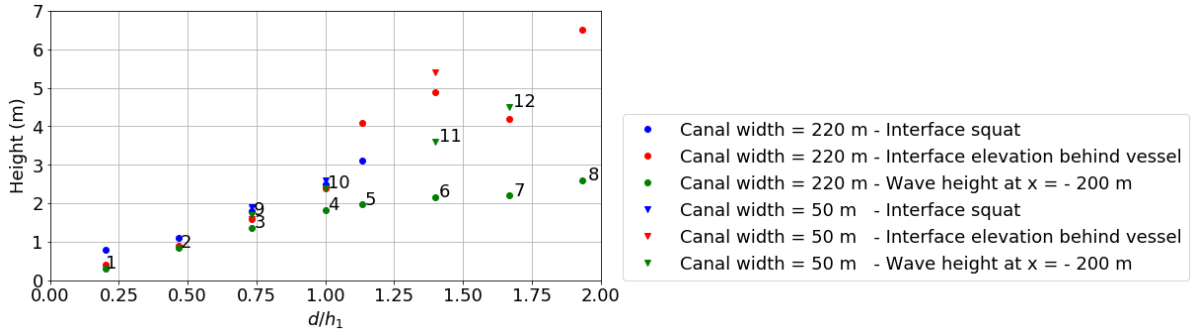

Figure 5.19: An increase in the draught to top layer ratio results in larger interface deformations. The same pattern as in Figure 5.12 is visible. The values of the different canal widths largely overlap, except for a d/h_1 ratio of 1.67.

Mixing

The PEA in Figure 5.20 has a lot of influence from the wave field and the reflection of the waves. That makes it hard to see the decrease in PEA well. Especially for the larger draughts, the PEA drops quickly around the vessel. This is due to the high return current and the shear around the vessel hull and the canal bed and banks, but also due to the low number of cells underneath the vessel in the mesh. The relative drop in PEA for run 9 is equal to the relative drop in PEA for run 3. For the other runs, the PEA decreases much more for the smaller canal. Figure F.2 shows also a larger change in density for larger draughts.

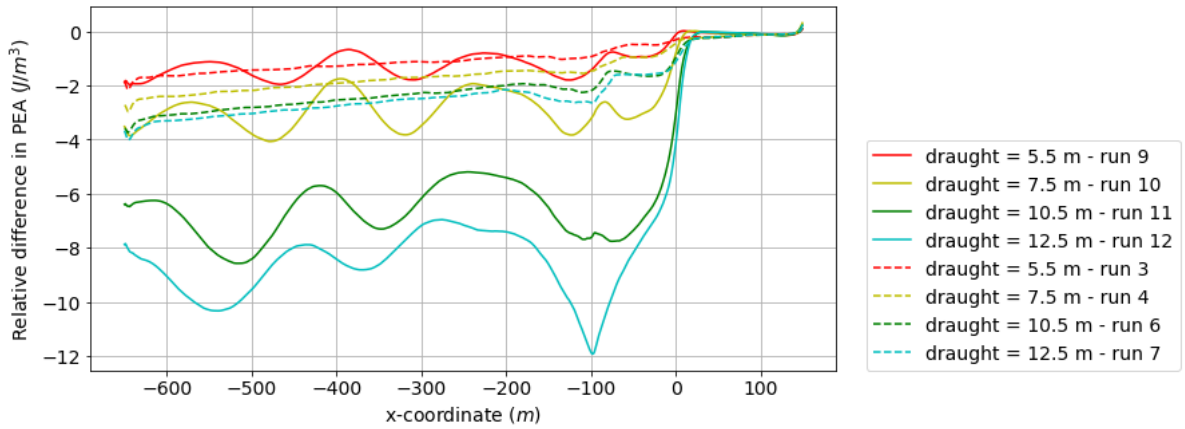

Figure 5.20: For a less wide canal, the PEA also decreases faster for larger draughts. However, due to internal waves reflecting at the sides of the canal and the small canal width, the PEA is not decreasing in a straight line.

5.4. Internal Froude number

The internal Froude number is dependent on the vessel speed and the internal long wave speed, which is dependent on the salinity distribution. The vessel speed, density difference, layer distribution has been varied, and a few runs with a linear profile have been done. First, the results of the variation in parameters of these runs is discussed and then a comparison is made between them to see the influence of the internal Froude number. It is expected that both the internal Froude number as the individual parameters have an influence on the flow field around the vessel as has been described in Section 3.3.3 and Section 3.4. Therefore, variations in both vessel speed and density profile have been done. The expected wave angle for each run is calculated using the formulas given in Section 3.4.1.

5.4.1. Vessel speed

The vessel speed has been varied from 0.5, 1, 3 (run 2), 5, and 7 m/s. A higher vessel speed results in a higher internal Froude number as can be seen in Table 5.5. Run 13 (vessel speed of 0.5 m/s) is subcritical, all the other runs have supercritical flow.

Run	U	Fr_i	Fr	Fr_c	$Fr_{c,L}$	ϕ	ϕ_L
13	0.5	0.041	0.82	0.050	0.019	-	0.49
14	1	0.082	1.6	0.050	0.019	0.65	0.24
15	5	0.41	8.2	0.050	0.019	0.12	0.047
16	7	0.58	12	0.050	0.019	0.086	0.033

Table 5.5: The vessel speed in m/s for run 13 to 16. The Froude numbers are calculated as well as the expected wave angles in rad.

General results

A larger vessel speed gives a larger return current as the ship moves water at a faster speed. The ratio between the internal wave speed and the velocity of the ship also changes which results in a smaller wave angle for higher vessel speeds. Figure 5.21 shows these wave patterns clearly. The different pattern for run 13 is also clearly visible.

The result of run 13 and 14 behave in a different way than expected when looking at the velocity shear and amount of mixing. It is expected that a low sailing velocity gives low velocities in the model and therefore less mixing. This is not the case. These runs show low Richardson numbers throughout the model (see Figure F.7 in the appendix). Figure 5.22 shows the width-averaged PEA for these runs.

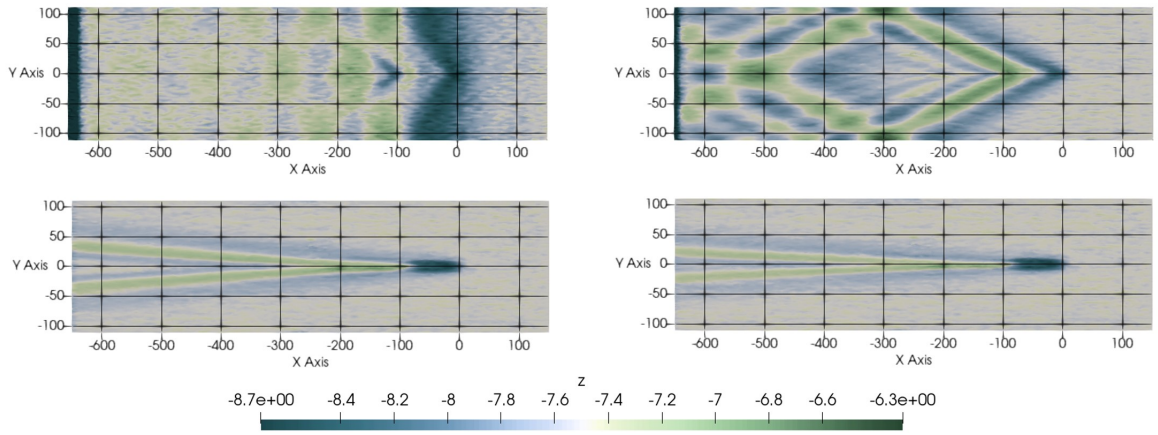

Figure 5.21: From left to right, top to bottom: contour plot of the interface for a ship sailing 0.5, 1, 5, and 7 m/s. The waves are almost not distinguishable for a speed of 0.5 m/s. For higher vessel speeds, the wave angle decreases according to the theory.

Figure F.4 in the appendix shows the relative decrease in PEA for these runs. The PEA has been plotted relatively to the run without a vessel with the same speed.

The PEA of these runs decrease quickly both with and without a vessel. It is unclear why this is. The movement of salinity through the model is equal to the velocity of the mesh which is proportional to the numerical diffusion. This means that a lower velocity would return in lower diffusion. However, in terms of distance travelled by the vessel, these runs show a relatively longer area. These two effect should have about the same impact and cancel each other. Why this is not the case is unclear. Figure F.7 also shows low Richardson numbers everywhere in the model for these runs. It could be that the adaptive polynomial order transport scheme makes the solution too smooth as it has a larger effect for a small speed. A linear polynomial order transport scheme might in that case give better results, however, this has not been tested. Run 13 and 14 will be considered as outliers due to this strongly increased mixing, although the wave pattern looks as expected.

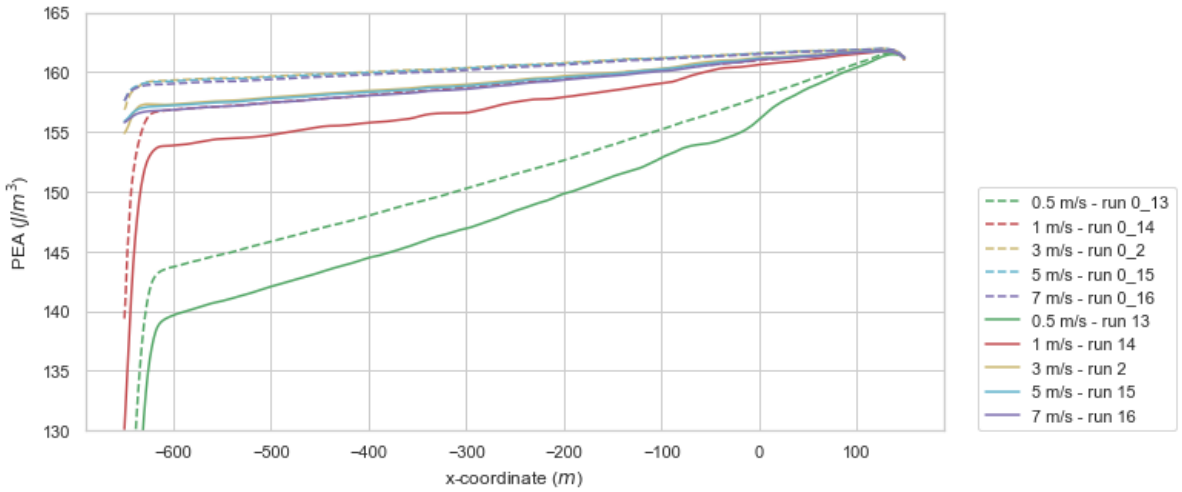

Figure 5.22: Width-averaged PEA over the length of the canal for runs of different speed. The runs with a speed of 0.5 and 1 m/s show a much faster decrease. The other runs are comparable with run 2.

Return current

The return current velocities vary with the vessel speed. The maximum return current velocity in the x-direction in the wake following the vessel is 1.98 ms/ for run 15 and 2.78 m/s for run 16. The return current around the vessel has a maximum value of -0.37 m/s for run 15 to - 0.53 m/s for run 16. The velocity differences underneath the vessel increase for the larger vessel speeds. Run 15 and 16 both

show low Richardson numbers around the vessel very clearly and some low Richardson values in the wake (see Figure F.7 in the appendix).

Interface deformations and internal wave field

Figure 5.21 shows how the wave angle increases for an increasing internal Froude number. Figure 5.1 fits exactly in between the second and third figure. The wave angles found correspond to the average of the values in Table 5.5, with run 13 as an exception. The wave heights for run 15 and 16 are comparable.

The maximum interface squat underneath the vessel is for all runs around 1 meter, just as in run 2. However, the pattern underneath the vessel is a little different, see Figure 5.23. For run 15 and 16, the interface height rises a little underneath the vessel and comes up behind the vessel. It does not decrease quickly behind the vessel as can also be seen in the contour plots (Figure 5.21).

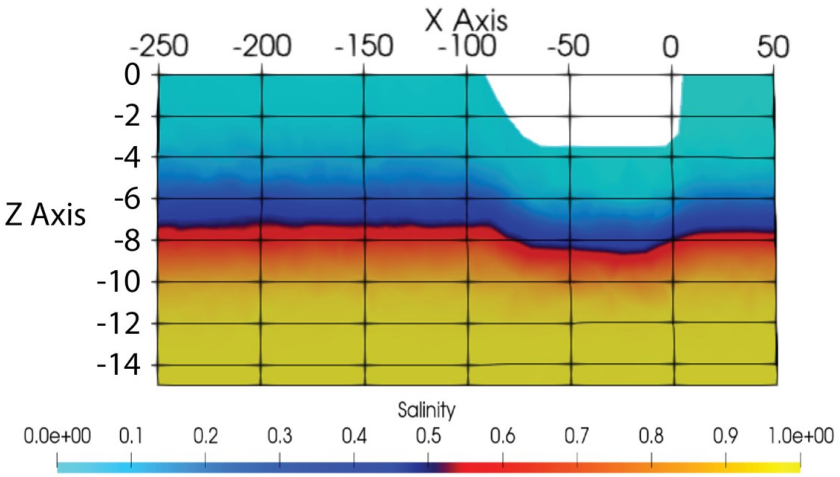

Figure 5.23: Interface deformation underneath the vessel for run 16. Compared to the reference run (Figure 5.5), the interface behind the vessel is flatter.

Mixing

Run 15 and 16 show a larger decrease in PEA than run 2, which can be related to the higher vessel speed and the higher return current (see Figure 5.24. The difference is however small. Figure F.6 in the appendix shows the change in density profile for these runs. This shows the same pattern as was discussed above.

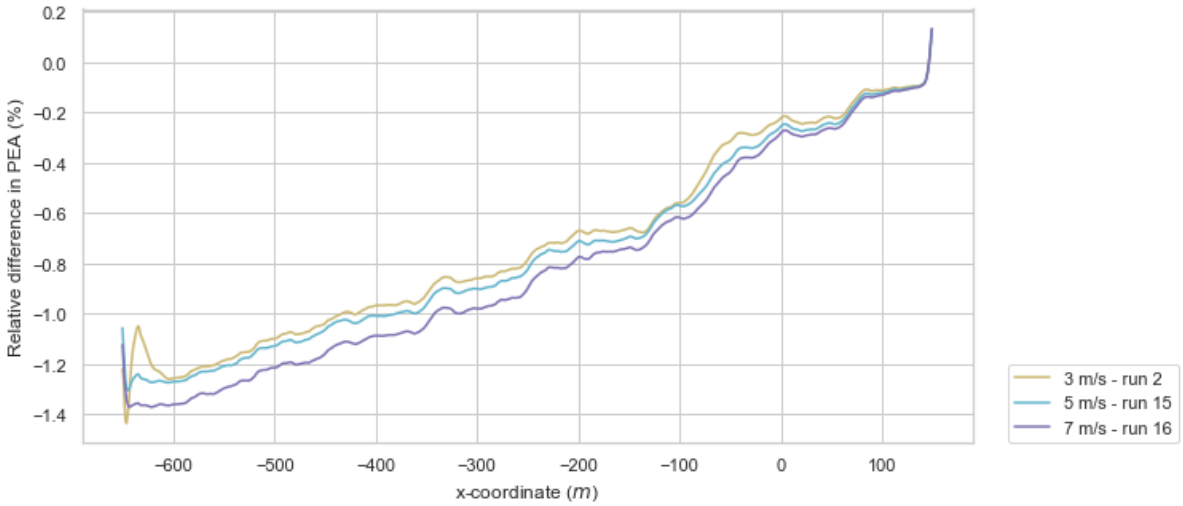

Figure 5.24: The width-averaged PEA for run 2, 15, and 16. For a larger sailing velocity, the amount of mixing increases.

5.4.2. Relative density difference (run 17 to 20)

Four runs have been made with a varying relative density difference, see Table 5.6.

Run	$R0$	Fr_i	Fr	Fr_c	$Fr_{c,L}$	ϕ	ϕ_L
17	0.001	15	0.25	0.064	0.025	0.64	0.25
18	0.005	7.0	0.25	0.14	0.055	0.14	0.055
19	0.015	4.0	0.25	0.25	0.095	0.25	0.095
20	0.020	3.5	0.25	0.29	0.11	0.29	0.11

Table 5.6: Run characteristics of run 17 to 20. The relative density difference has been varied from 0.001 to 0.02. Run 2 has a R0 of 0.01. The wave angle is given in rad.

General results

The internal Froude number of these runs is larger than the previous variations which results in a smaller wave angle. Instead of varying the vessel speed, the density profile is changed to change the internal Froude number. Aside from small changes in the wake of the vessel, almost no differences are observed for the return current. The interface deformations and internal waves are influenced by the density difference and become larger for a larger density difference as the reduced gravity term for the internal waves increases.

Return current

At the bow of the vessel, no clear velocity difference between the runs is visible. For the velocity in x-direction, the most noticeable difference is visible when comparing the wake following the vessel. The depth of the wake is larger for the higher density differences (see Figure 5.25). This is different from what would have be expected when looking at for example Figure 2.10 where the propeller wake behind a vessel is less deep for higher density differences. However, in this case, the wake is part of the return current and not caused by a propeller. There are also disturbances from the wave field behind the vessel. Figure F.10 in the appendix shows that the velocity in x-direction follows the shape of the layers and that higher density differences give larger deformations. The wake is less deep where the interface comes up and becomes deeper when the interface moves down again.

A difference is also visible in the Richardson numbers (see Figure F.11). For the smallest density difference, low Richardson values are only found around the vessel. As the density difference increases, more low Richardson numbers are found in the wake and in the wave field due to the higher velocities.

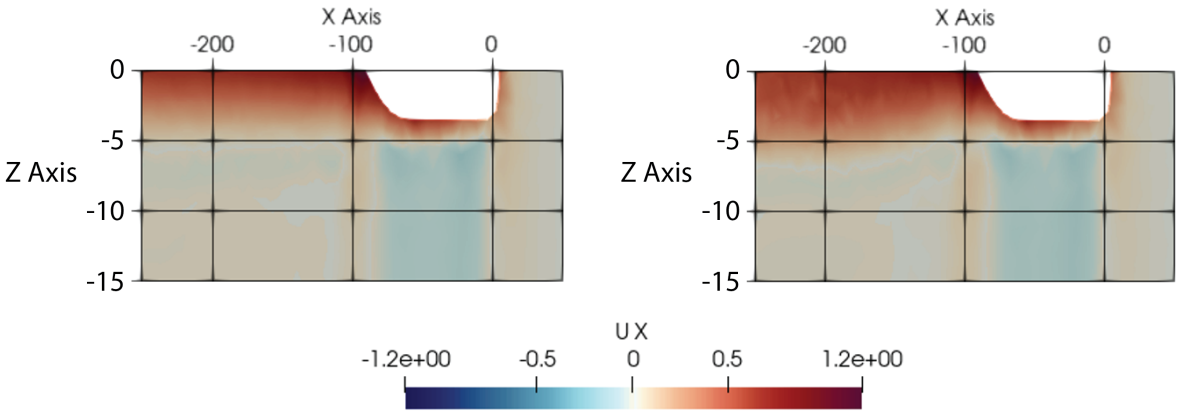

Figure 5.25: Velocity in x-direction in m/s for run 17 (left, $R0 = 0.001$) and run 20 (right, $R0 = 0.02$). A higher relative density difference gives a deeper wake behind the vessel. This wake continues at a lower depth compared to the lower density differences. At the top of the water column, the wake is smaller in width, giving an almost triangular shape at x = - 600 m, compared to a half-round shape for run 17 at x = - 600 m. The z-axis has been scaled with a factor 10.

Interface deformations and internal waves (run 17 to 20)

Directly behind the vessel, small differences are visible due to the changes in wave pattern. In the wave field, the differences between the runs is clear. The higher waves as a result of the larger density difference give larger velocities.

Figure F.10 in the appendix shows the interface of run 17 to 20. In the run with the smallest difference (run 17) almost no effect is visible. The interface moves down at the location of the vessel to restore itself slightly higher than its original position. There is no distinct hump visible directly behind the vessel. Behind the vessel, the interface moves up slightly directly behind the vessel and stays at that level for about 100 m before it moves up slightly and splits in the familiar V-shape. Run 18 shows a similar result. Also for this run, the interface moves about one meter down from the original position. However, it moves up quicker and reaches higher after the vessel. This effect is larger for run 19 and 20. The squat of the interface does not change considerably, rather the moment the interface moves back up again is sooner and the slope is steeper. For the higher density differences, a higher and more distinct hump is visible behind the vessel.

Changing the density difference has an influence on the internal wave speed and the internal Froude number. A higher density difference therefore gives a larger angle of the V. The wave angle is about the average of the calculated wave angles in the table for each run. At the outflow boundary, the wave height of the wave height is also increased for larger density differences.

The velocity in y-direction shows large differences between the runs. As the density difference increase, the velocity gradient in y-direction underneath the vessel becomes larger as can be seen in Figure 5.26.

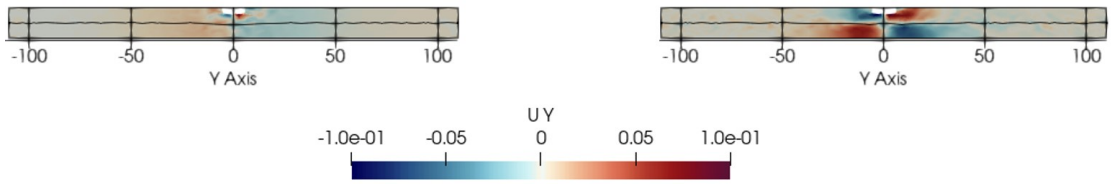

Figure 5.26: Velocity in y-direction in m/s at $x = -50$m for run 17 (left, $R0 = 0.001$) and run 20 (right, $R0 = 0.02$). The interface has been plotted as a black line. A higher relative density difference gives larger velocity gradients over the depth underneath the vessel. Compare also Figure 5.2.

Mixing

The PEA shows a larger decrease over the length of the canal for a larger relative density difference. In front of and at the location of the vessel there is almost no difference visible. The lower density differences have a slightly higher decrease at the vessel location, however this is probably due to

interpolation issues around the vessel. Another explanation would be that mixing is easier for the lower density differences. After the vessel, an increase in the slope of the PEA-decrease for larger relative density difference is visible, due to the higher waves. This seems to be the main difference between the runs. This would indicate that, even though there are differences in the flow field around the vessel, mainly the differences in the wave field contribute to more mixing for larger relative density differences. The difference in decrease in PEA between the runs is however small.

Where in the previous set of runs the difference in PEA started around the vessel due to the changes in return current, Figure 5.27 shows that the difference in PEA starts after the vessel. This highlights that for run 13 to 16 the change in return current was the main contributor to more mixing, while for run 17 to 20, the higher waves due to the higher density difference contribute to more mixing.

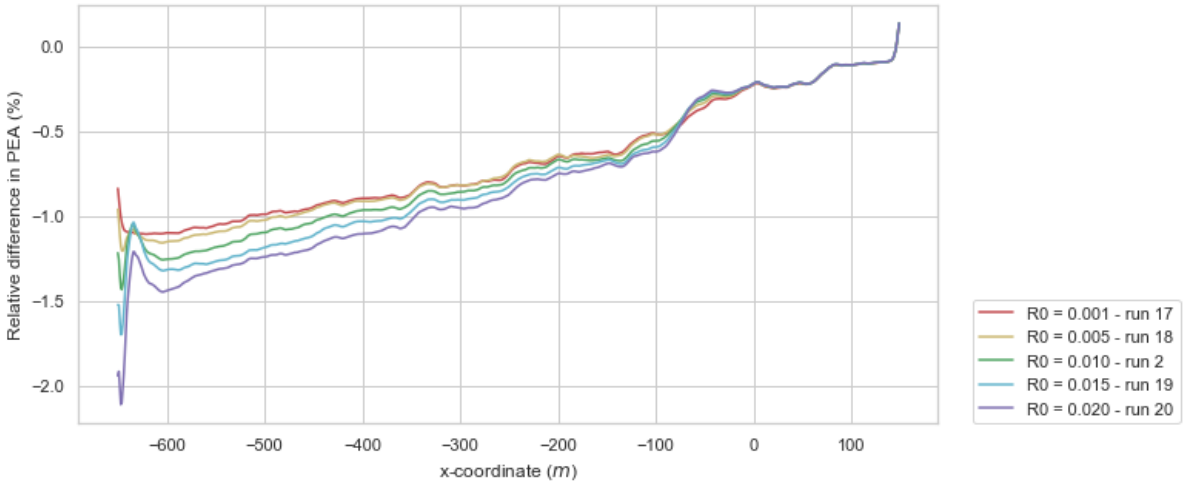

Figure 5.27: The width-averaged PEA for run 2 and 17 to 20. The changes in relative density difference influence the PEA only slightly. X-coordinate on the horizontal axis corresponds with the distance from the bow.

The change in width-averaged density profile between the run with and without a vessel is visible in Figure 5.28.

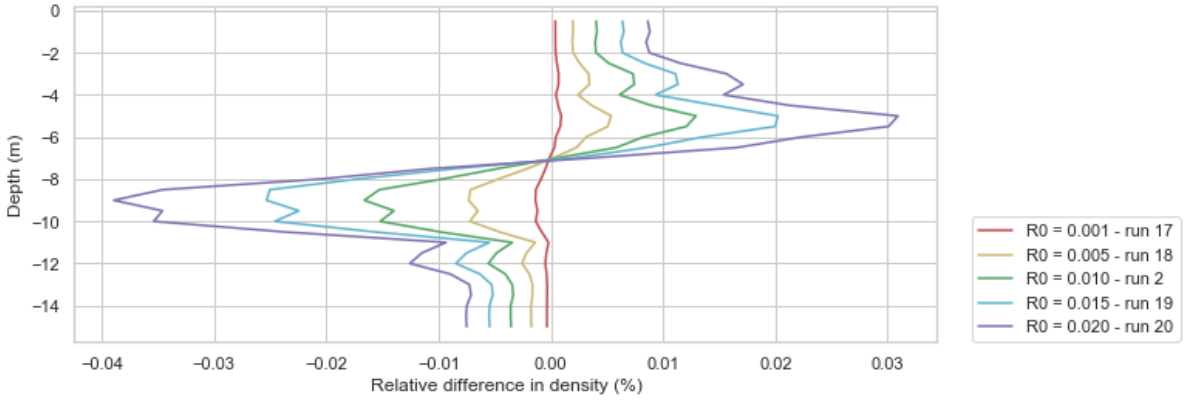

Figure 5.28: The width-averaged changes in density profile for run 17 to 20 compared to run 0 show an increase in effect for larger density differences.

5.4.3. Linear density profile (run 21 to 24)

A linear density profile can be seen as a transition from a two-layer system to a fully-mixed system. Instead of one interface layer, the density gradient is continuous. It is therefore expected that a linear system will result in more mixing. Four runs with a linear profile have been done with a varying relative density difference as can be seen in Table 5.7. The internal Froude number for a linear profile is taken as $Fr_i = \frac{U}{NH}$. It is unclear how the wave angle for a linear profile can be estimated.

Run	R_0	Fr_i
21	0.001	305
22	0.005	61
23	0.010	30
24	0.015	20

Table 5.7: Run characteristics of run 21 to 24. These runs have been done with a linear density profile.

General results

Compared to the previous runs with a tanh-density profile, the density gradient in run 21 to 24 is continuous over depth. This gives several differences in response of the flow. Figure 5.29 illustrates how the waves are spread over the entire depth of the water column for the linear case, while they are restricted to the mixing layer for the tanh-density profile.

The same relative density difference is now spread over the entire depth instead of limited to the mixing layer. This gives a continuous smaller density gradient over the depth. The Richardson number is therefore also found spread over the entire water depth (see Figure F.14).

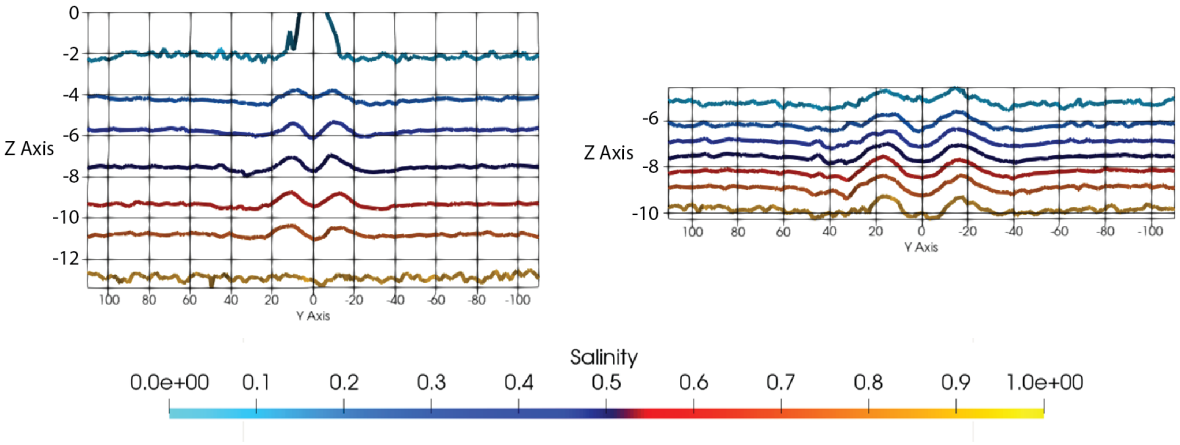

Figure 5.29: Comparison of the contour lines at x = -250 m for salinity = 0.25, 0.375, ..., 0.875 for the linear (left, run 23) and tanh-profile (right, run 2) show the differences in the wave field. For the linear profiles, the waves are spread over the entire depth of the canal, while for the tanh-profile the waves are limited to the mixing layer (see also Figure 5.7). The V-shape is more narrow for the linear case. The z-axis has been scaled with a factor 10.

Return current

The velocities show a similar pattern as has been observed for run 17 to 20. The wake of the velocity in x-direction reaches deeper for larger density differences and the velocity in z-direction shows a larger downward motion for larger density differences. A larger density difference results in higher velocities in the wave field. Overall, the velocities are lower compared to run 17 to 20. The low Richardson numbers are more spread out over the depth due to the change in density gradient (see Figure F.14). This is mainly visible for the low density differences, where the density gradient is smaller.

Interface deformations and internal waves

Almost no difference is visible between the interface deformations around the vessel for run 21 to 24. Figure 5.30 shows that there is almost no difference for the salinity = 0.5 line between a tanh-profile and linear profile with the same relative density difference. The decrease in height of the hump behind the vessel is slower for the linear profile. This is due to a more narrow angle of the wave field as the Froude number is higher.

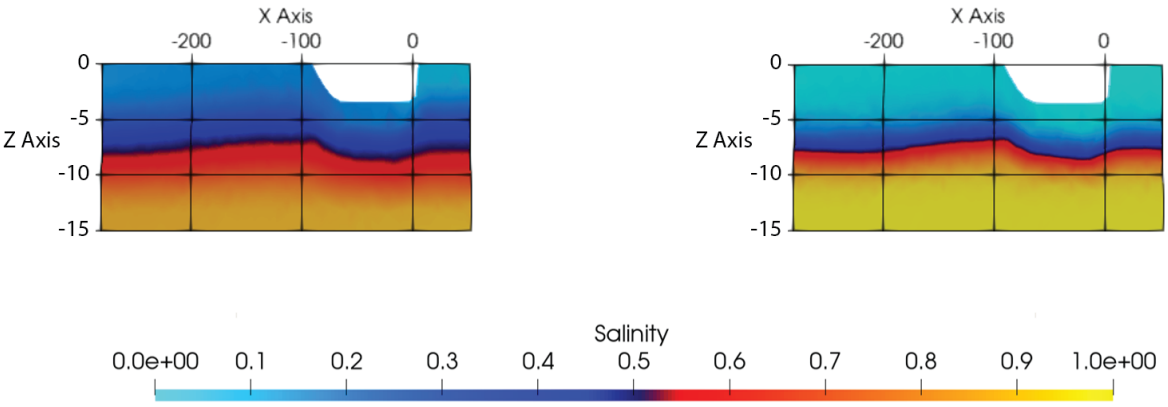

Figure 5.30: Left: Interface at y = 0 for run 23 (linear profile, R0 = 0.010). Right: Interface at y = 0 for run 2 (tanh-profile, R0 = 0.010). The interface deformation for salinity = 0.5 is equal for both runs, except for the part behind the vessel (x = -250 to -100 m). The z-axis has been scaled with a factor 10.

Mixing

The linear profiles give a different width-averaged PEA pattern than the tanh-profiles as can be seen in Figure 5.31. However, the relative decrease in PEA is again only slightly larger for larger density differences. The decrease in PEA is larger than for run 17 to 20. Figure F.15 shows the PEA at every location of the model for run 23. Different from Figure 5.8 is the increase in PEA at the location of the vessel (x = 0 to x = -100 m) and a more narrow profile behind the vessel due to the change in Froude number. The largest difference is -10.5 J/m^3 for the linear case instead of -8.5 J/m^3 as for run 2.

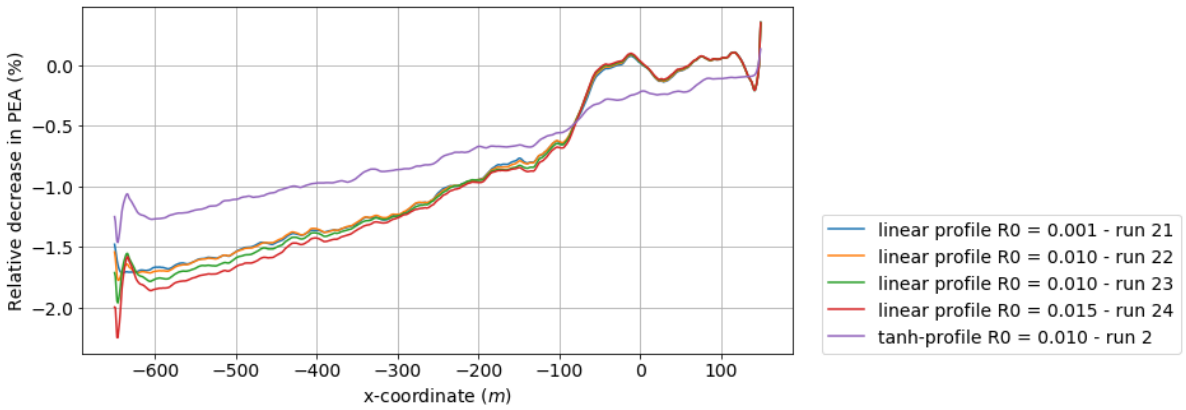

Figure 5.31: Relative difference in PEA for run 2, 21 to 24 and the corresponding runs without a vessel. The width-averaged PEA of the linear runs shows a different pattern than the tanh-runs (compare as well Figure 5.8 with Figure F.15). The PEA at x = - 600 m is lower for the same density difference. Again, a slight difference is observed for the different density differences. X-coordinate on the horizontal axis corresponds with the distance from the bow.

Figure 5.32 shows the change in width-averaged density profile between the runs with and without a vesel at the outflow boundary. Figure F.13 shows these density profiles.

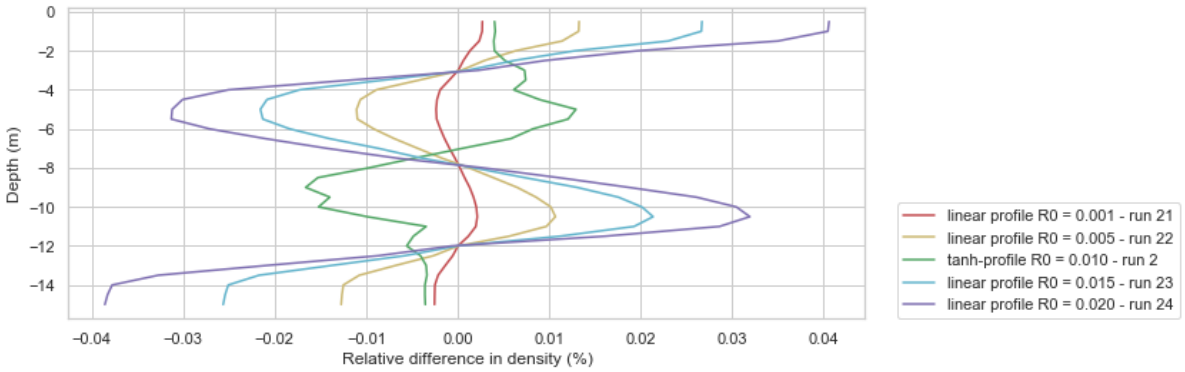

Figure 5.32: Relative difference in width-averaged density compared to a run without a vessel at the outflow boundary (x = 600 m) for run 21 to 24. A higher density difference results in a larger change of the density profile. The density profile moves from a linear profile to a tanh-profile. This happens for both the runs and the runs without a vessel. The top and bottom density move closer to the average value and the gradient becomes less steep for the runs with a vessel.

5.4.4. Layer distribution (run 25 to 28)

Finally, a variation in layer distribution has been made. In order of the run number, the interface depth is at -3, -5, -10, -12 m.

Run	h_1/h	Fr_i	Fr	Fr_c	$Fr_{c,L}$	ϕ	ϕ_L
25	0.2	6.2	0.25	0.040	0.015	0.16	0.062
26	0.33	5.2	0.25	0.047	0.018	0.19	0.073
27	0.67	5.2	0.25	0.047	0.018	0.19	0.073
28	0.8	6.2	0.25	0.040	0.015	0.16	0.062

Table 5.8: The layer distribution changes for run 25 to 28. The Froude numbers are calculated as well as the expected wave angles in rad.

General results

The layer distribution changes both the internal Froude number as the draught to top layer height ratio. Similar to what was seen in run 17 to 20, the wake following the vessel follows the deformations of the interface around the vessel. Other areas of the return current are largely unaffected by the changes in layer distribution. The interface deformations and internal waves are larger for a smaller h_1/h-ratio and largely follow the trend of the d/h_1-ratio discussed above. The closer the ship hull is to the interface, the more the interface is disturbed and the larger the interface motions as can be seen in Figure 5.33.

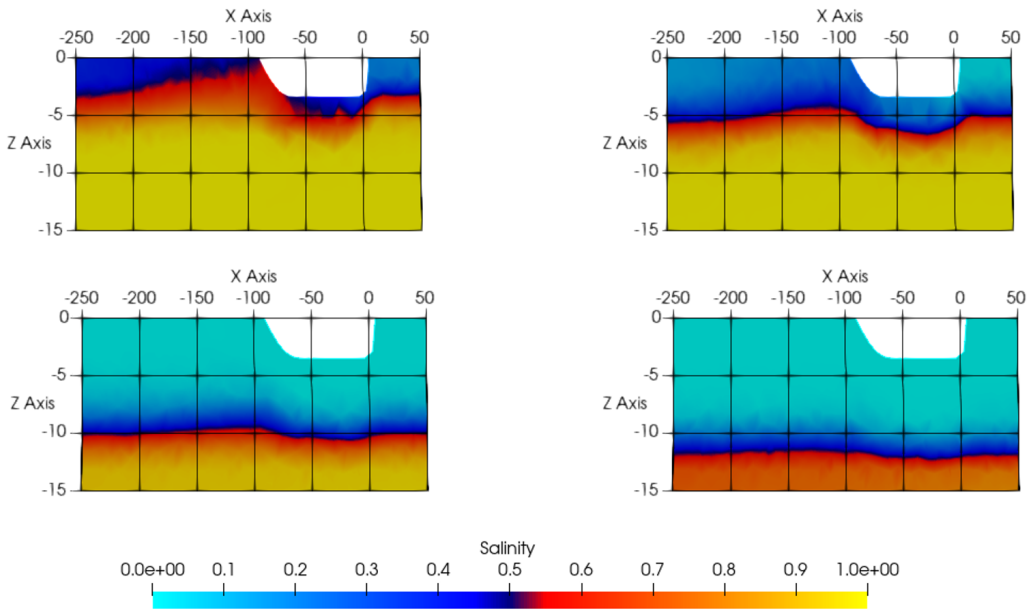

Figure 5.33: Interface deformations for run 25 to 28. The effect on the interface becomes larger if the ship hull is closer to the interface. The z-axis has been scaled with a factor 10.

Return current

The wake is deeper for a smaller top layer as can be seen in Figure F.19. The top layer is almost completely blocked and flows almost completely around the vessel for these runs. Behind the vessel, the streamlines connect and the wake behind the vessel is formed. Also, differences in the shape of the wake can be observed. The wake of run 25 is relatively flat for example, while run 28 shows a half-round wake. The Richardson plots show the most low Richardson numbers in the largest layer, so at the edges of the mixing layer. Other low Richardson numbers are found at the surface and in the wave field halfway the water column.

Interface deformations and internal waves

If the bottom of the ship hull is further away to the interface depth, less effect is visible on the interface as can be seen in Figure 5.33. This was already visible in the runs with a large draught (see Figure 5.11). Figure 5.33 also shows that for small top or bottom layers (run 25 and 28), the thin top or bottom layer already becomes mixed around the vessel. This effect is partly also visible for the runs without a vessel, however, it is stronger for the runs with a vessel. The interface behind run 25 looks unstable. Figure 5.34 shows that run 25 to 28 largely fit in width the pattern of run 1 to 13. Run 25 is an exception as well as the interface squat of run 28.

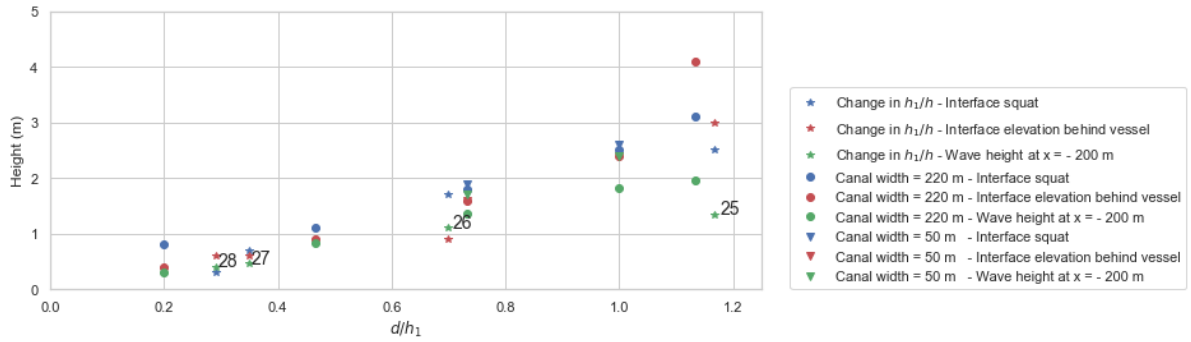

Figure 5.34: Interface motions for run 1 to 13 and 25 to 28. The runs with a changing layer distribution follow the same pattern as the runs with an increase in draught with an exception for run 25 and the interface squat of run 28.

The velocity in y-direction is clearly influenced by the layer distribution as can be seen in Figure F.18. This is the start of the internal wave system behind the vessel. If a layer becomes smaller, the velocities in this layer increase. The wave field of run 28 is not well recognisable, probably due to interaction with the bed. The velocities in z-direction on the interface are from large to low run 26, 25, 27, 28. Although, run 25 has the largest impact on the interface around the vessel, the velocity in z-direction in the wave field is smaller, probably due to influence of the surface. Again, the wave angles come close to the average of the calculated wave angles.

Mixing

The initial PEA of these runs is different, because of the different layer distribution. Run 25 and 28 and run 26 and 27 have a similar initial PEA-value. Figure 5.35 clearly shows the trend that occurs for either a smaller top or bottom layer. For a smaller top layer, the PEA rises around and after the vessel and then goes down in the wave field. For a smaller bottom layer, the PEA around the vessel goes down around the vessel, then comes up slightly, before going down. It should be noted that results at the location of the vessel are not reliable due to the interpolation method. Figure 5.36 shows the difference in PEA for run 26 and 27 and the same run without a vessel. In the wave field, run 25 and 28 decrease the fastest, even though almost no waves are observed for run 28. Small interface motions probably already have a large effect. Run 26 and 27 decrease slower. Run 27 shows a slightly faster decrease due to the larger waves. All runs show a faster decrease compared to run 2. The further the interface is from the middle of the canal, the lower the wave velocity (see Equation 3.6).

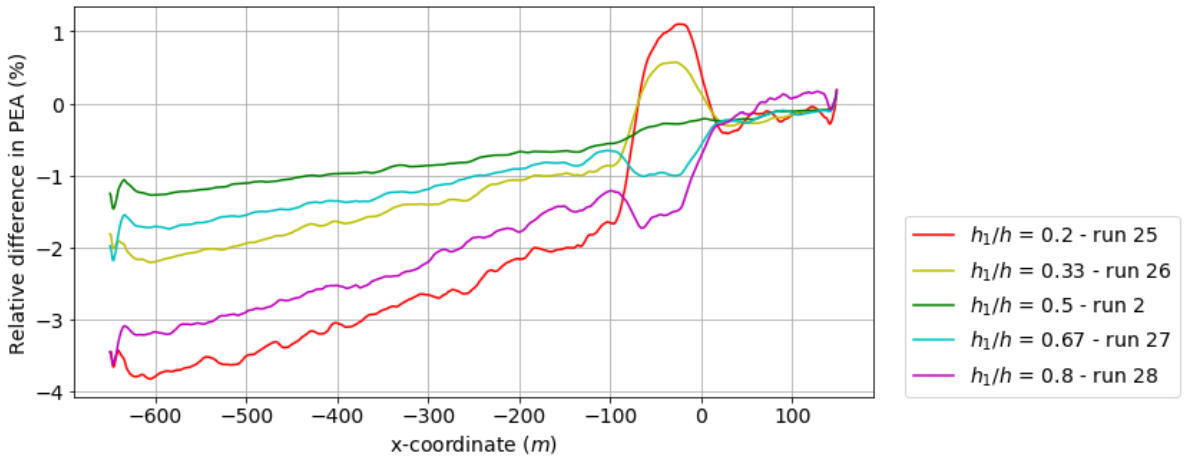

Figure 5.35: Width-averaged PEA relative to a run without a vessel for run 25 to 28. X-coordinate on the horizontal axis corresponds with the distance from the bow.

Figure 5.37 shows the relative density difference for run 25 to 28. For a smaller top layer, the change in density is only visible at the top of the water column, and the other way around for a smaller bottom layer. The effect is larger for a smaller top layer.

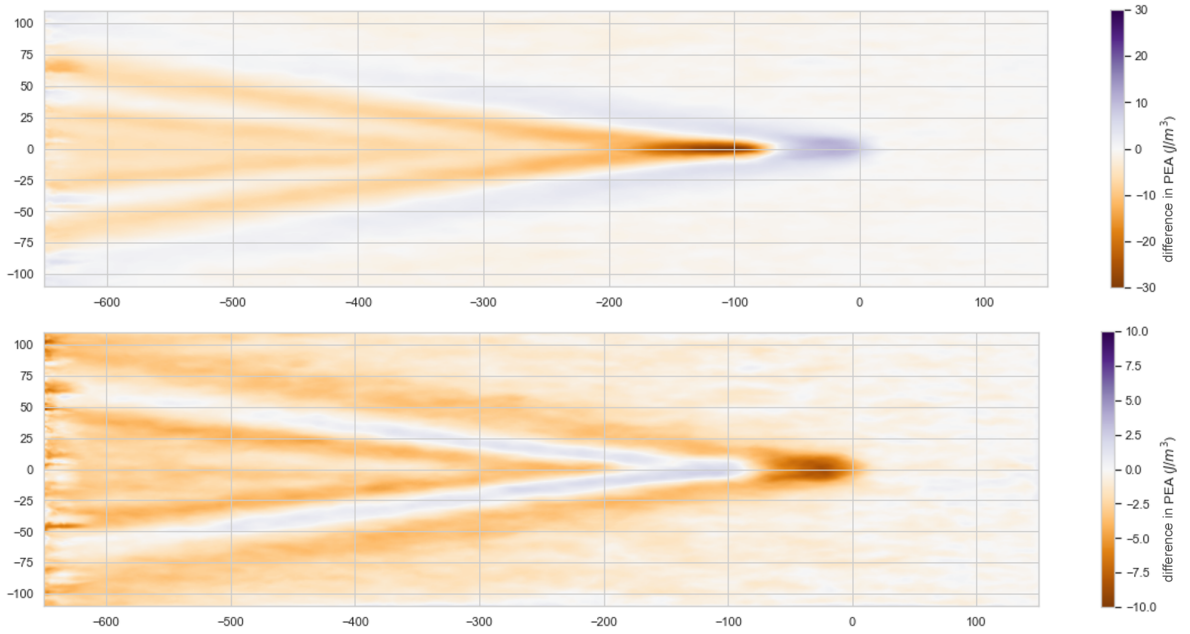

Figure 5.36: The difference in PEA between run 26 (top) and run 27 (bottom) and the same run without a vessel.

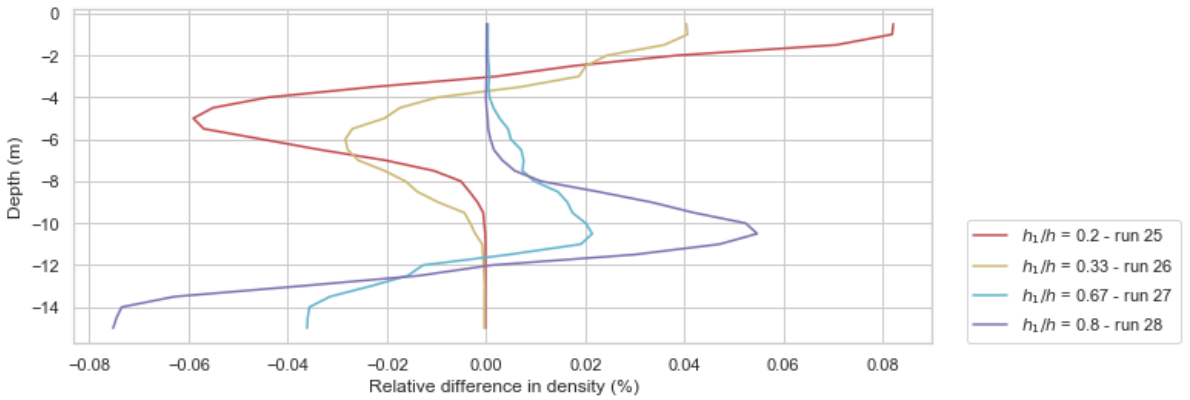

Figure 5.37: If the interface is closer to the surface, the change in density is mainly visible on the surface, and if the interface is closer to the bed of the canal, the change in density is mainly visible at the bed.

5.4.5. Comparison internal Froude number

The wave angle is clearly influenced by the internal Froude number. The average value of the calculated wave angles gave in most cases a close approximation of the angle. For some runs, the waves on the interface are hard to distinguish. This is the case for run 13 (low velocities) and run 28 (small bottom layer). Large Froude numbers can give very small angles of the V-shape. In some cases, the angle is so small that it takes a few hundred meters behind the vessel before the V-shape can be recognised.

The wave height does not seem to be dependent on the internal Froude number. This is different from the expectation. Figure 5.38 shows the squat relative to the interface, the hump behind the vessel relative to the interface, and the wave height at x = - 200 and - 600 m. The interaction of the waves with each other, the sides of the canal and the different wave patterns made it hard to distinguish individual waves, so the values plotted are estimates of the largest waves at the given locations. The differences between the runs is small and no pattern based on the Froude number can be recognised. The squat relative to the interface is for all runs around 1 m, except for the runs where the layer distribution was varied (run 25 to 28). It is larger for the runs with a small top layer, and smaller for a run with a small bottom layer. Run 25 to 28 deviate most from the pattern. The other runs all have wave heights in the same range (0.4 to 1.5 m). Similarly, no pattern is recognised between the internal Froude number and

the decrease in PEA.

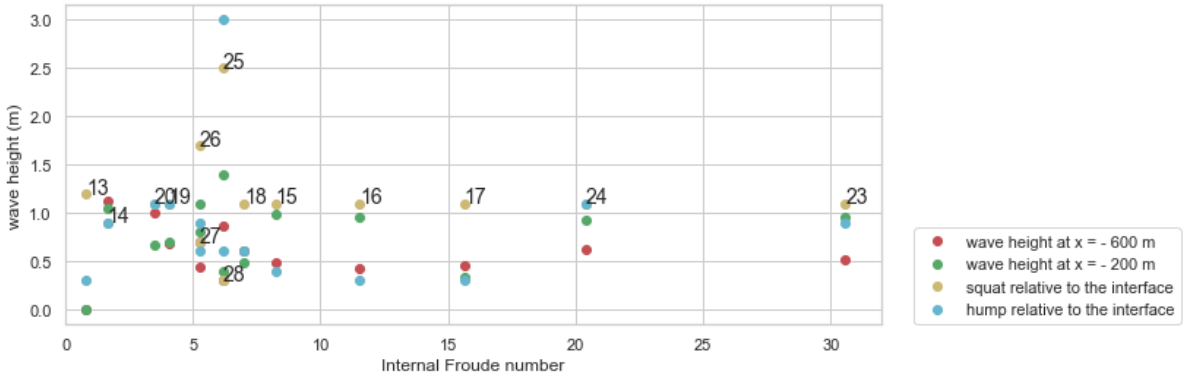

Figure 5.38: The interface motions of run 13 to 24 are in the same range. The internal Froude number is not an indication of wave height, however, the d/h_1 is as can be seen in run 25 to 28.

The individual parameters that determine the internal Froude number proved to be a good indicator of the amount of mixing.

- **Vessel speed**
  It was expected that the higher return current of a higher sailing velocity would lead to more shear, which was confirmed by comparison of run 2, 15, and 16. These runs show that a higher return current gives more mixing around the vessel.

- **Relative density difference**
  A higher density difference was expected to lead to more shear in between the layers. Both run 17 to 20 and run 21 to 24 had changes in the relative density difference. More shear is not visible for the return current directly around the vessel, however, it is visible for the wave field and the wake behind the vessel. A larger density difference gives larger waves, which results in more mixing. The linear runs show more mixing for the same relative density difference.

- **Layer distribution**
  A smaller top layer leads to higher waves, however, at some point the surface disturbance probably dampens the waves. The effect of the rigid lid and possible surface waves on the internal wave system is subject for further study. The interface motions of runs with a change in layer distribution fitted in the pattern found for runs with a changing draught. The closer the ship is to the interface, the larger the waves and the more mixing is generated.

The internal Froude number is helpful in determining the wave angle, however, it is not enough to fully understand the flow pattern and wave field behind the vessel. To do this it is better to look at the vessel speed or density profile individually.

5.5. Slope of the canal banks (run 29 to 36)

The previous runs have been done with a rectangular canal. In run 29 to 36, the canal banks are sloped. The slope has been varied according to Table 5.9, while the width of the canal in the middle of the water column has been kept to 220 m. The canal has been extended to a length of 2000 m, as the waves had not reached the banks of the canal yet at the outflow boundary (x = - 600 m) of run 2. It is expected that ratio of the wave steepness and slope steepness will determine the wave behaviour and resulting mixing.

Run	Canal bank slope
29	1 on 3
30	1 on 4
31	1 on 5
32	1 on 6
33	1 on 7
34	1 on 8
35	1 on 9
36	1 on 10

Table 5.9: Canal bank slopes used for run 29 to 36.

General result

Adding sloped canal banks means that the wave reflection is almost completely removed. The waves refract on the canal banks. The wave field is largely reduced at the outflow boundary, however, some disturbances are still present.

A shallower bank slope means as well that that the top of the water column is wider while the bottom of the water column is narrower. This has an effect on the return current. This is not studied here.

Interface deformations and internal waves

Figure 5.39 shows the interface height of run 32. The waves are not reflected against the side of the canal as they were for the runs with a rectangular cross section. The pattern is largely the same for the other runs with a sloped canal bank. The location where the wave crests meet the sides of the canal is only a little further away for the runs with a shallower slope. After the waves reach the canal banks, the wave crests refract slightly and become more parallel to the shore.

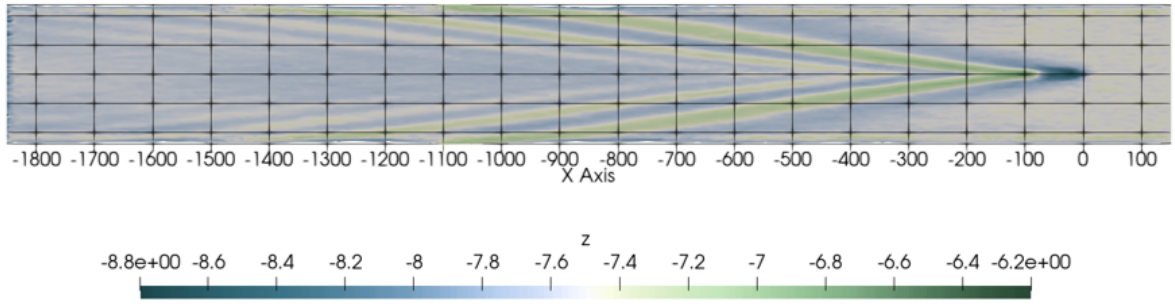

Figure 5.39: Interface height in m for run 32. The other runs with a sloped canal bank show a similar result.

The first wave crests reaches the banks at around x = - 800 m. The wave steepness perpendicular to the bank is at that moment about 0.01. Figure 5.40 shows waves hitting the slope. Run 36 seems to show some wave breaking in this figure, although the number of grid cells needs to be improved to resolve the small scales accurately. The Richardson number shows some low Richardson numbers at the sides of the canal (see Figure F.21). The amount of low Richardson numbers increases for shallower slopes.

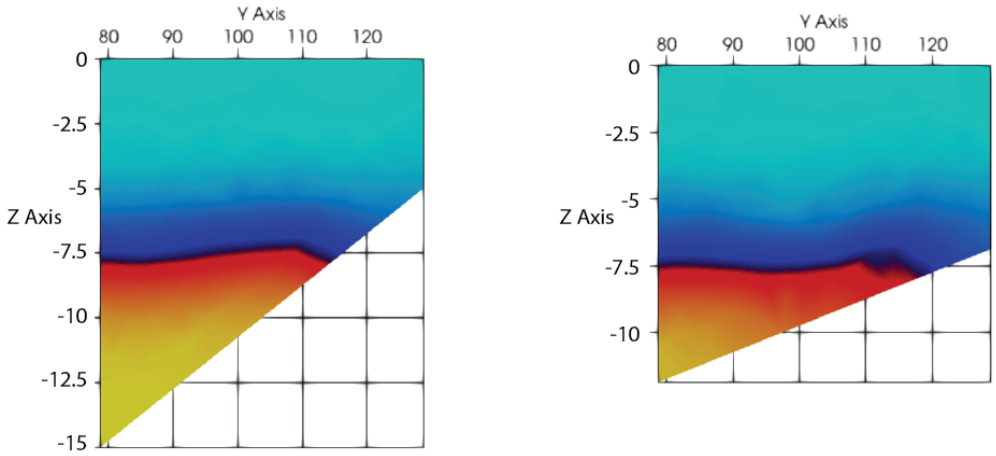

Figure 5.40: Waves on a a sloped canal bank for run 31 and 36. The z-axis has been scaled with a factor 4.

Mixing

No runs without a vessel have been done for the slope variations, however, the width-averaged PEA is influenced by the slope. A canal with a shallower slope has a wider top layer with a low density compared to steeper slopes. Therefore, the PEA has been calculated by removing the value of the PEA at the inflow boundary. The result of this can be seen in Figure 5.42. The width-averaged PEA can be seen in Figure F.20 in the appendix. This shows that the shallower slopes have a lower PEA, which means that the difference in Figure 5.42 is relatively larger. Applying the same method to run 2 shows that the canal bank slope does not have large impact on the decrease of width-averaged PEA for the stretch of canal modelled in run 2 (until x = - 650 m), however, at this location the waves have not reached the canal banks yet. Run 29 and 30 show a somewhat different profile from run 31 to 36. It is most likely an effect of wave reflection as runs 9 to 12 also showed oscillations in the width-averaged PEA due to reflection.

In general, the trend of decreasing width-averaged PEA in the wave field continues in the longer canal. Around x = 1500 m, the lines of the different runs are almost parallel, which indicates that the difference between the runs is negligible and the added influence of the slope is gone. Figure 5.39 also shows that the waves are almost gone at the outflow boundary.

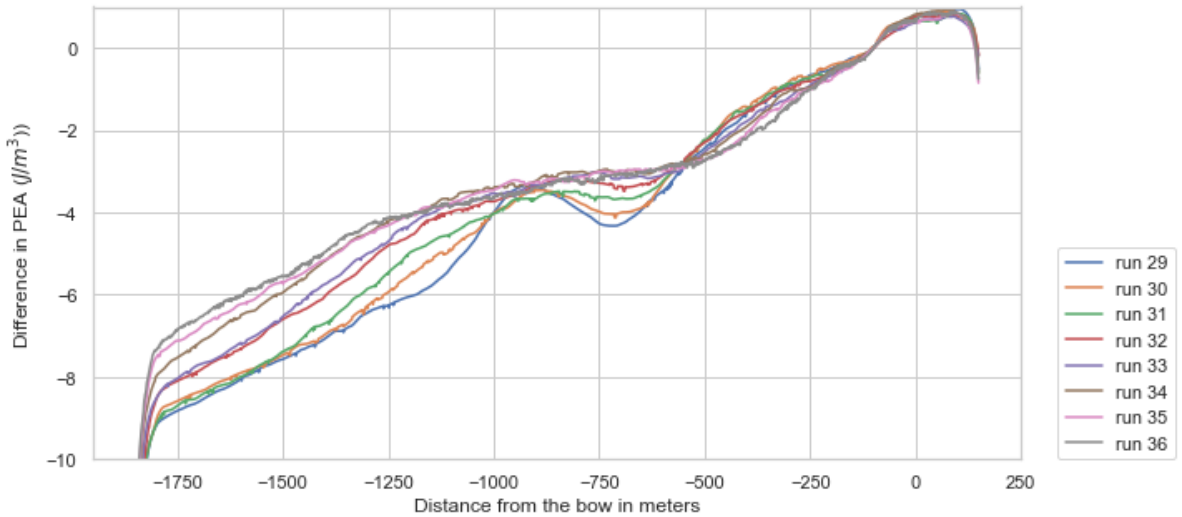

Figure 5.41: The width-averaged PEA compared to the width-averaged PEA at the inflow boundary. Note: the width-averaged PEA is much larger for the shallower slopes (about 90 J/m^3 difference between run 29 and 36).

The width-averaged density profiles show almost the same difference between the in- and outflow boundary for run 29 to 36. The shallower runs show a larger effect in the bottom of the mixing layer. As the canal cross-sections are all 220 m in the middle of the water column, the top layer is wider for the shallower slopes. This means that for the shallower slopes more mixing is needed to show a change in density at the top.

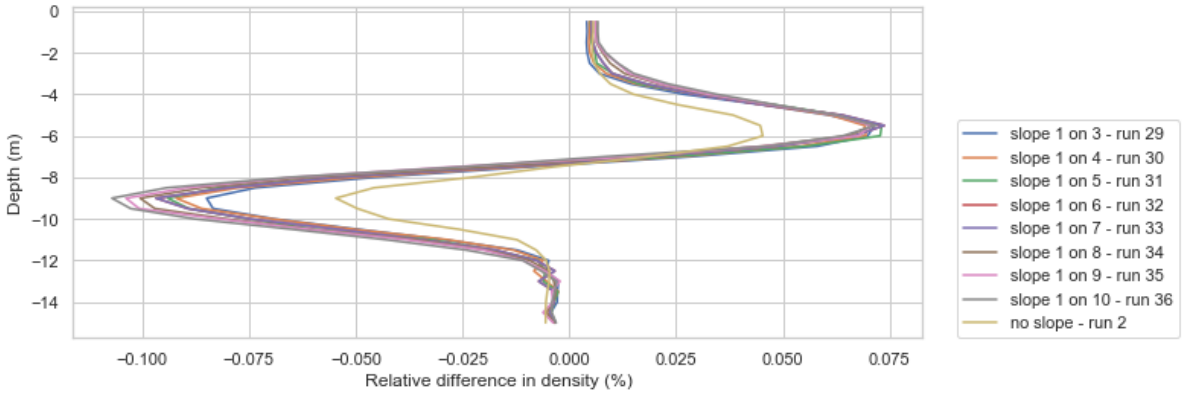

Figure 5.42: The difference in density for run 29 to 36 between the in- and outflow boundary. Run 2 has been plotted as a reference, however, run 2 is 800 m long instead of 2000 m.

These runs do not show a conclusive image of the effect of waves on a sloped canal bank. The slope does largely remove wave reflection, however, a clear effect on mixing is not observed. The changes in density profile seem to suggest that more mixing occurs for shallower slopes.

5.6. Discussion of results

In this section, the overall view after the numerical model runs is discussed. First, the return current is discussed. This is followed by the interface deformations and internal waves. This section ends with a discussion on the observed mixing.

A few runs need improvement or further study. The runs with a large draught need more elements underneath the boat in the mesh. Also, a very small top or bottom layer caused disturbances. The runs with a low vessel speed showed a large decrease in PEA, which was unexpected.

5.6.1. Return current

In general, no large velocity difference at the interface due to the return current is visible. The return current does not concentrate in one layer as was suggested in Chapter 3. Also, an 1D-approximation is likely not helpful as the flow field has been shown to be very three-dimensional.

The return current does generate large velocity gradients at the ship hull and in the wake following the vessel. In the x-direction, the velocity close to the ship hull is in the sailing direction while the flow underneath is accelerated against the sailing direction. Behind the vessel, a wake in the direction of the vessel is formed, which remains present for a long time. This wake is only present in the top part of the flow and is dependent on the draught of the vessel and layer distribution. Higher density differences gave a thicker wake. The wake follows the pattern at the interface. When the interface comes up the wake becomes less deep and when the interface moves down, the wake becomes deeper.

The velocity shear is in most parts of the model not large enough to create low Richardson numbers. Most low Richardson numbers were found at locations with a very small density gradient. Low Richardson numbers due to the return current were found at locations with large velocity gradients, such as at the ship hull and in the wake. These values were found at the top and bottom of the water column. The low Richardson numbers were found to correspond with a decrease in PEA at that location.

The canal blockage and the vessel speed have the largest influence on the return current. A higher canal blockage means that more water is moved by the vessel resulting in a higher return current. A higher vessel speed means that the same amount of water is moved at a higher speed. The higher return current results in more shear instabilities and more mixing.

5.6.2. Interface deformations and internal waves

As expected, the vessel deformed the interface underneath the vessel and created internal waves behind the vessel. This is very similar to the pattern on the surface, except that the internal waves showed a supercritical wave pattern, where that would have not been the case for the surface waves. Wave reflection and dispersion of the waves made it in some cases hard to accurately read wave characteristics.

The interface deformation shows a consistent image for all runs. The minimum and maximum change in interface height is about equal in most cases. The interface is forced underneath and around the vessel. The lowest point is close to the bow of the vessel and the interface starts to rise from that point. At the stern, this hump steepens before it splits into two waves forming a V. The interface squat is visible until a d/h_1 of 1.1. For larger draughts, the top layer flows around the vessel, no interface squat is visible, and the hump is connected to the ship hull. It was suggested that the canal blockage is not a good parameter to predict the interface deformations, and that d/h_1 is a better predictor of interface motions by comparing data from a smaller canal. The d/h_1 was also found to be a good predictor for the runs with a change in layer distribution. For changes in internal Froude number, the pattern changed as well. The minimum and maximum interface deformation were at the same location, however, the slope underneath the vessel changed. The sailing speed had the most influence on this.

The wave angle can be estimated by taking the average of the formulas given in Section 3.4. The wave crests are initially narrow and high, while the trough is long and flat. Further away from the vessel, the wave height decreases. The wave height seems to be mostly influenced by how far the vessel is from the interface. The waves become less steep after reflection at the canal banks. A sloped canal bank removed the wave reflection almost completely.

The internal waves contribute to mixing via two processes: shear instabilities in the wave field and wave breaking at sloped canal banks.

5.6.3. Mixing

Figure 5.43 summarises the width-averaged PEA plots for all the runs above (with runs 29 to 36 as exceptions). The contribution of the return current and the internal wave is also given. These values are estimates as sometimes wiggles made it hard to determine an exact value. The PEA decreases and increases quickly directly behind the vessel for run 6 to 8. For these runs, the contribution of the return current has been estimated as the value after the increase. The patterns in this figure are discussed below. Run 29 to 36 are not included in this graph as no run without a vessel has been done for these runs. The influence of the slope on mixing is not very clear from these runs. A shallower slope seems to contribute to more mixing.

In the reference run, both the wave field as the return current cause a 1 J/m^3 decrease of the PEA (about 1.2% of the initial PEA). The PEA at the location of the vessel might be distorted by the interpolation method, however, the width-averaged PEA before and after the vessel shows a relatively large decrease. This means that the processes around the vessel cause mixing. The decrease of PEA in the wave field occurs in a slower rate, but over a longer distance.

A larger draught and canal blockage causes a larger decrease in PEA and therefore more mixing. This is due to both a larger contribution of the return current as the internal waves. The smaller canal of run 9 to 12 has a lot of reflection in the wave field and this also visible in the PEA plot. For these runs, it was therefore not possible to find the contribution of the internal waves and the value has been set to 0. The vessel speed influences the decrease in PEA less. For a larger speed, the decrease becomes slightly larger (only run 15 and 16 are included here). A larger relative density difference has a larger decrease in PEA. The biggest contribution to this difference is the wave field. This is visible for both the tanh-profile as the linear profile with a slightly higher decrease of PEA for the linear profile. Moving the interface away from the middle of the water column results in more mixing. If this means that the vessel is closer to the interface as well, the mixing is even more. This is due to both contributions of the return current as the internal wave field.

Most runs have a relative decrease of the PEA between the 1 to 2 %. The runs with a change in d/h_1 show much larger values, up till 4 or 9% decrease. The maximum value of 9% was found for the canal of 50 m wide. The PEA showed a lot of wiggles, so the effect on mixing is not very clear for this run. Moreover, the mesh size was relatively bad for this run. A maximum value of 4% seems to be a safer assumption.

The complete effect of the internal wave field is not visible as the waves are still present on the

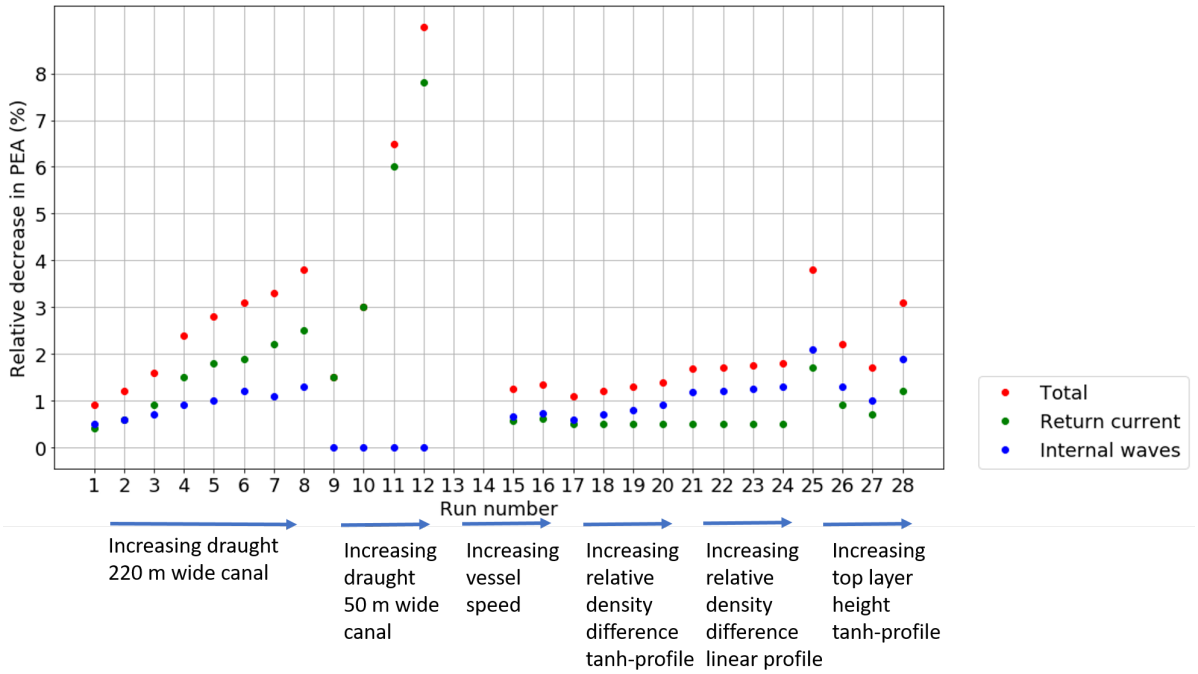

Figure 5.43: Percentage relative decrease in width-averaged PEA for the runs with a vessel compared to without a vessel with the contribution of the return current and the internal waves.

interface. The longer canal in run 29 to 36 showed that the wave field remains present for a long time and continues to contribute to mixing. The values found for the decrease in PEA can therefore be seen as a minimum value. The longer canal has a twice as long distance behind the vessel. In this canal, the waves are almost gone at the outflow boundary. The contribution of the internal wave field might be up to twice as large as compared to the shorter canal, as all the wave energy will have to dissipate at some point and a part of this wave energy will contribute to mixing. The contribution of internal waves to mixing will decrease with distance from the vessel as the internal waves become smaller as well, so the maximum value might also be smaller. This needs further study.

The decrease in PEA generally means that the top and bottom value of the width-averaged density move closer to each other and the mixing layer becomes steeper as can be seen in the density plots. Due to bottom friction and disturbance at the top, the linear profile slightly moved to a tanh-profile for both the run with and without a vessel. The top and bottom density move closer to each other, while the mixing layer becomes less steep. For the layer distribution, the change in density profile is only visible at the top or bottom respective of where the smaller layer is. Both the series with a linear as with a changing layer height show already a relatively large change in density for the run without a vessel. The vessel amplifies this effect.

The changes in the width-averaged density profile are almost symmetric for the top and bottom layer (with the exception of the runs with a different layer distribution). The shift in the mixing layer is a little stronger for the bottom layer, while the density at the top of the water column increases more than the density at the bottom of the water column decreases. The runs with a change in layer distribution show a larger effect for the runs with a small top layer respective to a small bottom layer. Low Richardson number can indicate shear instabilities and are observed around the vessel, in the wake and in the wave field. The low Richardson number were mostly found in locations with very small density gradients. The gradient in velocity is in other locations not strong enough to create shear. In runs with more low Richardson numbers, the PEA decreases faster, which confirms that shear instabilities due to the return current and internal waves contribute to mixing.

5.7. Conclusion

The following can be concluded about the contribution of the different mixing mechanisms to mixing.

- **Return current**
  The return current contributes to mixing by shear instabilities at the ship hull and canal bed directly around the vessel and in the wake following the vessel. The return current is mostly influenced by the canal blockage and vessel speed. The density profile and resulting interface deformations around the vessel have some influence on the shape of the wake following the vessel. The decrease in width-averaged PEA due to the return current (not including the wake) is in the range of 0.4 to 7.8 % for the runs done with an average value of 1.5 %. The largest values occur for the large canal blockages. A small layer thickness also gives relatively much mixing due to the return current.

- **Internal waves**
  The internal waves contribute to mixing by shear instabilities in the wave field and wave breaking on the canal banks. The distance of the ship hull to the interface (d/h_1), density profile (ρ_1/ρ_2, linear), and slope of the canal bank have the largest impact on the wave field. The decrease in width averaged PEA is in the range of 0 to 2 %. It varies the most for the runs with a different density distribution, especially for the linear runs and the runs with a change in layer-distribution for a two layer-flow. As the wave field was still present at the outflow boundary, the total decrease of PEA per vessel will be higher. The percentages given can be seen as minimum values with double the value as a maximum.

- **Propeller jet**
  The propeller jet is not studied in the numerical runs. The hump behind the vessel and the low PEA at the location of the propeller seen in the model results indicate that the propeller jet could have a large contribution to mixing. This will be further discussed in the next chapter.

6

Discussion

A comparison of processes and parameters found in Chapter 3 with the model results has already been made in the previous chapter. In this section, the results and limitations of this study are discussed. First, the limitations of the numerical study and the choices made therein are discussed. This is followed by a discussion of the observed mixing in the numerical study. Next, an estimation of mixing in a typical Dutch inland waterway is made based on the results of the numerical study. Steps to be taken to include ship-induced mixing in numerical models are shortly discussed as well.

6.1. Numerical model set up

Several choices have been made in the set up of the numerical model, which influence the results. The most important limitations are discussed below. The model results confirm that a 3D approach is necessary to accurately study the problem.

6.1.1. Mesh quality

As discussed in Section 4.2.1, the amount of tetrahedra that could be used was limited due to convergence problems. The meshes used are all very unstructured and in some cases more elements over depth are needed, such as for example for the runs with a large draught. More elements over depth are needed to resolve the small scales that are currently not visible in the model. Shear instabilities or breaking internal waves have not been observed. Furthermore, although the numerical diffusion is low, even the runs without a vessel show a change in density profile. A different mesh generator or a smarter mesh design could have limited these issues. However, for this study the mesh quality is acceptable. The most important processes are visible and numerical diffusion is relatively low (in the order of 1 percent).

6.1.2. Model parameters

In Chapter 4, the choices for the model parameters have been explained. The most important implications of these choices are discussed here.

Based on data of the NZK and AKP, a vessel similar to a Va vessel has been used as reference case and for most runs as this was the most frequently occurring vessel. This is a relatively small ship, especially for the NZK. A larger vessel would have given more effect as was shown with the runs with a larger draught. To study the effect of the horizontal canal blockage, the width of the canal has been reduced. It would have been better however, to increase the width of the vessel, as this would have resulted in a more realistic result and less wave reflection.

All runs have been done using a rigid lid approximation as the interest was solely in the internal effects. This might have an influence, however, the effect is expected to be small. The roughness coefficient used is the same for the ship as the bed of the canal. This is good enough to show the general pattern, however, for choosing two different roughness coefficients would make the result more accurate.

The concepts discussed in Chapter 3 are mostly based on two-layer flow. A tanh-profile has been applied to approximate this. The mixing layer of this profile is relatively large. Setting a thinner mixing

layer meant a lot more numerical diffusion, which resulted in a similar density profile at the outflow as is now set at the inflow boundary. The two-layer model approximation is not valid because of the thick mixing layer. It might be better to use three-layer theory of Fructus and Grue (2004) as was suggested by Medjdoub et al. (2020). The linear density profile was also not a fully linear profile. The density profile shifted to a tanh-profile with a very large mixing layer, even for runs without a vessel, due to influences from the top and the bed of the canal.

Furthermore, the range of parameters tested is incomplete. Many other factors might influence mixing by ship traffic, such as the eccentricity of the boat in the canal, the length of the boat, discharge in the canal. It is expected that the studied parameters already give a good view of the most important aspects of mixing by ship traffic.

The used approach is good enough to get a first impression of the order of magnitude of effect and to get insight in the relevant processes and parameters.

6.2. Mixing

In the previous chapter, the results of the numerical runs have been discussed. This section looks at the approach that was used to quantify the amount of mixing, the method used to analyse the return current and internal waves, and the additional effect that the propeller could have on the mixing of salinity.

6.2.1. Quantifying mixing

The PEA has been used as an indication of the amount of mixing in the flow. It is a good indicator of changes in the density profile, and using a width-averaged value gives a good overview of the general effect. However, the PEA-plots of some runs also showed at some locations increase in PEA and the effect of the vessel was still present at the outflow boundary. Furthermore, the decrease in PEA has been standardised following the formula given in Section 4.3. It might have been better to use a constant value instead of a value changing over the length of the canal, however, this is dependent on the application.

The model showed low numerical mixing. The reference run without a vessel (and thus no velocities) showed about 1.7 % decrease in PEA over the length of the canal relative to its start state at the inflow boundary. The reference case showed an additional 1.2 % decrease in PEA. This is also visible for the other runs without a vessel, so the effects are of the same order of magnitude. This makes the interpretation of runs without a run without a vessel (the runs with a slope) hard.

The Richardson number has been used as an indicator for shear instabilities. The velocity gradients in the model are very low which gives very large Richardson numbers. The Richardson number is actually not meant for these kind of low velocity gradients. It has however been an good indicator of mixing and shear instabilities. It also showed the patterns in the return current, wake and wave field clearly.

The combination of shear instabilities and internal waves do suggest that ship traffic is contributing to mixing. It shows the complexity of modelling density-driven flow around a vessel. The method used already has low numerical diffusion compared to other methods. A better quality mesh would probably improve the runs considerably.

6.2.2. Return current

The return current contributes to mixing of the waterway. In Chapter 3, it was suggested that shear would occur due to the concentration of the return current in one layer. This is not the case. However, the increased velocities at the bed and ship hull contribute to mixing. The width-averaged PEA shows a drop at the bow and at the stern, even for the runs where the PEA increases at the location of the vessel. This increase is likely due to the interpolation method. The method used distorts the data at the location of the vessel hull. Only the values before and after the vessel can therefore be used.

The wake following the vessel is also part of the return current. The location of the wake shows low Richardson numbers, but it is not possible to see the effect of the wake separately from the effect of the wave field in the width-averaged PEA plots. The PEA plots showing the entire model domain do not show the wake clearly. Furthermore, in reality, the wake would have a completely different profile due to the propeller jet. The contribution of the wake is therefore likely to be small.

6.2.3. Internal waves

Mixing by the internal waves seems to stem from shear instabilities in the wave field. The waves are still present at the outflow boundary, so the total effect of the wave field is not visible. They are likely to contribute more than the return current, as their contribution to the decrease of PEA was now about equal for a large number of runs (see Figure 5.43). Based on the data from a longer canal, a maximum contribution of the internal wave field of twice as large as currently modelled is given. This is not a very reliable estimate, as the runs in a longer canal have been done in different canal geometry with sloped canal banks. In a rectangular cross-section, the interaction of the internal waves with the canal banks will be different and it is unknown how long the waves will stay present in such a canal. Furthermore, the results with a slope are hard to interpret since no run without a vessel has been done for these meshes. No large differences are visible between these runs. A shallower slope seems to contribute to more mixing, however, the effect is small. The wave reflection in some runs gives a lot of wiggles in the width-averaged PEA plots. This makes it hard to see the effect of the wave field on mixing.

6.2.4. Possible influence of propeller

The propeller has not been added to the model to simplify the numerical model, and because it was expected to play a local and small effect, especially for ships sailing with constant speed in a straight line. However, the numerical model results suggest that the propeller might have an important role, as the interface is heightened and the PEA low at the location of the propeller, making it easy to have a large impact on mixing.

This requires further research, because the interface rises at the stern of the vessel. For most runs, this meant an elevation of 0.5 to 1 m with a maximum of 3 m relative to the interface. This means that the propeller would be very close to the interface if it was not already. Esmaeilpour et al. (2016) already showed for a submarine that the location of the propeller with respect to the interface is important for the response of the interface. How the propeller would deform or influence the hump is unclear. It also not known how much mixing this would generate.

The runs done show a wake in the direction of the vessel. In the discussion of the results some differences in this wake were observed. For the reference case, the wake had a velocity of about 1.2 m/s. Adding a propeller to the vessel would change the flow in the wake completely. Figure 2.11 gives an impression of the changes that would occur for the flow field. More research is needed to find the effect of the propeller on mixing the canal. Below, a quick estimation based on velocity shear is given.

Estimates of the propeller velocity in Chapter 3 give efflux velocities of 2 to 6 m/s. This efflux velocity decreases along the axis and perpendicular to the axis following the formulas given in Section 3.5.1. At 5 m along the axis from the propeller and 1 m down, an original efflux velocity of 4 m/s is for example decreased to 1.4 m/s and another meter down to 0.8 m/s. If it is assumed that the propeller velocities concentrate in the top layer and the bottom layer is non-moving, an estimation can be made how much the velocity shear could mix the density distribution. Equation 3.4 gives that for a velocity difference in a 15 m deep two-layer flow with a velocity difference between the layers of 0.5, 1 or 1.5 m/s, a density difference of 1.7, 6.8 or 13 kg/m^3 could be mixed over the vertical. A time-component is to mix the flow completely over the vertical is not included in this equation, so the mixing will likely not develop completely and less mixing will therefore be realised. This quick estimation shows that the propeller could significantly contribute to mixing of salinity. The propeller velocity decreases however quickly with distance from the outflow and its ability to contribute to mixing decreases with it.

As the propeller velocities have the same order of magnitude as the return current, it is expected that the contribution of the propeller to mixing will be about equal to the return current. An important difference between the two is that the propeller jet is a forced jet from a local source, while the return current slowly builds up due to pressure differences in the flow.

6.3. Estimated mixing in canals

Estimations show around 1 to 4 percent decrease in width-averaged PEA from one ship in 600 m of canal (with two outliers of 6.5 and 9% for very large canal blockages). The width-averaged density difference plots show changes in the order of $\mathcal{O}(10^{-2})$ percent. As the difference in density in a typical canal is low, about 1 percent, this is a relatively large change for one vessel.

In reality, ships sail all-day through the canals, and will create a cumulative effect. How exactly the contribution of one vessel can be combined to the effect of multiple vessels is not studied. Below,

a few quick estimations of what it could mean for the Noordzeekanaal, Amsterdam-Rijnkanaal, and Antwerps Kanaalpand are given. Other mixing terms such as bottom roughness and wind are not taken into account here.

6.3.1. Noordzeekanaal

The Noordzeekanaal and Amsterdam Rijnkanaal described in Section 3.1.1. At IJmuiden, the top layer of the NZK is well-mixed over the vertical, while the salt wedge at the bottom has an almost linear profile. In the numerical model results, the change in density profile over the length of the canal was largest at the top of the canal. The well-mixed top layer of the NZK might partly be due to the ship traffic. Verbruggen and Baan (2020) showed that numerical models result in a more linear profile as opposed to the measured profiles (see Figure A.3). The difference between the model results and measured values might be due to the lack of a mixing by ship traffic term in the numerical model. Figure 6.1 sketches how the density profile could change from a linear profile to a typical NZK-profile if ship traffic is contributing mostly at the top of the water column.

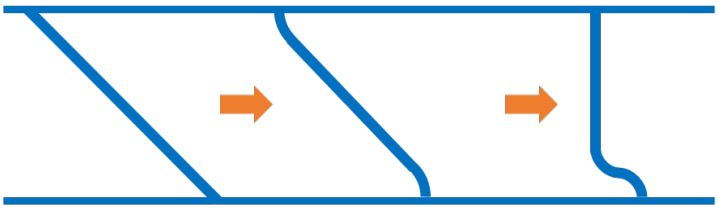

Figure 6.1: Possible change of density distribution from a linear profile to a more trapped density profile as was seen in the linear runs. If ship traffic has a larger impact on the top layer, this might contribute to a vertically mixed profile at the top of the water column, while the bottom still shows a gradient.

This idea is applied to the width-averaged changes in density profile of the numerical run. The results of run 23 (linear profile, R0 = 0.01) are used, as the NZK has a typical density difference over the depth of 10 kg/m^3. Figure 6.2 shows the result if the same change is applied five times to the density profile, corresponding to five ships sailing over the canal. This gives an unrealistic density profile. The actual density profile might look some more like the dashed line.

A few things have not been taken into account in this estimation. The run used has a rectangular profile instead of sloped canal banks as the NZK. This would mean some extra mixing is generated in reality. As the density difference becomes smaller, the amount of mixing per vessel becomes less as well. Furthermore, the linear density profile transitions to a trapped profile. Figure 6.2 shows what happens if the change in density profile is repeated for run 2 (tanh-profile, R0 = 0.01). The actual change in density profile after 5 ships will lay somewhere in the middle of these results.

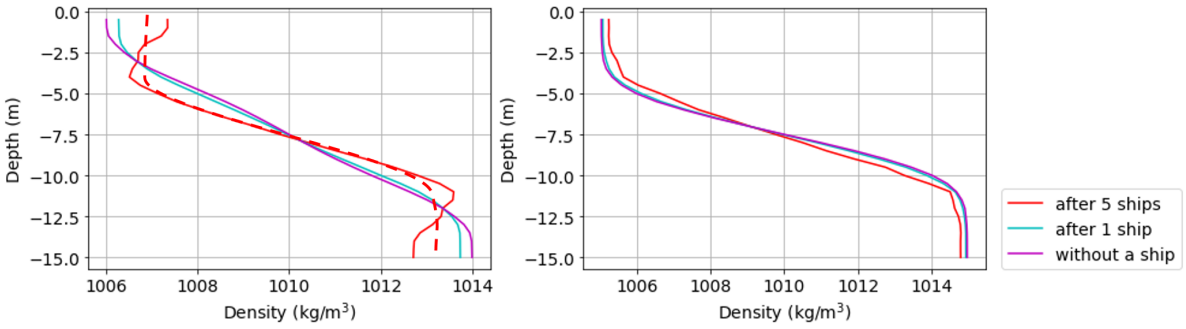

Figure 6.2: Observed changes in the density profile without a vessel, after one vessel (numerical model result), and after 5 vessels (extrapolated from the model results) for run 23 (left) and run 2 (right). The profile on the left is unrealistic. The dashed line shows how the resulting density profile might look after 5 vessels since the extrapolated result is unrealistic.

The top layer becomes more well-mixed, but the effect is not as extreme as sketched in Figure 6.1. The combination of more ships and the addition of fresh water discharge might lead to a larger top layer as sketched above. The combination of these effects is not yet clear. Furthermore, only results

with a ship with small draught have been used. Figure 5.15 suggests that for a larger vessel the effect becomes larger in the top layer than in the bottom layer.

6.3.2. Amsterdam-Rijnkanaal

A quick estimation of mixing by ship traffic around Diemen is given as well. Hydrologic (2020) studied peaks in chloride-levels in the Amsterdam Rijnkanaal at Diemen. They found a decrease in ship traffic over the weekends overlapping with peaks in the measurements of chloride. The chloride peaks were found to occur more often on Sundays and Mondays. Most of the peaks occurred for a short time frame of a few hours, however, peaks longer than 12 or 24 hours are also observed. Peaks were defined as measurements of 200 to 500 mg Cl/L. A maximum value of 550 mg Cl/L was found for the top sensor and of 3200 mg Cl/L for the bottom sensor, however most recorded peaks were lower. On Sundays, the density differences were found to be the largest with a median difference between the sensors of 1250 mg Cl/L. Based on the data of Hydrologic (2020), the ship traffic intensity is estimated at 4.6 ship/hour on Sundays. During the week, about 7 ships an hour pass by. This is a decrease of on average 2.4 ship/hour in the weekend.

The median difference of 1250 mg Cl/L corresponds to a density difference of 1.7 kg/m^3. The numerical runs showed a relative decrease in PEA of about 1.1% for a tanh-profile and 1.7% for a linear profile with a density difference of 1 kg/m^3. Assuming that the PEA decreases exponentially, this would give 47 to 62 % increase of stratification in 24 hours and 72 to 86 % increase of stratification in 48 hours during the weekend due to the lower ship traffic intensities using the -2.4 ships/hour. The average ship traffic intensity of 7 ships/hour during the week would decrease the PEA with 84 to 94 % in 24 hours and would be able to almost completely mix the canal over the vertical.

These are very rough estimations based on width-averaged data. The amount of mixing is likely to be higher due to propeller mixing. This does not take into account that most peaks occurred for short time frames. High variability of ship traffic might play a role here, however, this level of detail is not available.

6.3.3. Antwerps Kanaalpand

The Antwerps Kanaalpand is described in Section 3.1.2. Most of the year, the AKP is well-mixed over the vertical, even though both ends of the AKP have very different densities. As the canal cross-section is smaller than in the test runs and the depth lower, the ships are likely to have a larger impact. Figure 6.3 shows how the density profile could change from a two-layer profile due to the different densities at the canal boundaries to a vertically well-mixed state. The figure on the right in Figure 6.2 illustrates this for a tanh-profile using the numerical model results.

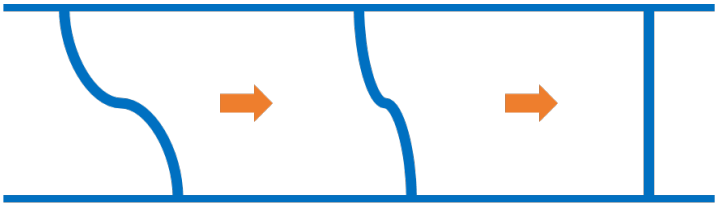

Figure 6.3: Possible change of density distribution to a fully-mixed state. As was seen in the runs, ship traffic results in a decrease of the density at the top and bottom of the water column. If the effect of enough ships is added, a vertically mixed profile is found.

In Section 3.2.1, the effect of the lack of ship traffic in the canal due the blockage of the Eendracht on salinity measurements in the AKP are described. In about 12 hours the difference in chloride measured went up by 600 to 800 mg Cl/L, corresponding to a density difference of 1 kg/m^3. The ship traffic on the AKP is estimated to be about 7.6 ships per hour, so under normal circumstances on average about 90 ships would have passed the AKP during the time period of the blockage. Based on the decrease of PEA of 1.1% for a tanh-profile and 1.7% for a linear profile with the same density difference for the numerical runs and the assumption that the decrease of PEA develops exponentially for multiple ships, 64% to 79% of PEA-decrease would normally have been added by ship-mixing in this time period of 12 hours. The lack of ship traffic might therefore explain the peak in difference in salinity measurements. This is likely to be higher due to the added mixing of the propeller. Furthermore, the decrease in PEA is likely higher due to the smaller canal geometry compared to the model runs. The relative draught of

vessels is likely to be higher than in the numerical simulations resulting in a larger decrease of PEA.

These estimations suggest that ship-induced mixing is indeed likely to play an important role in canals, however, they are based on small mixing factors for one vessel that are extrapolated to the effect of multiple vessels.

6.4. Including ship-induced mixing in numerical models

This study has focused on the basics of mixing by ship traffic in canals, and contributes to a better understanding of the physical processes and parameters that play a role. Additional work is needed before ship-generated mixing can be included in large-scale numerical models. Several steps need to be made before ship-induced mixing can be included in large-scale numerical models. This study gives insight in the most important parameters, however, more research is needed to completely describe the flow around a ship in a stratified canal and the mixing this causes. This could lead to a parameterisation where based on certain parameters the amount of mixing could be established. The changes that have been observed in the density profiles and the PEA could be translated to a diffusivity. Some thoughts on what would be important are given below, however, this is not a complete list.

The way that mixing would be best included in a numerical model would be based on a few factors. The first factor is the type of model that is used and the requirements on the model. It is always a balance of detail needed and computation power. For an 1D-model, details of ship-induced mixing might be less important and could be taken into account in a general mixing term. For a 2DV-model, ship traffic would be more important and could be introduced in several ways, for example by a source term or a larger background viscosity. Maderich et al. (2008) added a ship-component to the vertical eddy- and diffusion coefficients. As the effect was slightly larger for the top layer, the mixing should mimic this as well. For a 3D-model, the vertical resolution used in the model would be an important parameter to decide how detailed mixing by ship traffic should be included.

The second factor is the type of canal. A more traffic intense canal might need a different approach than a canal with few ship traffic. Also, the variety of ships and ship characteristics is important. Furthermore, as ship traffic shows a time-dependent pattern (as shown by Hydrologic (2020)), the aim of the model calculations is important. Is the goal to model a single ship along its path or is the goal to mimic the average effect of shipping? It might also be important to take into account a weekday/weekend-pattern when modelling changes in a certain month. However, for other situations such detail might be superfluous. This might lead to for example a variable function or stochastic function that mimics the variability in ship traffic or a time-averaged term that continuously adds mixing to the model.

7

Conclusion and recommendations

In this chapter, the conclusion to the research questions is given and recommendations for further research are made.

Chapter 2 showed that there is currently little known about mixing by ship traffic in canals. The most recent study with the same goal that was found was Moser (1985) and Moser and Bakker (1989). In the mean time, knowledge on ship-generated internal waves has improved considerably for example by work of Yeung and Nguyen (1999) and Chang et al. (2006). These studies are, however, not focused on inland waterways or mixing.

Throughout the report clues have been found that mixing by ship traffic plays an important role in canals. A rough data analysis of the time period of a blockage of the Schelde-Rijnkanaal showed that the amount of stratification increased during the blockage. Also, a slight weekend effect with more stratification during the weekend was visible. This weekend effect has also been observed by Hydrologic (2020) in their study into salinity peaks in the Amsterdam-Rijnkanaal. These analyses did not show whether this decrease in mixing is due to a decrease in mixing by ships or a decrease in lock operations. In Section 3.2.2, a rough estimation following Karelse and Van Gils (1991) showed that ship traffic might be more important than wind or bottom shear, however this was rough estimation based on propeller power. As these clues indicate that ship traffic might contribute significantly to mixing in a canal, this study aimed to improve the knowledge on this field.

This study set out to answer the following research questions:

To which account is ship traffic responsible for the vertical mixing in a stratified canal, and to which processes can this be attributed?

- What are the governing parameters in these processes, and how do these parameters influence vertical mixing and transport?
- How significant is the effect of shipping traffic on mixing and transport of salinity in relation to other mixing and transport terms?
- Which steps need to be taken to include the mixing and transport of salinity caused by ship traffic in weakly-dynamical inland waterways in 2DV- and 3D numerical models?

7.1. Conclusion research questions

The effect of ship traffic on mixing in a stratified canal has been studied by means of a literature study, a data analysis on the Antwerps Kanaalpand, Noordzeekanaal and Amsterdam-Rijnkanaal and set of numerical runs in FinLab, a 3D non-hydrostatic finite element model. The return current, internal waves, and the propeller jet are identified as possible mixing processes based on previous studies. Several relevant parameters in these processes have been identified and tested in a numerical model. In Chapter 6, a first approximation to what this might mean in a canal with multiple ships has been given. The conclusions with respect to the research questions are given below.

- **To what extent is ship traffic responsible for the vertical mixing in a stratified canal, and to which processes can this be attributed?**
  The vessel has been found to contribute to mixing in a canal. The numerical runs showed a decrease of about 1 to 2% in width-averaged PEA over 600 m length of the canal after one vessel passage for a representative range of parameters of canal geometry, density profile, vessel draught and vessel speed. Runs in a two-layer flow with a large draught to top layer height, d/h_1, showed a decrease of up to 4 %. A slightly larger effect for the density at the top of the water column as compared to the bottom of the water column was observed.

  The numerical model showed the effect of one vessel on the stratification. In reality, many ships are affecting the density distribution (six ships an hour on average for the studied canals). The integrated effect of multiple ships was not investigated, however, a first estimate has been given in Section 6.3, which shows that the integrated effect might have a large impact on the density distribution of the Antwerps Kanaalpand, Amsterdam Rijnkanaal, and Noordzeekanaal.

  Three possible contributing processes have been identified. The return current and the internal waves have been shown to play role in mixing, and the propeller jet is likely to contribute as well. The internal wave field seems to show the largest contribution to mixing, as its influence is over a long reach of canal. The total effect of the internal waves was not visible in this study as the domain was too short. The runs with a longer canal and sloped canal banks showed that the internal wave field continues to contribute to mixing for about double the distance modelled in the runs with a shorter canal. The return current does have a large contribution over a short stretch of canal.

  - *Return current*
    The return current does not concentrate in one layer, and therefore does not create shear in between the layers as was suggested in Chapter 3. The increased velocities of the return current cause shear at the ship hull and at the bed which contributes to mixing. Behind the vessel a wake with high velocities in the direction of the vessel is formed. This wake also creates large velocity gradients. The return current contributes to about 0.4 to 3% decrease in PEA around the vessel. A few higher values for larger canal blockages, however, for these runs the number of grid cells underneath the vessel was too low.
  - *Internal waves*
    Under most circumstances, ship traffic in a stratified canal will create a supercritical internal wave field. The orbital motions of the internal waves give oppositely directed velocities in the wave field. The resulting shear instabilities contribute to mixing. Internal wave breaking on the slope seems to contribute as well to mixing. More research is needed to model and study effects at the canal banks better. The contribution of the internal waves is found to be minimum in the range of 0.5 to 2.1% decrease in PEA with a maximum of about twice this range.
  - *Propeller jet*
    The propeller jet is likely to play a role. The interface is elevated behind the vessel, resulting in an interface close to the propeller. The high velocities and turbulence of the propeller jet are thought to be able to subsequently easily mix the surrounding fluid. Furthermore, the propeller may influence the flow around the ship hull, and the propeller jet provides an opposite flow to the wake of the return current. Since these may also have a significant effect on the return currents and the behaviour of the interface observed in the present study, it is recommended to add the propeller jet to the model. Quick estimations using typical propeller jet velocities give that the propeller could significantly contribute to mixing, however, the question is how much mixing the propeller jet can realise in a short time period. The velocities are about the same order of magnitude or higher than the return current, so similar amount of mixing is estimated to be generated by the propeller jet.

  A combination of these processes determines the amount of mixing in the flow. The return current and internal wave system have a similar importance with a slightly larger contribution for the wave field. The contribution of the propeller jet is not studied in numerical model, but is expected to increase the amount of mixing.

- **What are the governing parameters in these processes, and how do these parameters influence vertical mixing and transport?**
  The vessel speed and canal blockage are most important in determining the return current. The internal wave system is set by the vessel speed and density profile. A larger disturbance also creates larger waves and so the ratio of draught to top layer height, d/h_1, is an important parameter for the wave field. In general, a larger return current or larger interface motions resulted in more mixing.

  The influence of these parameters is described below.

  - *Internal Froude number*
    The internal Froude number is a good predictor of the angle of the V-shape of the waves. It is not an indicator for the height of the interface motions or the amount of mixing.
  - *Vessel speed*
    A higher vessel speed results in a higher return current. This results in more mixing by velocity shear.
  - *Density profile*
    Runs with a tanh-profile and with a linear profile have been done. Compared to the tanh-profile, the linear profile showed a larger amount of low Richardson numbers over the depth due to the change of density gradient. This leads to more mixing for the same density difference for the linear profile. The influence of other changes in the density profile (the density difference and layer distribution) are discussed below.
  - *Density ratio, ρ_1/ρ_2*
    A larger density difference results in larger internal waves. It also changes the wake behind the vessel. More mixing is generated for a larger density difference.
  - *Layer distribution, h_1/h*
    The change of layer distribution in a semi-two layer flow results in larger waves for smaller top layers. This is found to be corresponding to an increase in d/h_1. The amount of mixing increased as the h_1/h-ratio moved further away from 0.5. The most mixing was found for small $h1/h$-values.
  - *Canal blockage*
    A larger canal blockage leads to a higher return current. It does not necessarily result in an increase in wave heights. It is also not a good predictor of the amount of mixing.
  - *Draught to top layer ratio, d/h_1*
    The draught to top layer ratio is found to be an important parameter for the interface deformations underneath the vessel and the internal waves behind the vessel. These become larger for larger d/h_1-ratios. This results in more mixing for larger d/h_1-ratios.
  - *Slope of canal banks*
    The presence of sloped canal banks almost completely removed the wave reflection and resulted in wave dissipation at the canal banks. A shallower slope of the canal bank resulted in slightly more mixing.

- **How significant is the effect of shipping traffic on mixing and transport of salinity in relation to other mixing and transport terms?**
  A detailed comparison of the effect of ship traffic with other mixing and transport terms has in the end not been included in this study. Estimates based on the numerical runs of the cumulative effect of ship traffic in 6.3 show that ships can have an important role in the amount of stratification. These estimations show that the decrease in ship traffic might be coupled with measured salinity peaks in the Amsterdam-Rijnkanaal and Antwerps Kanaalpand. Moreover, this section argued that ships might have a role in mixing the top of the water column in the Noordzeekanaal, although this effect is not as clearly visible from the performed model runs. This combination of field observations and numerical model results show that ship traffic has an important role in mixing of salinity in canals.

- **Which steps need to be taken to include the mixing and transport of salinity caused by ship traffic in weakly-dynamical inland waterways in 2DV- and 3D numerical models?**
  This question has not been studied in detail. This parameter study is a first step towards a parameterisation of mixing by ship traffic. More research is needed to better understand mixing by ship traffic as will be argued in the next section. The influence of the propeller jet and how to go from the effect of one vessel to multiple vessels are important next steps, as well as the validation of these results. This parameterisation can then be used to estimate the amount of mixing in a canal using information on the canal characteristics and the typical ship traffic. Depending on the requirements on the model and the canal characteristics, a certain level of detail could be used to implement the mixing in a large-scale numerical model.

7.2. Recommendations

The most important recommendations for further research on this topic are given below. Furthermore, as became clear in Chapter 6, several aspects of the numerical model set up could be improved, most notably the mesh generation. It is expected that this will not give a different pattern, however, it would give some more detail. The same goes for the roughness coefficient and density profile that is used. This study has given a good basis to build on for further studies as it showed the main patterns.

- **Adding a propeller**
  The propeller jet has not been included in the model, however, there are indications that it might play an important role. Adding a propeller to the model will change the flow field considerably, and will most likely generate more mixing. To understand this better and to find how much mixing a propeller would add, more study is needed. A numerical study would be a good option for this, although, a fine resolution in the propeller jet is needed to accurately model the small-scales. A scale model with a propeller will be complicated due to scale effects.

- **Validation of the results**
  The model results have not been validated, and Finlab has not yet been validated for the use of a moving mesh or the combination of using a moving mesh with a density gradient. It would therefore be good to do validation tests. Field measurements will have many practical complications. Laboratory experiments would be the most logical way of validating the results. The accuracy of the model result for low velocities would require special attention, as in this study these results were unclear.

- **Longer model domain**
  The return current causes some disturbances at the inflow boundary in the model, and the effect of the wave field is not completely visible in the current results. In a next study, it would be interesting to model a longer canal stretch to study the full effect of the wave field, however, attention should be paid to the mesh generation. Modelling a longer stretch of canal makes mesh generation and convergence of the model harder.

- **Effect of multiple ships**
  In Section 6.3, a quick estimation of the effect of multiple ships has been given. This is a very rough estimation. The effect of multiple ships should therefore be studied to know how to get from one ship to multiple ships. A numerical model that connects the outflow boundary conditions to the inflow boundary conditions could be used for this and thereby simulates a canal with ships sailing in regular intervals could be used. Also, laboratory tests in a flume could be used. This is an important step before a parameterisation can be made.

- **Wave breaking and reflection**
  Internal wave breaking and reflection on a slope for typical dimensions in an inland waterway are not yet well understood. This study has found some effect on mixing for the runs with a slope, however, the effect is not clearly visible. It would be helpful to study this problem in a higher resolution, which could be done using a simple geometry and generating internal waves comparable to the ship waves.

- **Other parameters**
  As mentioned in Chapter 6, some parameters likely to be of importance have not been studied.

The runs with low velocity showed large decrease in PEA which could not be explained physically. Also, the runs with a large draught need improvement on the resolution of the mesh. The influence of the free surface waves on the internal waves is likely to be small, however, could have an influence, especially for lower top layers. As velocity shear at the ship hull and bed are found to be an important contribution to mixing, it would be good to further study the effect of the roughness coefficients and see if a different roughness can be applied to the hull and the bed. Additionally, sailing eccentrically to the axis of the canal will cause asymmetry in the return current, and waves to reach the sides of the canal sooner. The effect of bends or side canals has not yet been studied. All runs so far have been done without discharge in the canal. In reality, there will be a discharge in the canal. The change in length of the boat has also not been studied, even though it is a component of the critical internal Froude number.

- **Parameterisation**
  Next steps towards parameterisation have been discussed above and in Chapter 6. First, a better understanding of the processes is needed and it should be studied how the effect of multiple ships can be added. The type of parameterisation is likely to be situation-specific. Possible ways to include this in numerical models needs further study.

References

Aghsaee, P., Boegman, L., and Lamb, K. G. (2010). Breaking of shoaling internal solitary waves. *Journal of Fluid Mechanics*, 659:289.

Ahrens, J., Geveci, B., and Law, C. (2005). Paraview: An end-user tool for large data visualization. *The visualization handbook*, 717(8).

Arthur, R. S. and Fringer, O. B. (2014). The dynamics of breaking internal solitary waves on slopes. *Journal of Fluid Mechanics*, 761:360–398.

Baines, P. (1984). A unified description of two-layer flow over topography. *Journal of Fluid Mechanics*, 146:127–167.

Baines, P. (2016). Internal hydraulic jumps in two-layer systems. *Journal of Fluid Mechanics*, 787:1–15.

Baines, P. G. (1987). Upstream blocking and airflow over mountains. *Annual review of fluid mechanics*, 19(1):75–95.

Bijlsma, A. (2020). Interne golven op het Noordzeekanaal en het Amsterdam-Rijnkanaal. Memo 11203735-006-ZWS-0005.

Bijlsma, A. and Weiler, O. (2016). Zoutindringing IJmuiden fase 3: Verdere uitwerking mogelijke bronmaatregelen. Report, Deltares. Deltares report 1220309-000.

Blaauw, H. and van de Kaa, E. (1978). Erosion of bottom and sloping banks caused by the screw race of manoeuvring ships. publ. no. 202,. Report. 202.

Boegman, L., Ivey, G. N., and Imberger, J. (2005). The degeneration of internal waves in lakes with sloping topography. *Limnology and Oceanography*, 50(5):1620–1637.

Boon, C. v. d. (2011). *Numerical modelling of internal waves in the Browse Basin*. Thesis. Delft University of Technology.

Brucker, K. A. and Sarkar, S. (2010). A comparative study of self-propelled and towed wakes in a stratified fluid. *Journal of Fluid Mechanics*, 652:373–404.

Bruggeling, M., Groot, B. d., and Thijs, R. (2014). SIVAK-simulatie IZZS Krammersluizen. Report, TBA Group. [presentation, May 2014, rev.4].

Chang, Y., Zhao, F., Zhang, J., Hong, F., Li, P., and Yun, J. (2006). Numerical simulation of internal waves excited by a submarine moving in the two-layer stratified fluid. *Journal of Hydrodynamics, Ser. B*, 18(3, Supplement):330–336.

Crapper, G. D. (1967). Ship waves in a stratified ocean. *Journal of Fluid Mechanics*, 29(4):667–672.

Cushman-Roisin, B. (1994). *Introduction to geophysical fluid dynamics*. Prentice Hall, Englewood Cliffs, N.J.

de Jong, M., Roelvink, D., Reijmerink, S., and Breederveld, C. (2013). Paper 95-Numerical modelling of passing-ship effects in complex geometries and on shallow water. Presented at PIANC Smart Rivers (Liege (BE), Maastricht (NL), 2013 (Paper 95).

Esmaeilpour, M. (2017). *A ship advancing in a stratified fluid: the dead water effect revisited*. Thesis. University of Iowa.

Esmaeilpour, M., Ezequiel Martin, J., and Carrica, P. (2018). Computational fluid dynamics study of the dead water problem. *Journal of Fluids Engineering*, 140(3).

Esmaeilpour, M., Martin, J. E., and Carrica, P. M. (2016). Near-field flow of submarines and ships advancing in a stable stratified fluid. *Ocean Engineering*, 123:75–95.

Fischer, H. B. (1979). *Mixing in inland and coastal waters*. Academic Press, New York.

Fourdrinoy, J., Dambrine, J., Petcu, M., Pierre, M., and Rousseaux, G. (2020). The dual nature of the dead-water phenomenology: Nansen versus Ekman wave-making drags. *Proceedings of the National Academy of Sciences*, 117(29):16770.

Fringer, O. B. and Street, R. L. (2003). The dynamics of breaking progressive interfacial waves. *Journal of Fluid Mechanics*, 494:319.

Fructus, D. and Grue, J. (2004). Fully nonlinear solitary waves in a layered stratified fluid. *Journal of Fluid Mechanics*, 505:323.

Geuzaine, C. and Remacle, J. (2009). Gmsh: A 3d finite element mesh generator with built-in pre-and post-processing facilities. *International journal for numerical methods in engineering*, 79(11):1309–1331.

Geyer, W. R., Scully, M. E., and Ralston, D. K. (2008). Quantifying vertical mixing in estuaries. *Environmental Fluid Mechanics*, 8(5):495–509.

Haasnoot, M., Bouwer, L., Diermanse, F., Kwadijk, J., van der Spek, A., Oude Essink, G., Delsman, J., Weiler, O., Mens, M., ter Maat, J., Huismans, Y., Sloff, K., and Mosselman, E. (2018). Mogelijke gevolgen van versnelde zeespiegelstijging voor het Deltaprogramma : een verkenning. Report, Deltares. Deltares rapport 11202230-005-0002.

Hogg, A. M. and Ivey, G. N. (2003). The Kelvin–Helmholtz to Holmboe instability transition in stratified exchange flows. *Journal of Fluid Mechanics*, 477:339–362.

Hydrologic (2020). Analyse chloride Amsterdam-Rijnkanaal. Report, Hydrologic. P1204.

Ivey, G., Winters, K., and Koseff, J. (2008). Density stratification, turbulence, but how much mixing? *Annual Review of Fluid Mechanics*, 40(1):169–184.

Kang, D. and Fringer, O. (2010). On the calculation of available potential energy in internal wave fields. *Journal of Physical Oceanography*, 40(11):2539–2545.

Karaki, S. and VanHoften, J. (1975). Resuspension of bed material and wave effects on the Illinois and Upper Mississippi Rivers caused by boat traffic. Report, Colarado State Univ Fort Collins Engineering Research Center. LMSSD 75-881.

Karelse, M. and Van Gils, J. (1991). Noordzeekanaal, Amsterdam-Rijnkanaal: waterbeweging en zouthuishouding. Report, WL Delft Hydraulics. Voorstudie t.b.v. modellering, i.o.v. Rijkswaterstaat, Directie Noord-Holland. - Nota ANW 91.11.

Kikkert, A. (2015). *Afvoerdebieten van het Noordzeekanaal inventarisatie van beschikbare data*. Rijkswaterstaat.

Koedijk, O. (2020). Richtlijnen vaarwegen 2020. Report, Ministerie van Infrastructuur en Waterstaat, Rijkswaterstaat Water, Verkeer en Leefomgeving (RWS, WVL). ISBN 9789090334233.

Kundu, P. K. (2013). *Fluid Mechanics*. Academic Press, Oxford. Accession Number: 596581; OCLC: 843201802; Language: English.

Labeur, R. (2009). *Finite element modelling of transport and non-hydrostatic flow in environmental fluid mechanics*. Thesis. PhD thesis Delft University of Technology.

Labeur, R. J. and Pietrzak, J. D. (2005). A fully three dimensional unstructured grid non-hydrostatic finite element coastal model. *Ocean Modelling*, 10(1-2):51–67.

Lam, W., Hamil, G. A., Song, Y. C., Robinson, D. J., and Raghunathan, S. (2011). A review of the equations used to predict the velocity distribution within a ship's propeller jet. *Ocean Engineering*, 38(1):1–10.

Lamb, K. G. (2014). Internal wave breaking and dissipation mechanisms on the continental slope/shelf. *Annual Review of Fluid Mechanics*, 46(1):231–254.

Lawrence, G. A., Browand, F. K., and Redekopp, L. G. (1991). The stability of a sheared density interface. *Physics of Fluids A: Fluid Dynamics*, 3(10):2360–2370.

Maderich, V., Heling, R., Bezhenar, R., Brovchenko, I., Jenner, H., Koshebutskyy, V., Kuschan, A., and Terletska, K. (2008). Development and application of 3D numerical model THREETOX to the prediction of cooling water transport and mixing in the inland and coastal waters. *Hydrological Processes*, 22(7):1000–1013.

Masunaga, E., Arthur, R. S., and Fringer, O. B. (2019). Internal wave breaking dynamics and associated mixing in the coastal ocean. *Encyclopedia of Ocean Science*, pages 548–554.

Medjdoub, K., Jánosi, I., and Vincze, M. (2020). Laboratory investigations on the resonant feature of 'dead water' phenomenon. *Experiments in Fluids : Experimental Methods and their Applications to Fluid Flow*, 61(1):1–12.

Moser, G. and Bakker, J. (1989). Mixing caused by shipping traffic. Report WL258, WL Delft Hydraulics. WL258.

Moser, G.M. Bakker, J. (1985). Onderzoek naar menging door scheepvaart in de Westsluis van het Volkeraksluizencomplex. Report, WL Delft Hydraulics, Delft. M 896 - 55 WL/WWZW-43.004.01 RWS.

Moum, J. N., Klymak, J. M., Nash, J. D., Perlin, A., and Smyth, W. D. (2007). Energy transport by nonlinear internal waves. *Journal of Physical Oceanography*, 37(7):1968–1988.

Narimousa, S. and Fernando, H. J. S. (1987). On the sheared density interface of an entraining stratified fluid. *Journal of Fluid Mechanics*, 174:1–22.

Peltier, W. R. and Caulfield, C. P. (2003). Mixing efficiency in stratified shear flows. *Annual Review of Fluid Mechanics*, 35(1):135–167.

PIANC (1987). *Guidelines for the Design and Construction of Flexible Revetments Incorporating Geotextiles for Inland Waterways: Report of Working Group 4 of the Permanent Technical Committee I*. Supplement to Bulletin No 57.

PIANC (2015). Guidelines for protecting berthing structures from scour caused by ships. Report. Rep. No. 180/ISBN978-2-87223-223-9.

Pietrzak, J. (2012). *An introduction to Stratified Flows for Civil and Offshore Engineers: "From Shelf to Shore"*. Delft University of Technology.

Pietrzak, J. and Labeur, R. J. (2004). Trapped internal waves over undular topography in a partially mixed estuary. *Ocean Dynamics*, 54(3):315–323.

Rietveld, M. (2015). Geregistreerd sluisbedrijf 2013 en 2014 op basis van PONTIS. Report, Deltares. Appendix by Deltares report 1220309-000.

Rijkswaterstaat (2020a). Vaarweginformatie. URL: https://www.vaarweginformatie.nl (Last accessed on 11/03/2021).

Rijkswaterstaat (2020b). Waterinfo - zoutmetingen. URL: www.waterinfo.rws.nl (Last accessed on 11/03/2021).

Sano, M. and Kunitake, Y. (2017). Numerical solution for a ship-wave problem in a two-layer fluid using a double-model linearised interface condition. *Ships and Offshore Structures*, 13(3):293–302.

Sarkar, S. (2005). *Prototypical examples of stratified shear flow*, pages 133–178. Springer, Vienna.

Savenije, H. (2012). Salinity and tides in alluvial estuaries, 2nd completely revised edition: salinityandtides.com.

Sharman, R. D. and Wurtele, M. G. (1983). Ship waves and lee waves. *Journal of the Atmospheric Sciences*, 40(2):396–427.

Simpson, J. H., Brown, J., Matthews, J., and Allen, G. (1990). Tidal straining, density currents, and stirring in the control of estuarine stratification. *Estuaries*, 13(2):125–132.

Snyder, W. H., Thompson, R. S., Eskridge, R. E., Lawson, R. E., Castro, I. P., Lee, J., Hunt, J. C., and Ogawa, Y. (1985). The structure of strongly stratified flow over hills: dividing-streamline concept. *Journal of Fluid Mechanics*, 152:249–288.

Staquet, C. and Sommeria, J. (2002). Internal gravity waves: From instabilities to turbulence. *Annual Review of Fluid Mechanics*, 34(1):559–593.

Steenepoorte, K. (2016). De Kreekraksluizen in de Schelde-Rijnverbinding. Report, Ministerie van Infrastructuur en Milieu, Rijkswaterstaat Zee en Delta (RWS, ZD). ZD1116ZB001.

Stefan, H. and Riley, M. J. (1985). Mixing of a stratified river by barge tows. *Water Resources Research*, 21(8):1085–1094.

Strang, E. J. and Fernando, H. J. S. (2001). Entrainment and mixing in stratified shear flows. *Journal of Fluid Mechanics*, 428:349–386.

Sullivan, G. D. and List, E. J. (1994). On mixing and transport at a sheared density interface. *Journal of Fluid Mechanics*, 273:213–239.

Sutherland, B. R. (2010). *Internal Gravity Waves*. Cambridge University Press, Cambridge (UK).

Sutherland, B. R., Barrett, K. J., and Ivey, G. N. (2013). Shoaling internal solitary waves. *Journal of Geophysical Research: Oceans*, 118(9):4111–4124.

Ten Hove, D. (2008). Herziening inventarisatie manoevreermiddelen. *MARIN 22788.600/3*.

Ten Hove, D. (2010). Scheepskarakteristieken van nieuwe grote schepen. *MARIN 24032.600/2*.

van der Hout, A. (2011). Ship in a 2DH shallow-water flow model. Report, Deltares. 1202340-002-HYE-0001.

van Page, H., Dekker, L., and Lievense, P. (2018). Gevolgen van een zout Volkerak-Zoommeer voor het Antwerps Kanaalpand en het Schelde estuarium. Report, Rijkswaterstaat - Waterdienst.

Vantorre, M. (1991). Ship behaviour and control at low speed in layered fluids. As presented at the International Symposium on Hydro- and Aerodynamics in Marine Engineering in Varna (Bulgaria).

Vantorre, M. (2001). Nautical bottom approach-application to the access to the harbour of Zeebrugge. *HANSA - Schiffart - Schiffbau - Hafen*, (138. Jahrgang, Nr. 6):93–97.

Vantorre, M. and Coen, I. (1988). *On sinkage and trim of vessels navigating above a mud layer*. Royal Flemish Society of Engineers (K VIV), Antwerp. ISBN 90-5204-001-X. Vol.1 (1.1-3.104; 1-78); Vol.2 (4.1-7.16) pp.

Venayagamoorthy, S. K. and Koseff, J. R. (2016). On the flux Richardson number in stably stratified turbulence. *Journal of Fluid Mechanics*, 798:R1.

Verbruggen, W. and Baan, J. v. d. (2020). Ontwikkeling zesde-generatie 3D Noordzeekanaal Amsterdam-Rijnkanaal model : modelbouw, kalibratie en validatie. Report, Deltares. 11205258-011-ZWS-0004.

Verbruggen, W. and Buschman, F. (2020). Evaluatie maatregelen constanter water afvoeren in het Noordzeekanaal en het Amsterdam-Rijnkaal. Report, Deltares. 11203735-006-ZWS-0007.

Verheij, H., Stolker, C., and Groenveld, R. (2008). *Inland waterways: ports, waterways and inland navigation*. VSSD, Delft.

Voropayev, S. I., Nath, C., and Fernando, H. J. S. (2012). Thermal surface signatures of ship propeller wakes in stratified waters. *Physics of Fluids*, 24(11).

Yeung, R. W. and Nguyen, T. C. (1999). Waves generated by a moving source in a two-layer ocean of finite depth. *Journal of Engineering Mathematics*, 35(1):85–107.

A

Salinity measurements in the Noordzeekanaal

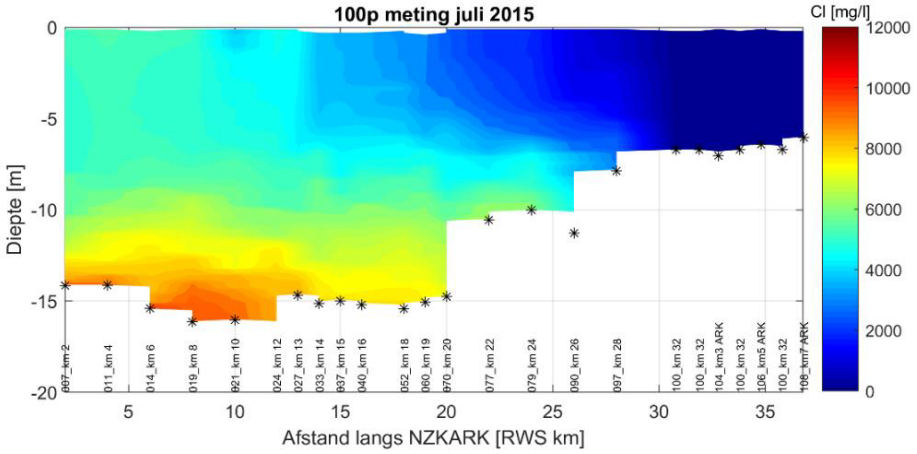

Figure A.1: Results of 100-point measurements in the Noordzeekanaal in July 2015. Figure from Verbruggen and Baan (2020).

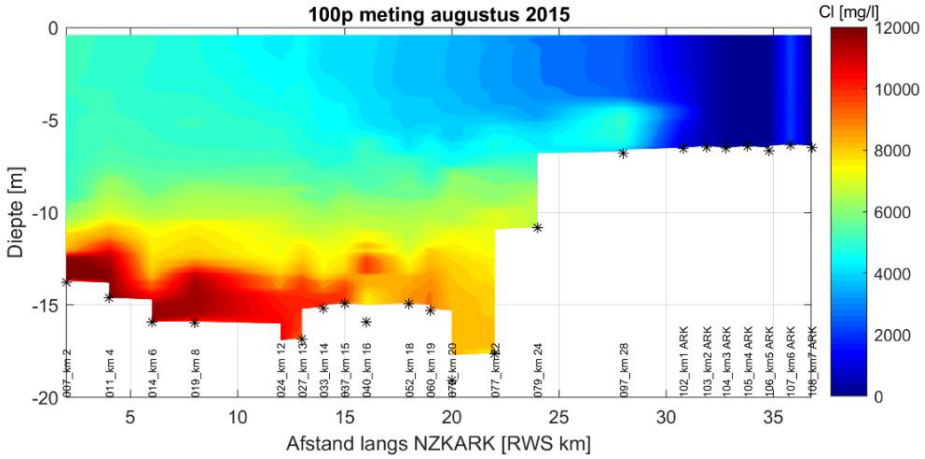

Figure A.2: Results of 100-point measurements in the Noordzeekanaal in August 2015. Figure from Verbruggen and Baan (2020).

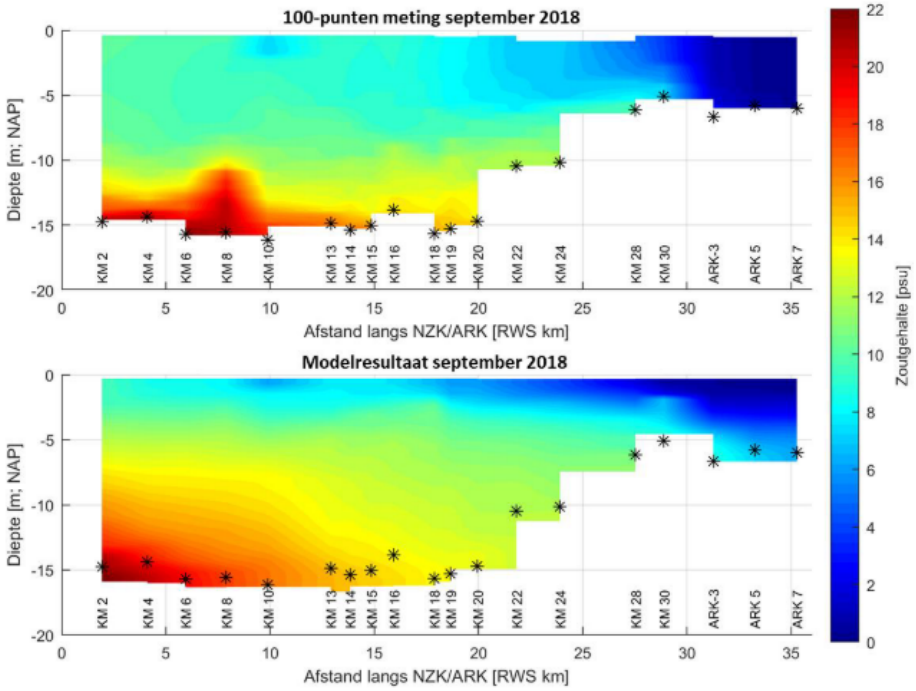

Figure A.3: Top: Results of 100-point measurements in the Noordzeekanaal in September 2018. Bottom: Numerical model results corresponding to these measurements. The results are very close to the measured values, however, give a more linear profile. Figure from Verbruggen and Buschman (2020).

B

Blockage of the Eendracht canal

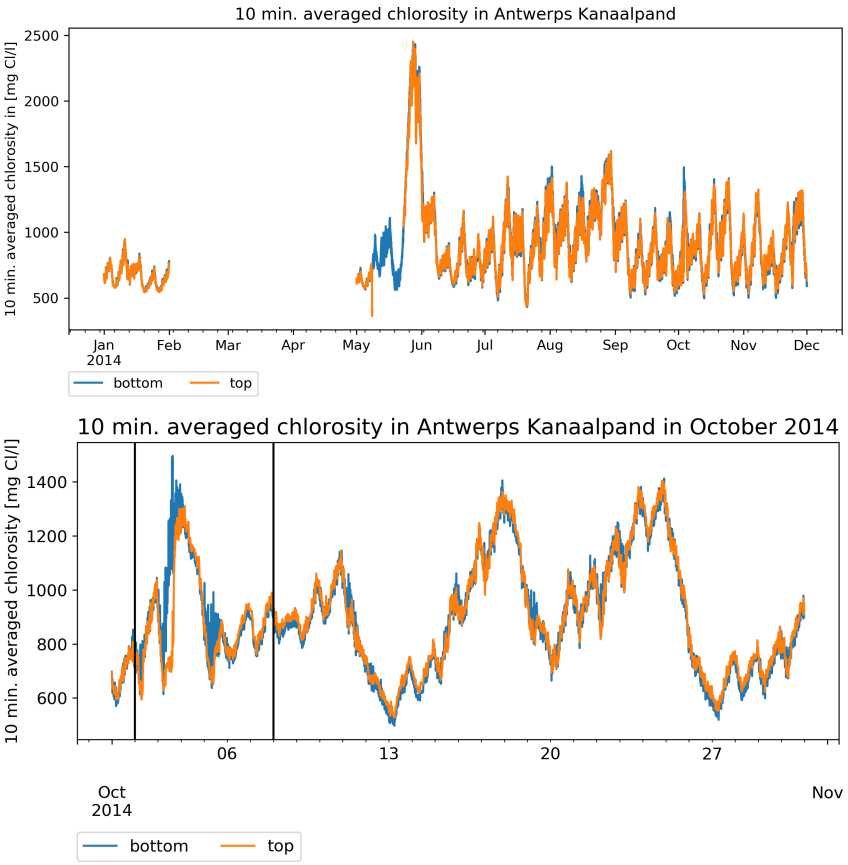

Figure B.1: 10-minute averaged chloride levels in het Antwerps Kanaalpand for the year 2014 and the month October of that year. The time period of the blockage of the Eendracht is indicated in black. (Data from Rijkswaterstaat (2020b))

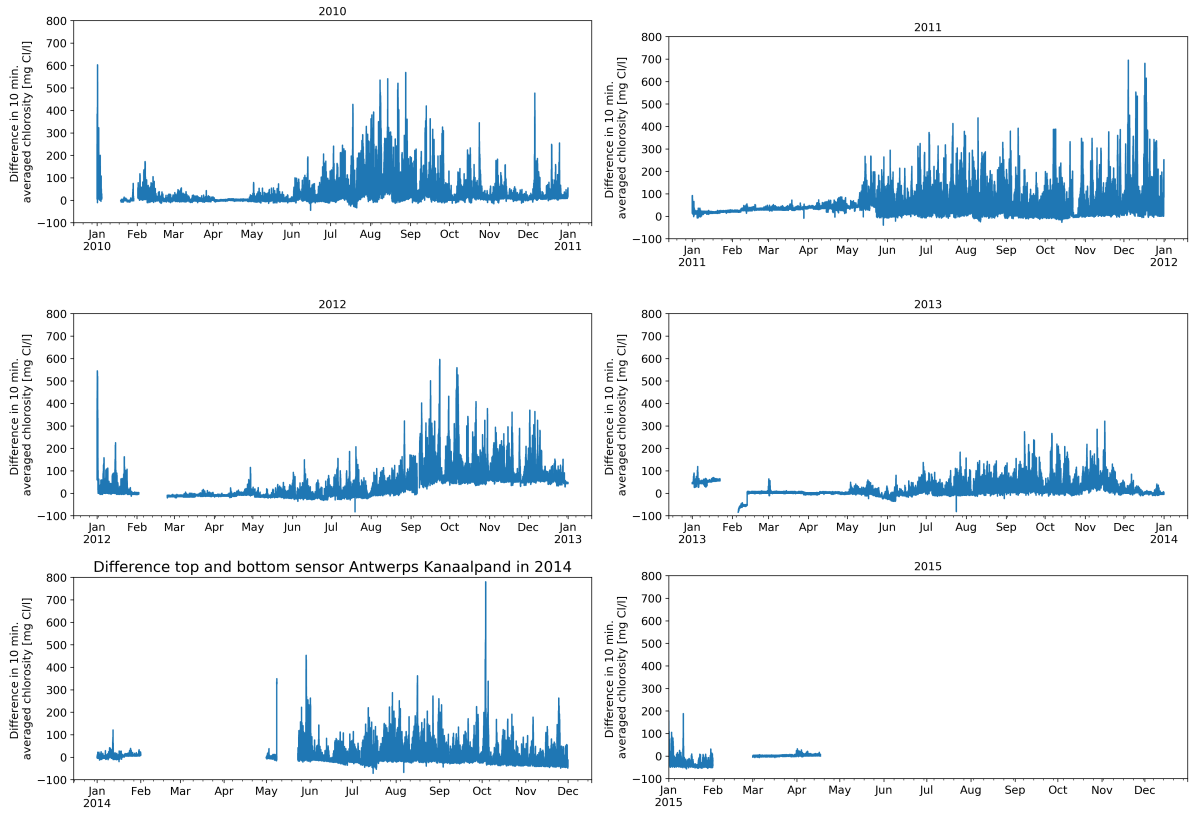

Figure B.2: Difference between the top and bottom chloride sensor in the Antwerps Kanaalpand from January 2010 to April 2015. Higher values indicate more stratification. The peak in October 2014 is at the time of the blockage of the Eendracht canal (Data from Rijkswaterstaat (2020b))

C

Parameter input: Energy estimation

		Noordzeekanaal	Amsterdam Rijnkanaal	Antwerps Kanaalpand
d	m	15	6	5
B	m	220	110	140
$\bar{\rho}$	kg/m^3	1012	1006	1002
Q	m^3/s	500	120	3.5
U	m/s	0.152	0.182	0.00455
n_{inland}	-	4	0,5	6
$n_{seagoing}$	-	4	-	-
P_{inland}	kW	370	370	370
$P_{seagoing}$	kW	1800	-	-

Table C.1: Overview of input parameters for energy estimation of the contribution of current, wind, and ships.

D

Modelling a moving vessel

Adding a moving ship to a numerical model poses certain challenges (de Jong et al., 2013). This section looks at the possibilities and implied consequences of certain methods in order to select the best method for this research.

Maderich et al. (2008) have developed a 3D-model to model cooling water transport and mixing and look in their research also at the effect of ship traffic on the dispersion of discharged heat from cooling water. In the Amsterdam-Rijn Kanaal (ARK) the large amount of shipping traffic and the vertical mixing this causes can affect heat dispersion. Shipping traffic is added to the model as a ship-generated component to the vertical eddy- and diffusion coefficients in the upper layer of the canal using the turbulent kinetic energy generated by the propeller.

For the numerical experiments, it would not be a good option to add a vessel by parametrisation as it will not improve understanding of the mixing processes. However, it is the goal to translate the final result in a parametrisation for large-scale models. This could be as a time-averaged component such as used above or as a stochastic parameter based on ship traffic statistics.

de Jong et al. (2013) names the double body method or the potential flow method as the traditional method to model the forces of a sailing ship. However, this is a linear method and will therefore not be considered further. van der Hout (2011) names three methods to add a ship to a model: 1) via a moving pressure field, 2) via immersed boundary method, 3) via the bathymetry. These are further explained below.

de Jong et al. (2013) used the first method, and added a moving, local increase in the atmospheric pressure in XBeach. The level of detail is limited by the grid resolution. This method shows the primary ship wave farther away from the ship well, but secondary waves are not well represented in this model. Friction from the structure on the flow is also not included (van der Hout, 2011).

This pressure field method can also be applied to Delft-3D or D-Hydro FM. A study in Delft3D Flow has been done by van der Hout (2011). Numerical oscillations were suppressed by increasing the horizontal background viscosity and applying a more dissipative numerical scheme. This resulted in a realistic model of the primary ship wave. The pressure field has to described for every time step to simulate a passing ship. To make this easier, an option would be to apply moving pressure fields, such as is for example done to model cyclones. A rigid shape represents the reality close to the ship better, because in that case ship waves cannot travel 'through the ship'. In Delft3D Flow, a method exists to add a pressure field with a rigid lid assumption, however, in this method the pressure field cannot move (van der Hout, 2011).

The second method is the immersed boundary method. In this method, the flow is given a different velocity at the location of the vessel. In this way, a solid body is modelled. van der Hout (2011) concluded that the method has potential, however, the wake of the ship is not modelled well and the method caused a relatively large boundary layer at the ships hull when increasing the viscosity because of large grid dimensions. This method is available for D-Hydro FM (UNSTRUC).

The third method is to update the bathymetry. In Delft3D, this would mean adding a moving shape on the bottom to simulate the local effective water depth reduction (van der Hout, 2011). Another method is available for the FinLab model. In this method, the mesh is deformed at the location of the ship and moves with the speed of the ship. This reduces numerical artefacts.

E

Numerical set-up

This chapter gives the parameters used in the numerical model runs and is an extension of Chapter 4. The parameters are grouped by category in different tables below.

	Parameter	Unit	Value
R0	relative density transport variable	-	0.01
Ma	Mach number	-	0.05

Table E.1: Physical constants

	Parameter	Unit	Value
dt	time step	s	0.5
theta	implicitness momentum equation	-	1
zeta	implicitness continuity equation	-	1
method	time discretisation	-	2 - Fractional step
move	move surface or rigid lid	-	Rigid lid
Tdamp	damping time	s	200
Tstart	initial time	s	0

Table E.2: Time discretisation

	Parameter	Unit	Value
turb	turbulence model	-	LES
visc0	(minimum) kinematic viscosity	m2/s	1E-06
Lmix	(turbulent) mixing length	m	0
kN0	default Nikuradse wall roughness	m	5E-03
cf0	default wall friction factor	-	0
Cs	Smagorinsky constant	-	0.125
fluc	random velocity fluctuation	-	0

Table E.3: Turbulence

	Parameter	Unit	Value
gamma	advective flux switch		0.5
upw	upwind parameter advection		1
eta	diffusive flux switch		-1
limu	polynomial order advection scheme		1
limc	polynomial order transport scheme		9

Table E.4: Advection-diffusion scheme

F

Additional figures of numerical model results

This chapter gives some additional figures of the numerical model runs and complements Chapter 5. The figures are sorted by set of runs. Chapter 5 often shows the relative decrease in width-averaged PEA or the relative change in width-averaged density. This chapter gives plots of the width-averaged PEA and density for the run with and without a vessel to show the complete picture.

F.1. Run 1 to 12

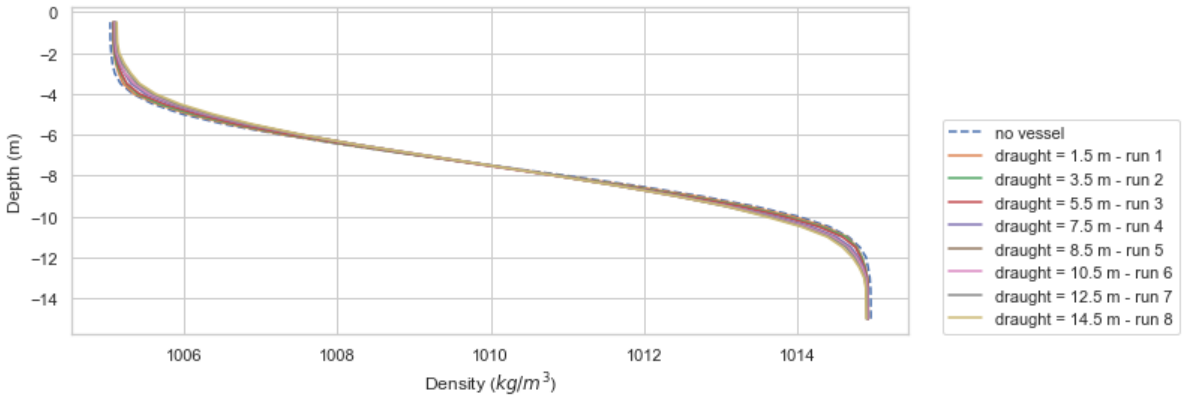

Figure F.1: The width-averaged density profiles at the outflow boundary for an increasing draught (run 1 to 8).

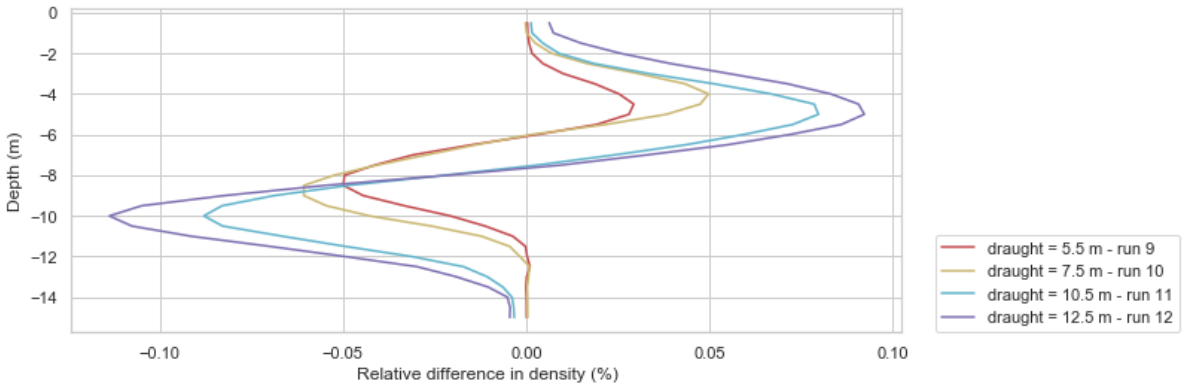

Figure F.2: Relative difference in density at 50 m from the outflow boundary for run 9 to 12 compared to run 0.

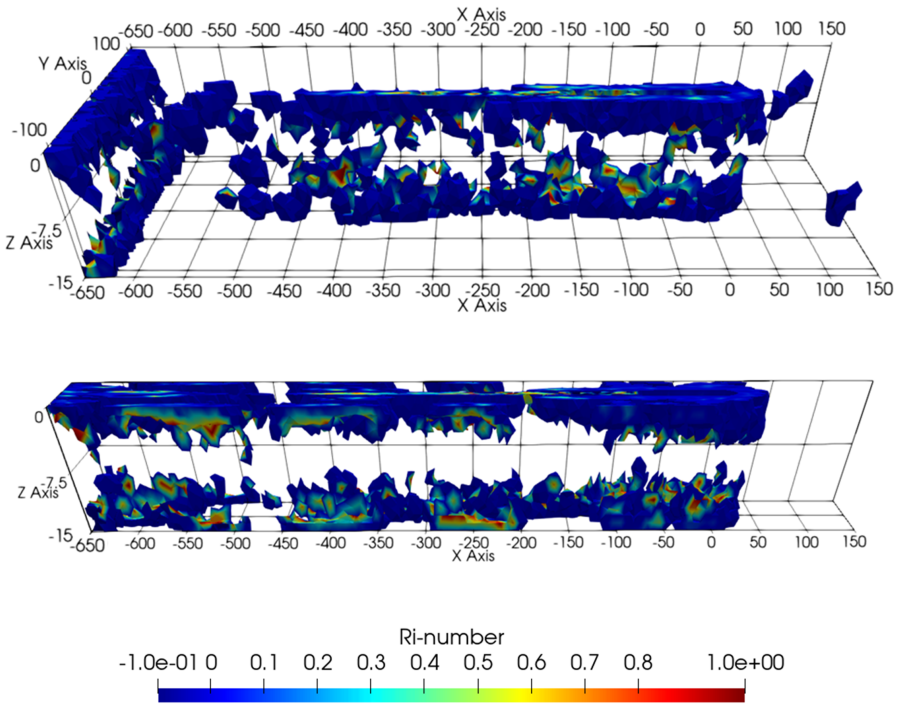

Figure F.3: Negative to 1 Richardson values for run 3 (width = 220 m) and run 9 (width = 50 m). Both runs have a draught of 5.5 m. There is no large difference visible. The z-axis is scaled with a factor 10.

F.2. Run 13 to 16

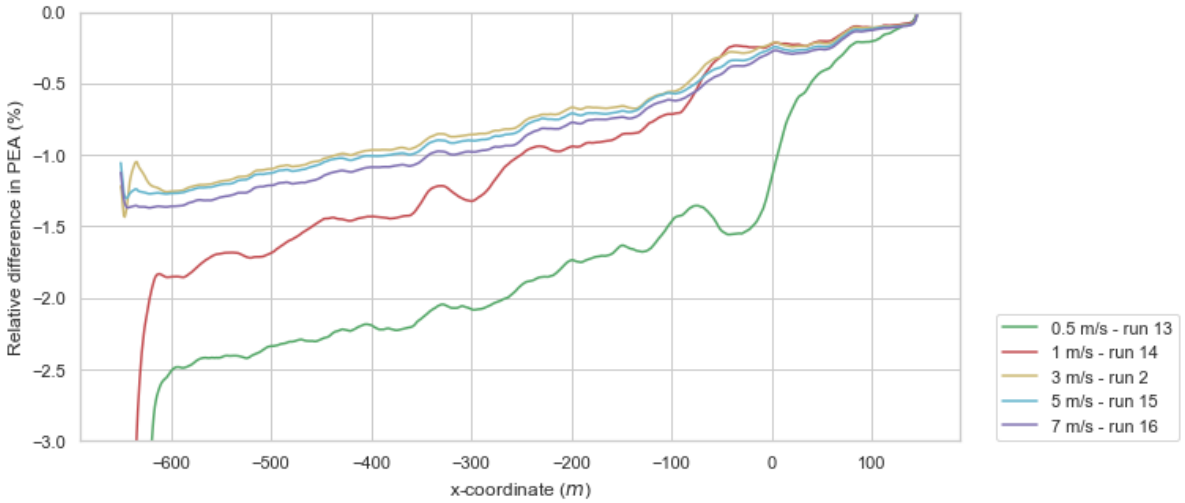

Figure F.4: Relative decrease in PEA for different vessel speeds. The decrease in PEA has been calculated relative to the PEA of a run without a vessel with the same speed. It is unclear why the PEA decreases so quickly for speeds of 0.5 and 1 m/s.

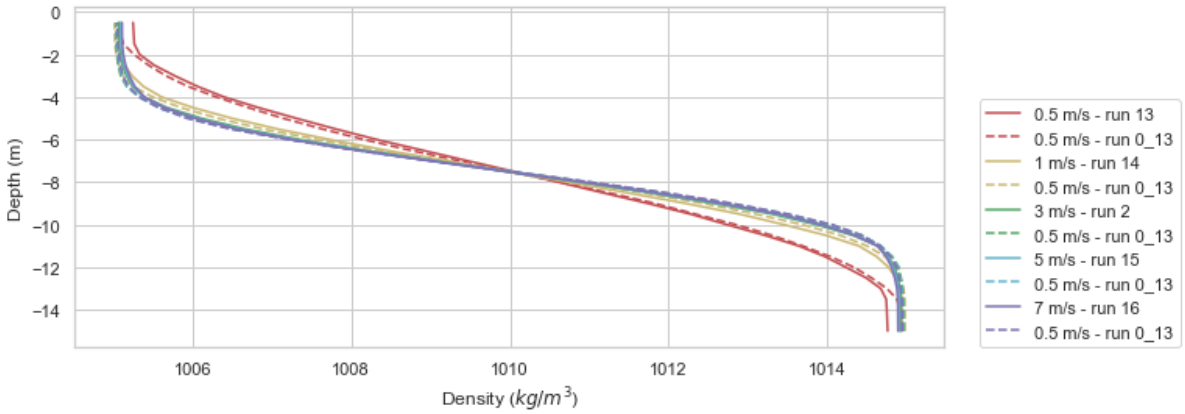

Figure F.5: Density profiles at 50 m from the outflow boundary for run 13 to 16 and corresponding runs without a vessel.

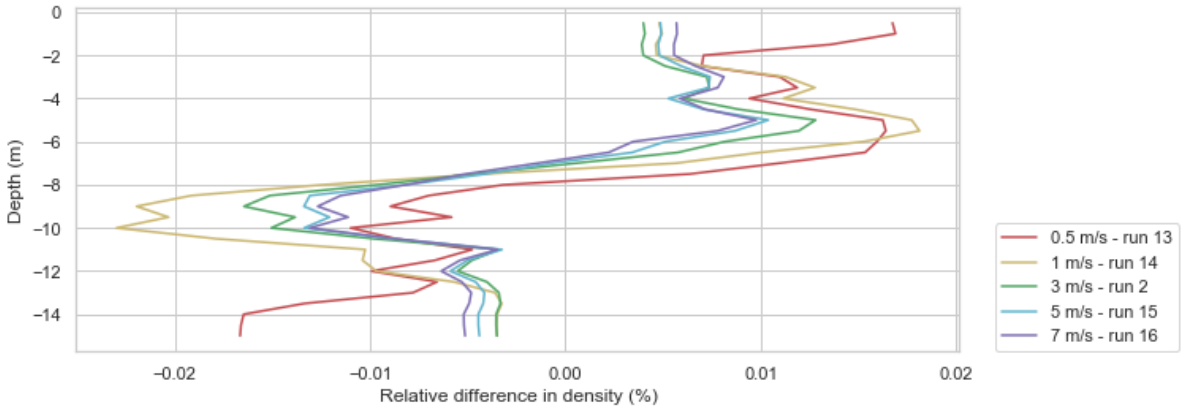

Figure F.6: Relative change in density profile at 50 m from the outflow boundary for run 13 to 16 compared to run without a vessel. It is unclear why run 14 and 14 show such a large change. These runs have been left out of the main analysis.

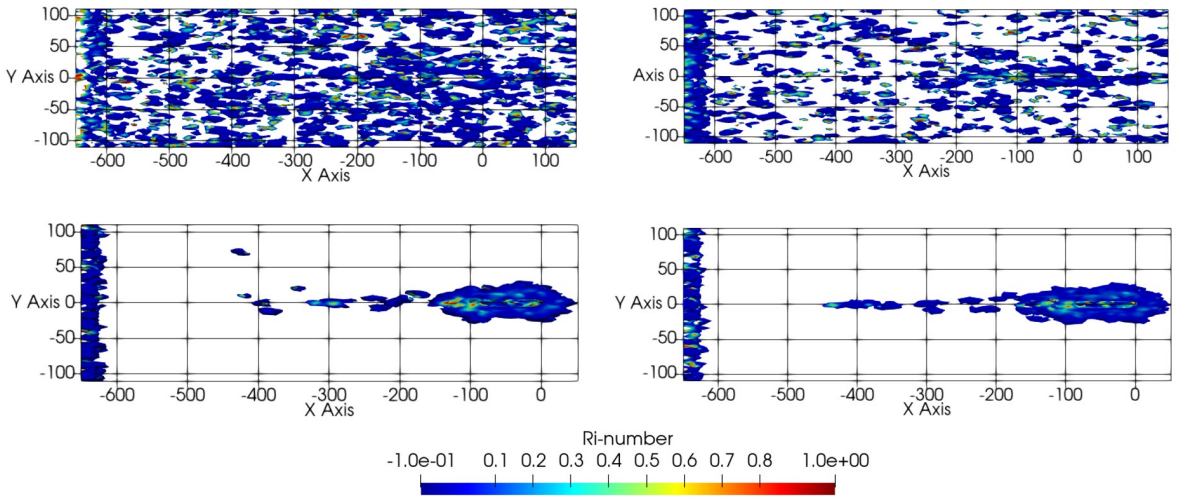

Figure F.7: Low Richardson numbers (negative to 1) for run 13 to 16. Run 13 and 14 are not analysed in the main text as they showed low Richardson numbers throughout the model for both the run with and without a vessel. Run 15 and 16 show low Richarson numbers around the vessel and in the wake following the vessel.

F.3. Run 17 to 20

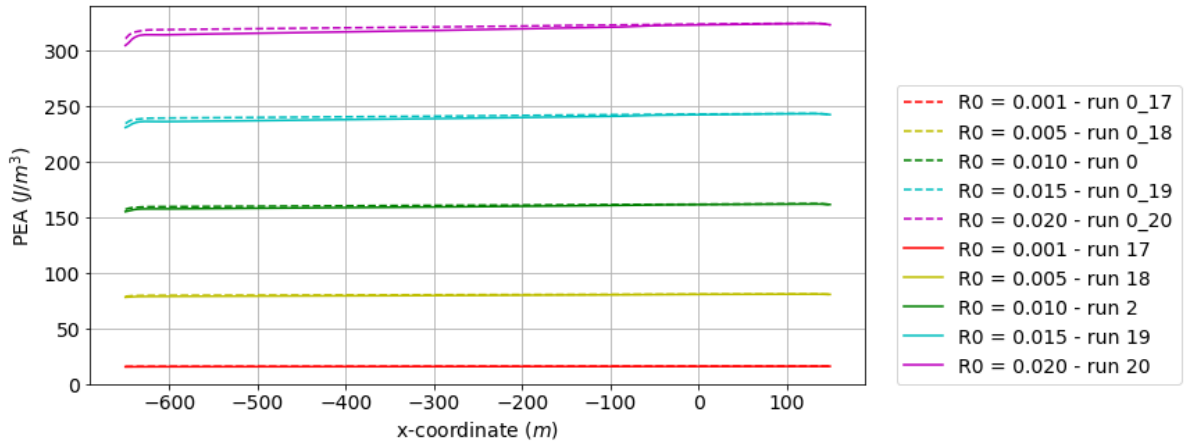

Figure F.8: The width-averaged PEA for run 17 to 20, run 2 and corresponding runs without a vessel. Due to the different relative density differences, the PEA differs a lot between these runs.

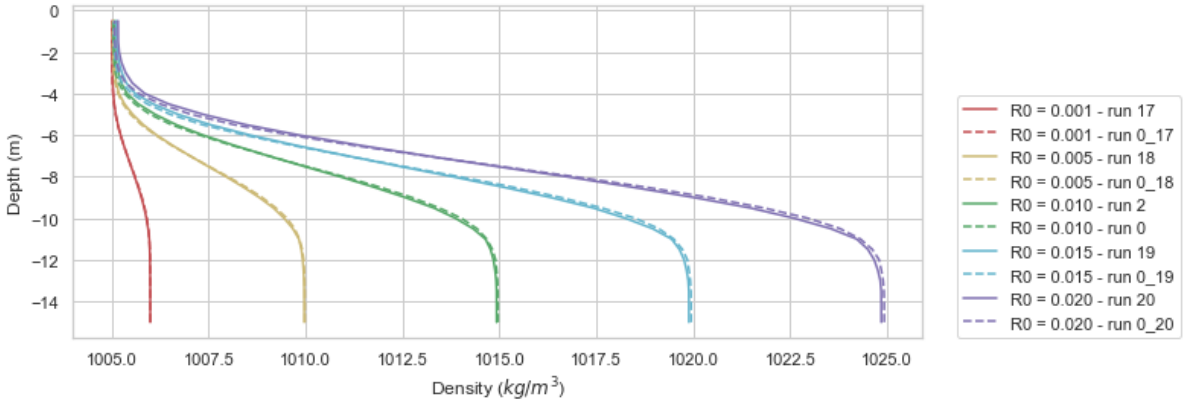

Figure F.9: The density profile at 50 m from the outflow boundary for run 17 to 20, run 2 and corresponding runs without a vessel.

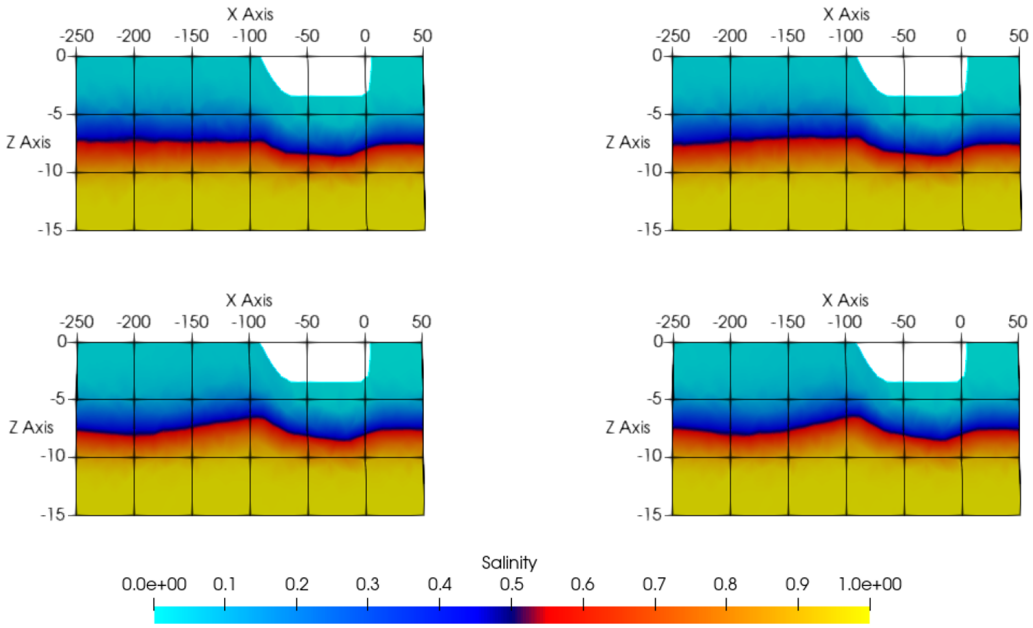

Figure F.10: Comparison of the interface at y = 0 m of run 17 (top, left), 18 (top, right), 19 (bottom, left), and 20 (bottom, right). The z-axis has been scaled with a factor 10.

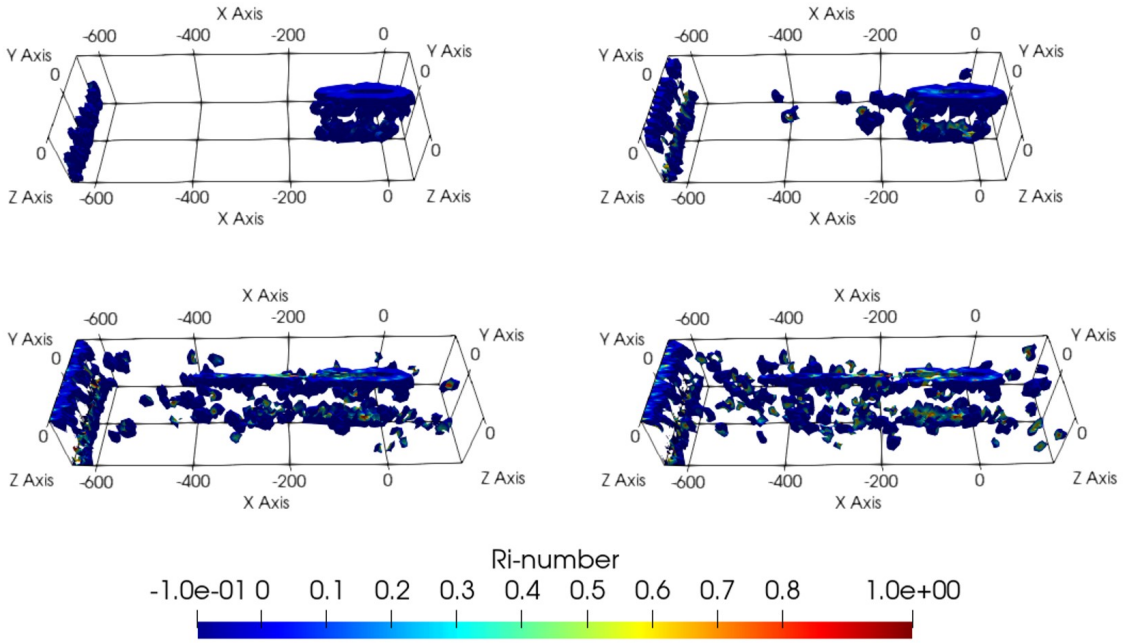

Figure F.11: Low Richardson numbers (negative to 1) found for run 17 to 20 (top right to top left, bottom right to bottom left).

F.4. Run 21 to 24

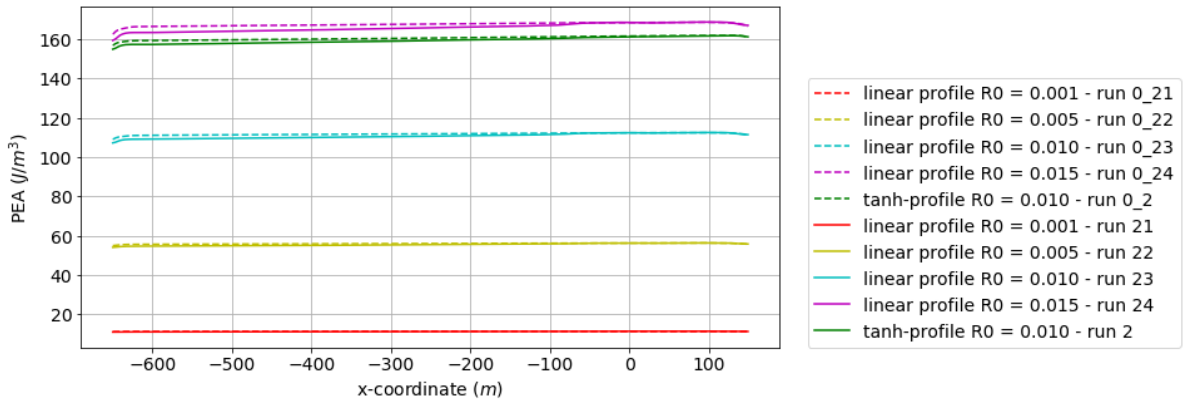

Figure F.12: The width-averaged PEA for run 21 to 24, run 2 and corresponding runs without a vessel. Due to the different relative density differences, the PEA differs a lot between these runs

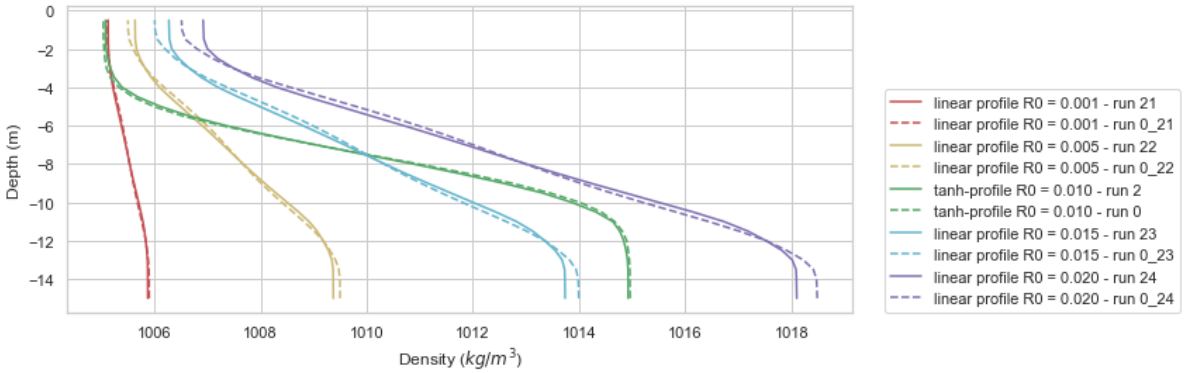

Figure F.13: The density profile at 50 m from the outflow boundary for run 21 to 24, run 2 and corresponding runs without a vessel. The linear profile shifts to a more trapped profile for both the run with and without a vessel.

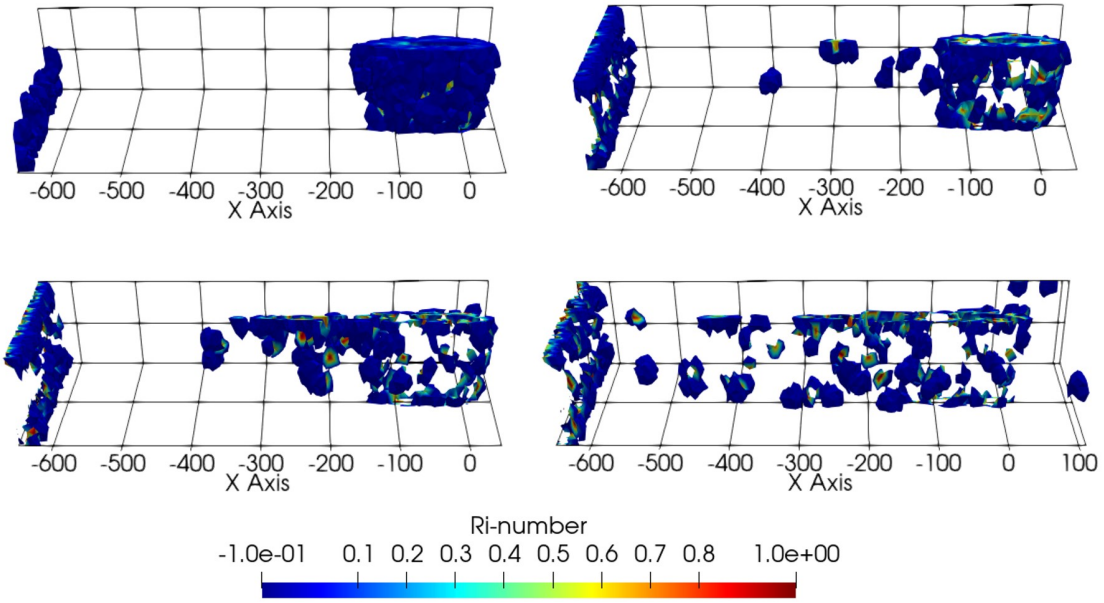

Figure F.14: Low Richardson numbers (negative to 1) found for run 21 to 24 (top right to top left, bottom right to bottom left). The low Richardson numbers are more spread over the depth compared to the two-layer runs.

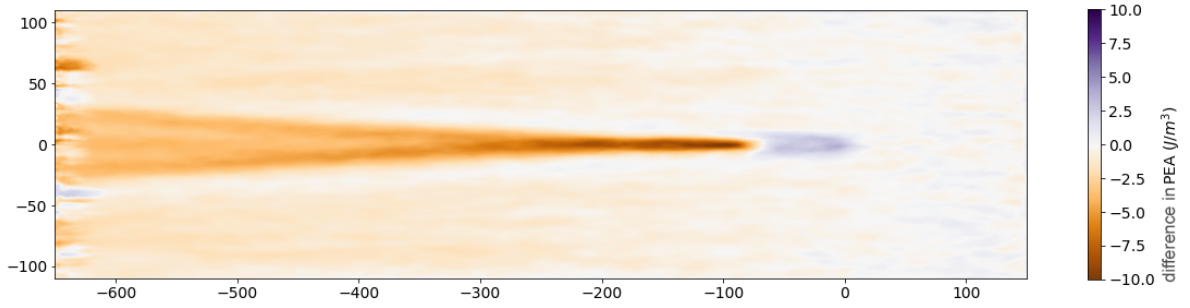

Figure F.15: Difference in PEA between run 23 (linear profile with R0 = 0.010) and the corresponding run without a vessel. Differences between this pattern and the pattern in Figure 5.8 are the increase in PEA at the location of the vessel (x = 0 to x = - 100 m) and the decrease in PEA in the area in between the wave crests.

F.5. Run 25 to 28

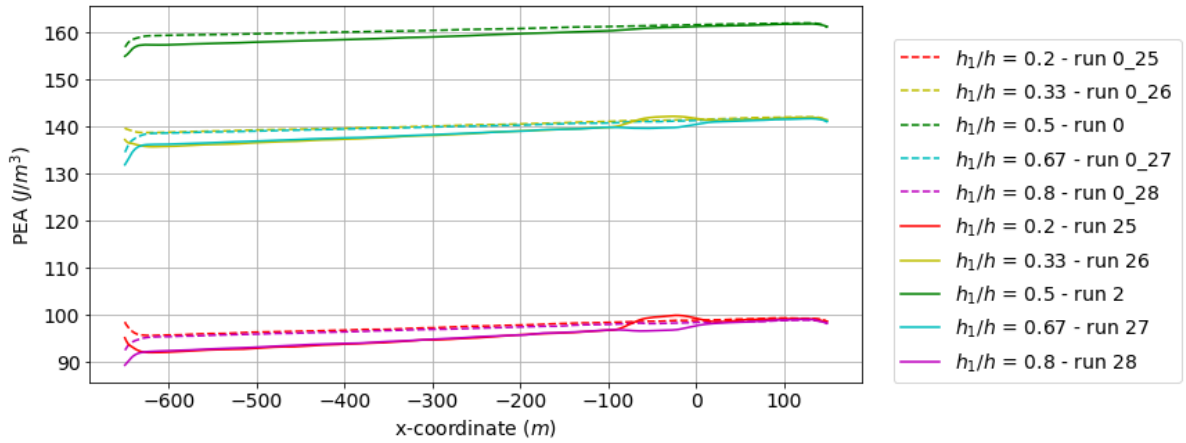

Figure F.16: The width-averaged PEA for run 25 to 28, run 2 and corresponding runs without a vessel. Due to the different density distributions, the PEA differs a lot between these runs

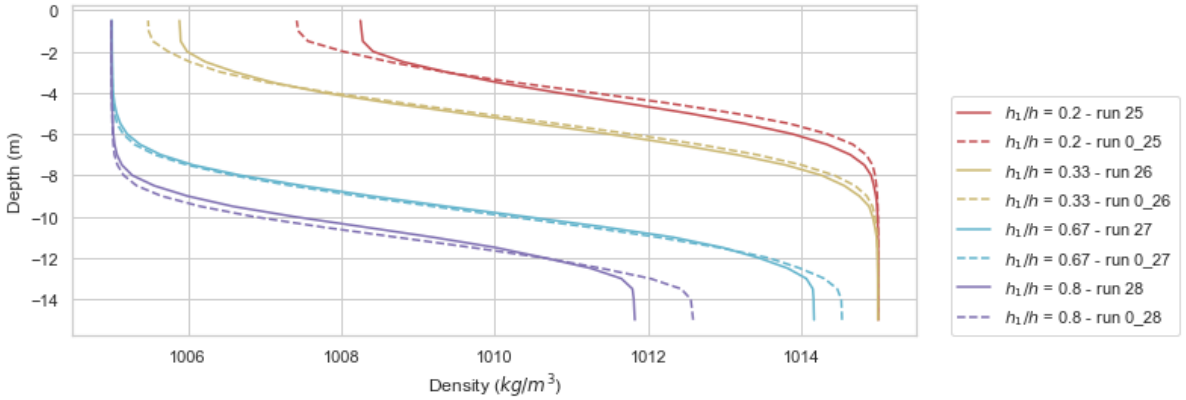

Figure F.17: Density profiles at 50 m from the outflow boundary for the run with and without a vessel for run 25 to 28. The numerical diffusion is relatively large as the runs without a vessel have shifted relatively much from the top density of 1005 kg/m^3 and bottom density of 1015 kg/m^3.

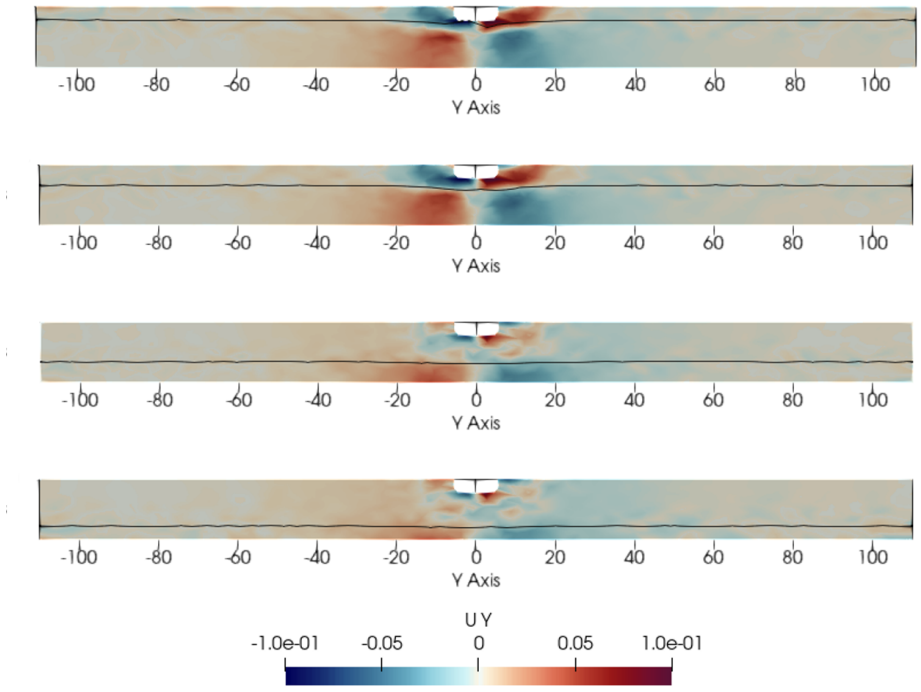

Figure F.18: Velocity in y-direction at $x = -50$ m for run 25 to 28 with the interface plotted as a black line. There is a clear velocity difference between the top and bottom layer, especially for the runs with a small top layer. The velocity in x-direction around the vessel is not influenced by the layer distribution, and the velocity in z-direction is influenced by the layer distribution, but does not show a velocity difference between the layers.

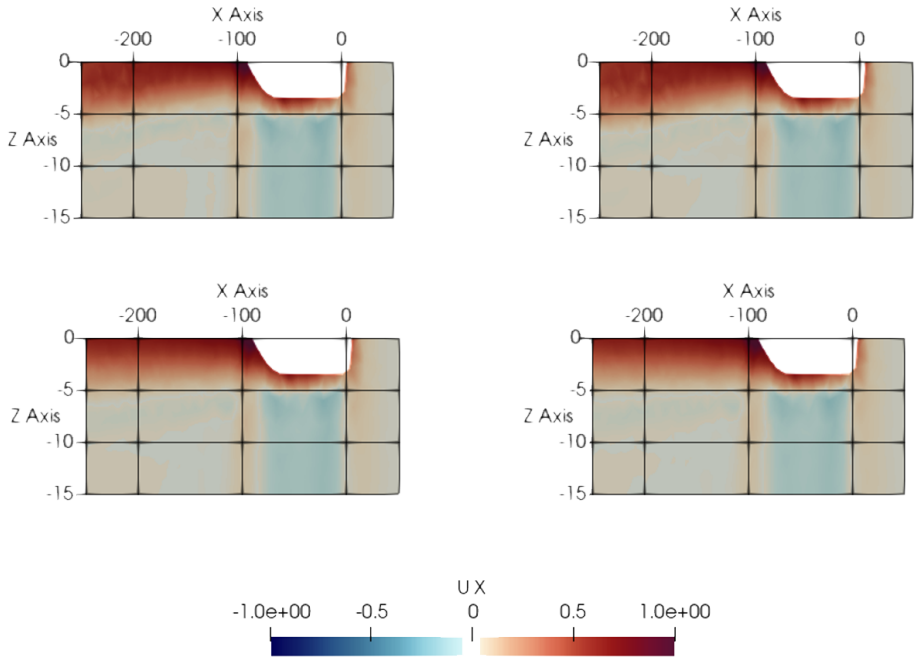

Figure F.19: Velocity in x-direction at y = 0. From left to right, top to bottom: run 25, 26, 27, and 28.

F.6. Run 29 to 36

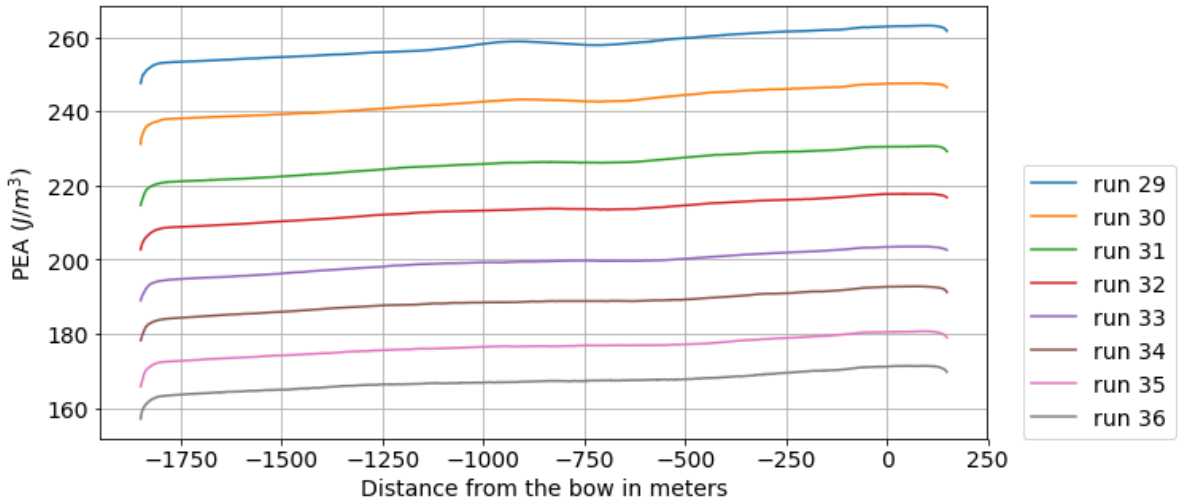

Figure F.20: The width-averaged PEA for run 29 to 36 with from top to bottom an increasingly more shallow canal bank slope. Due to influence of the shallow areas above the canal bank slopes, the PEA differs a lot between these runs

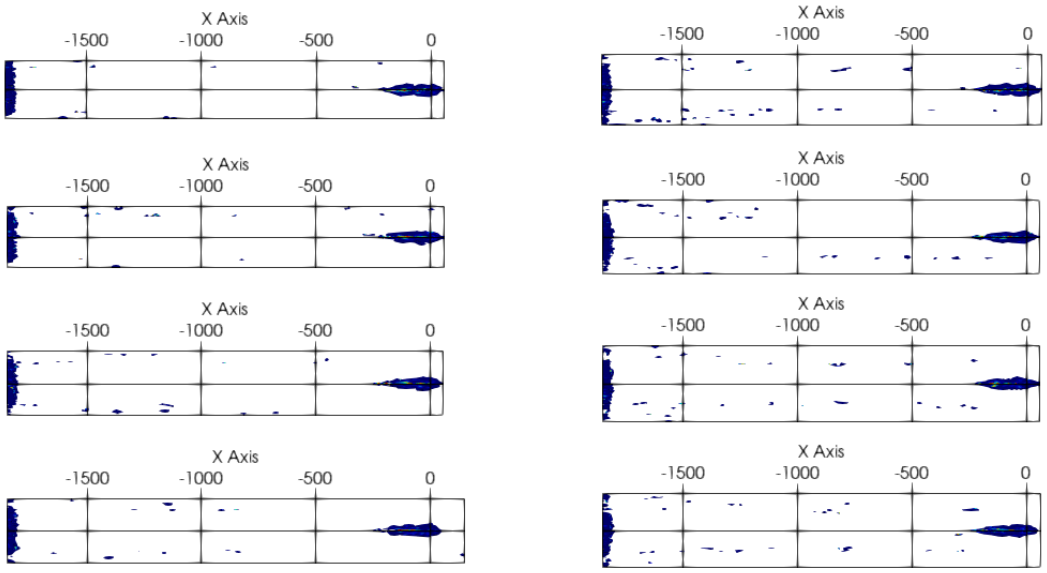

Figure F.21: Low Richardson numbers (negative to 1) found for run 29 to 36 (top right to bottom right, top left to bottom left). More low Richardson numbers are found for shallower slopes.